Informes Técnicos Ciemat 1522
Agosto, 2023

HEATING AND HYDRATION OF A COLUMN OF BENTONITE PELLETS FOR 10 YEARS: POSTMORTEM CHARACTERISATION

Villar Galicia, Mª. V.
Cuevas, J.
Melón Sánchez, A.E.
Zabala de la Fuente, A.B.
Ortega, A.
Iglesias, R. J
Ruiz, A.I.
Brea, N.
González, A.E.
Gutiérrez-Álvarez, C.
Gutiérrez-Nebot, L.
Real, E.

GOBIERNO DE ESPAÑA
MINISTERIO DE CIENCIA E INNOVACIÓN
Ciemat
Centro de Investigaciones Energéticas, Medioambientales y Tecnológicas

Publication available in catalog of official publications

ISSN: 2695-8864
NIPO: 832-23-002-2

Edition and Publication:
Editorial CIEMAT
Avda. Complutense, 40 28040-MADRID
e-mail: editorial@ciemat.es
Editorial news

TRATAMIENTO TERMO-HIDRÁULICO DURANTE 10 AÑOS DE UNA COLUMNA DE PELLETS DE BENTONITA: CARACTERIZACIÓN POST MÓRTEM

Villar, M. V; Cuevas, J.; Melón, A.M.; Zabala, A.B.; Ortega, A.; Iglesias, R. J.; Ruíz, A.I.; Brea, N.; González, A.E.; Gutiérrez-Álvarez, C.; Gutiérrez-Nebot, L.; Real, E.

74 pp., 65 refs., 57 figs., 13 tbls.

Resumen

Para simular las condiciones de la barrera del ensayo in situ HE-E, una columna de 50 cm de pellets de bentonita se sometió a calentamiento por la base a 140 °C mientras se hidrataba por el extremo contrario con agua de Pearson. Tras 10 años el material seguía siendo una esmectita dioctaédrica con distribución de cationes estructurales y carga similares a los de la bentonita original. Se mantuvo el sodio como catión predominante, probablemente debido a la composición del agua de hidratación, aunque con aumento de la contribución de cationes divalentes en la parte superior de la columna. Las muestras más secas, sometidas a T>60 °C, necesitaron someterse a humedades relativas altas para rehidratarse complemente. Los iones solubilizados se transportaron hacia el calentador y precipitaron en dos zonas bien definidas: a ~18 cm del calentador se concentraron sulfato, sodio y calcio, y la máxima concentración de cloruro se registró a ~9 cm del calentador. Cerca del calentador se identificaron calcita y sulfato cálcico y se produjo disolución de cristobalita y cuarzo. La mínima superficie específica BET se midió alrededor del sensor inferior (a 10 cm del calentador), probablemente como resultado de la desecación intensa debida a una fuga a través de la entrada del sensor. Aunque la distribución del tamaño de poros de la bentonita se vio muy afectada por la hidratación, esto no produjo un empeoramiento de sus propiedades hidro-mecánicas. En general los procesos observados fueron similares a los que se han descrito en ensayos similares en los que se utilizó como barrera bentonita compactada en lugar de pellets.

HEATING AND HYDRATION OF A COLUMN OF BENTONITE PELLETS FOR 10 YEARS: POSTMORTEM CHARACTERISATION

Villar, M. V; Cuevas, J.; Melón, A.M.; Zabala, A.B.; Ortega, A.; Iglesias, R. J.; Ruíz, A.I.; Brea, N.; González, A.E.; Gutiérrez-Álvarez, C.; Gutiérrez-Nebot, L.; Real, E.

74 pp., 65 refs., 57 figs., 13 tbls

Abstract:

With the aim of simulating in the laboratory the conditions of the barrier used in the HE-E *in situ* test, a 50-cm long column of MX-80 bentonite pellets was heated at its base to 140 °C while Pearson water was supplied through its upper surface. The mineralogical, chemical, physico-chemical and hydro-mechanical characterisation of the treated bentonite is presented. No relevant mineralogical changes were observed, and although there were some changes in the exchangeable cation complex, it continued to contain predominantly sodium. Close to the heater precipitation of calcite and sulphate and dissolution of cristobalite were observed. The pore size distribution and the way in which particles aggregated were affected by hydration and heating (desiccation), but no worsening of the hydro-mechancial properties of the bentonite was observed in the hydrated areas. Overall, the processes described are similar to those observed in other large-scale tests simulating the conditions of a bentonite barrier where compacted blocks instead of pellets were used.

ACKNOWLEDGEMENTS

The research leading to these results was performed in the framework of the EURAD project – WP7 HITEC, which receives funding from the European Union's Horizon 2020 research and innovation programme under grant agreement No 847593. Ana Beatriz Zabala was hired by CIEMAT as a pre-doctoral researcher with a grant awarded in the framework of a call of the Spanish Ministry of Science, Innovation and Universities in October 23rd 2018. Elena Real was hired in the framework of the Spanish National System of Youth Guarantee in R+D 2018, with financing of the European Social Fund and the Youth Employment Initiative. Dr. Raúl Saldaña did the SEM determinations at CIEMAT. Juan Aroz and Guillermo García participated in some of the laboratory work.

TABLE OF CONTENTS

1 INTRODUCTION 11

2 BACKGROUND: THE LABORATORY IN-CELL TEST 13

2.1 SUMMARY OF BEHAVIOUR DURING OPERATION 14

2.2 FINAL PHYSICAL STATE OF THE COLUMN 15

3 MATERIAL: MX-80 BENTONITE PELLETS 18

4 METHODOLOGY OF POSTMORTEM DETERMINATIONS 20

4.1 PORE SIZE DISTRIBUTION AND SPECIFIC SURFACE AREA 20

4.2 HYDRATION STATE (BASAL SPACING OF SMECTITE) 21

4.3 REHYDRATION OF SAMPLES 21

4.4 MINERALOGICAL CHARACTERISATION BY X-RAY DIFFRACTION 21

4.5 X-RAY FLUORESCENCE ANALYSIS (XRF) AND STRUCTURAL FORMULAE CALCULATION 23

4.6 FOURIER TRANSFORM INFRARED SPECTROSCOPY 24

4.7 THERMOGRAVIMETRIC ANALYSIS 24

4.8 MAGIC ANGLE SPINNING NUCLEAR MAGNETIC RESONANCE (MAS-NMR) . 25

4.9 SCANNING ELECTRON MICROSCOPY AND ENERGY DISPERSIVE X-RAY STUDY (SEM-EDX) 26

4.10 ELEMENTAL ANALYSIS 26

4.11 AQUEOUS EXTRACTS: SOLUBLE SALTS 27

4.12 CATION EXCHANGE CAPACITY AND EXCHANGEABLE CATIONS 27

4.13 SWELLING PRESSURE AND PERMEABILITY 28

5 RESULTS 31

5.1 PORE SIZE DISTRIBUTION AND SPECIFIC SURFACE AREA 31

5.2 HYDRATION STATE (BASAL SPACING OF SMECTITE) 36

5.3 REHYDRATION OF SAMPLES 38

5.4 MINERALOGICAL CHARACTERISATION BY X-RAY DIFFRACTION 40

5.5 FOURIER TRANSFORM INFRARED SPECTROSCOPY 48

5.6 THERMOGRAVIMETRIC ANALYSIS 51

5.7 NUCLEAR MAGNETIC RESONANCE (MAS-NMR) 51

5.8 SCANNING ELECTRON MICROSCOPY (SEM-EDX) *53*

5.9 ELEMENTAL ANALYSIS *58*

5.10 AQUEOUS EXTRACTS: SOLUBLE SALTS *59*

5.11 CATION EXCHANGE CAPACITY AND EXCHANGEABLE CATIONS *62*

5.12 SWELLING PRESSURE AND PERMEABILITY *63*

6 DISCUSSION **66**

6.1 MINERALOGY *66*

6.2 CATION EXCHANGE COMPLEX *66*

6.3 MOVEMENT OF SOLUBLE SPECIES *68*

6.4 EFFECTS OF ACCIDENTAL EVAPORATION *70*

6.5 MICROSTRUCTURE AND HYDRO-MECHANICAL PROPERTIES *71*

7 SUMMARY AND CONCLUSIONS **74**

8 REFERENCES **76**

APPENDIX **82**

LIST OF FIGURES

Figure 1 Layout of the in situ HE-E experiment (Teodori & Gaus 2011, Gaus et al. 2011)

Figure 2 Reproduction of the Swiss repository concept (Mont Terri URL) and transposition to a test in a cell

Figure 3 Experimental setup for the tests in thermo-hydraulic cells

Figure 4 Steady temperatures during hydration and relative humidity at the end of operation (3,444 days of hydration for the middle and upper sensors and 3059 days of hydration for the bottom sensor, which failed before the end of the test) inside the cell. The temperatures have been fitted to a 4^{th} degree polynomial expression

Figure 5 Appearance of the 25 sampling sections (hydration zone on the left, the photographs may show deformed diameters along the column which are not real)

Figure 6 Example of subsampling in a section for different analyses and determinations

Figure 7 Water content and dry density (empty symbols: estimated from weight and volume) and degree of saturation measured along the bentonite column at the end of the test. The thick vertical lines indicate the location of sensors, and the discontinuous horizontal lines the initial values

Figure 8 Appearance of the MX-80 bentonite pellets received at CIEMAT

Figure 9 Granulometric curve obtained by dry sieving of the bentonite pellets

Figure 10 Appearance of sample S3 once in the oedometer ring

Figure 11 Schematic layout and photograph of the high-pressure oedometric equipment

Figure 12 Incremental mercury intrusion in subsamples from the upper half of the column and of the initial GBM (see Table 2 for the location of samples)

Figure 13 Incremental mercury intrusion in subsamples from the bottom half of the column and of the initial GBM (see Table 2 for the location of samples)

Figure 14 Mean pore size obtained by MIP in samples along the column (the discontinuous horizontal lines indicate the reference values)

Figure 15 Void ratio corresponding to pores smaller (e_m) and larger (e_M) than 200 nm and ratio between them (the discontinuous horizontal lines indicate the reference values)

Figure 16 Void ratio corresponding to pores smaller (e_m) and larger (e_M) than 200 nm as a function of the degree of saturation of the samples. The open symbols correspond to the initial material

Figure 17 BET specific surface area of samples from cell HEE-B and of the initial pellets (dotted horizontal line)

Figure 18 BET specific surface area of samples from cell HEE-B and of the initial pellets (filled symbols) as a function of water content and dry density

Figure 19 Main diffraction reflection of the basal spacing of untreated subsamples of test HEE-B as a function of their position inside the cell (left) and their water content (right)

Figure 20 Profile fitting of the XRD pattern of the untreated sample S1 (46 cm from the heater)

Figure 21 Profile fitting of the XRD pattern of the untreated sample S7 (35 cm from the heater)

Figure 22 Profile fitting of the XRD pattern of the untreated sample S24 (2 cm from the heater)

Figure 23 Samples left in the laboratory atmosphere for water content stabilisation

Figure 24 Evolution of water content under room conditions of samples from the HEE-B cell and of the initial pellets previously dried at 110 °C (the legend shows the distance to the heater in cm)

Figure 25 Evolution of water content under a RH=97 % of samples from the HEE-B cell and of the initial pellets previously dried at 110 °C and stabilized at room conditions (the legend shows the distance to the heater in cm)

Figure 26 Equilibrium water contents for samples from the HEE-B cell under two different relative humidities (the dotted horizontal lines indicate the values for the untreated pellets)

Figure 27 Random powder XRD patterns of MX-80 column samples taken at various distances from the heater (see Table 2) equilibrated for 48 h at RH 55 %. The spacing of some reflections is indicated in Å. Montmorillonte (Mnt), illite (Ill), gypsum (Gp), cristobalite (Crs), plagioclase (Pl), quartz (Qz), K-feldspar (Kfs), halite (Hl), calcite (Cal)

Figure 28 Deconvolution of the basal reflection in the XRD patterns of the bulk samples S0 (~49 cm from the heater) and S25 (~1 cm from the heater)

Figure 29 Main and secondary peaks obtained by deconvolution of the basal reflection of the of bulk powder samples stabilised at 50 % RH (left) and of air-dried oriented aggregates (right)

Figure 30 XRD patterns of the air dried (OA) and ethylene-glycol solvated (EG) oriented aggregates of samples taken along the bentonite column (the reference of the samples according to Table 2 and their distance to the heater is indicated)

Figure 31 Deconvolution of the basal reflection in the XRD patterns of the oriented aggregates of samples S0 (~49 cm from the heater) and S25 (~1 cm from the heater)

Figure 32 Random powder XRD pattern of the Ca-homoionised <0.5-µm size fraction of sample S7 (up) and detail of presence of cristobalite (Crs) and quartz (Qtz) (bottom)

Figure 33 Linear regression for K_2O and SiO_2 in the XRF analyses (left); Area ratios of 1.0 nm illite to (002) Mnt (IEG/002) in the ethylene-glycol solvated oriented aggregate (EG-OA) XRD patterns versus cristobalite (0.403 nm) plus quartz (0.334 nm) reflection areas normalised to the (060) montmorillonite reflection areas (right)

Figure 34 Ca, Mg and octahedral charge in the corrected structural formulae as a function of octahedral Al (left) and of the distance to the heater (right). The horizontal dotted lines indicate the values for the reference sample (the circled symbols correspond to sample S19, at 11 cm from the heater)

Figure 35 Mid-FTIR spectra of MX-80, as reference bentonite, and several samples from S25 (hydration zone) to S0 (heater zone)

Figure 36 IR spectra of sample S16 from cell HEE-B and of the initial MX-80

Figure 37 Detail of the IR spectra of sample S16 and the initial MX-80 in the low-wavelength region

Figure 38 Mid-FTIR spectra of MX-80, as reference bentonite, and several samples S19, S20, S21

Figure 39 Detail of the IR spectra of samples S19, S20, S21 and of the initial MX-80 in the low-wavelength region

Figure 40 Differential thermogravimetric analysis data of selected samples along the HEE-B column experiment

Figure 41 ^{29}Si and ^{27}Al MAS-NMR spectra for the Ca-homoionised <0.5-µm size fraction of selected samples

Figure 42 SEM-EDX observation at the heater contact (S25 sample): scattered cavities with fine grained coatings (left); dense stacked clay aggregates fabric in the heater zone (right)

Figure 43 SEM-EDX examination of clay pellets at 9 cm from the heater (sample S20) and at the hydration surface (sample S0); a) S20 pellet surface and detail of NaCl glassy morphology coatings; b) hydration zone with filter cellulose fibres marks and detail of typical smectite platelets fabric; c) backscattered electron images of S20 pellets showing glassy NaCl coatings also inside a broken pellet; d) EDX characteristic X-rays used to outline colours corresponding to NaCl and $CaSO_4$ precipitated around cracks and plate-like discontinuities within the pellets (Ch1: backscattered electron background image channel)

Figure 44 NaCl and $CaSO_4$ (presumably hydrated) in pellets surface of sample S17. Purple grains are calcium sulphate as detailed in the bottom photographs (Ch1: backscattered electron background image channel)

Figure 45 Detail of SEM polycrystalline aggregate morphologies rich in Ca, S and Cl characteristic of soluble salt composing elements in S20 sample after drying at 110 °C and rehydrating under RH=97 % (a, b: carbon coating; c: gold coating)

Figure 46 Elemental analysis of samples along the column (note that S contents have been multiplied by 5)

Figure 47 Main cations measured in aqueous extracts of samples of cell HEE-B (the horizontal lines indicate the concentrations in the untreated pellets and the vertical dotted lines the positions of the sensors)

Figure 48 Main anions measured in aqueous extracts of samples of cell HEE-B (the horizontal lines indicate the concentrations in the untreated pellets and the vertical dotted lines the positions of the sensors)

Figure 49 Concentration of main cations (Na^{2+}, Ca^{2+}, Mg^{2+} and K^{+}), sodium, chloride and sulphate measured in aqueous extracts of samples of cell HEE-B (the horizontal lines indicate the concentrations in the untreated pellets)

Figure 50 Cations measured in aqueous extracts of samples of cell HEE-B (the horizontal line indicates the Si4+ concentration in the untreated pellets, the other ions were not detected)

Figure 51 Sum of extractable cations and CEC along the bentonite column of cell HEE-B (the dotted horizontal lines indicate the initial values)

Figure 52 Main extractable cations along the bentonite column of cell HEE-B (the horizontal lines indicate the concentrations in the untreated pellets and the vertical dotted lines correspond to the positions of the sensors)

Figure 53 Sum of cations extracted with $CsNO_3$ and of soluble cations (solubilised with aqua) along the bentonite column of cell HEE-B (the dotted horizontal lines indicate the initial values)

Figure 54 Evolution over time of axial pressure developed by samples from the HEE-B test saturated with deionised water

Figure 55 Swelling pressure values measured in samples from the HEE-B test before and after the permeability tests and for MX-80 bentonite samples (Eq. 1)

Figure 56 Relation between void ratio corresponding to pores <200 nm (as determined by MIP) and the basal spacing determined in untreated samples from test HEE-B

Figure 57 Main diffraction reflection of the basal reflection of subsamples of lab tests performed with MX-80 bentonite (values from Villar et al. 2012b, Villar 2013 and other unpublished results) and of the HEE-B cell

LIST OF TABLES

Table 1 Initial and final chemical composition of the water used to hydrate the bentonite column (mg/L)

Table 2 References of the samples taken, their location along the column relative to the heater and temperatures in the area during the test according to Figure 4

Table 3 Mineralogical phases used for the identification of minerals in bentonite. ICDD PDF2 standards (2001) used as references are included (abbreviations for minerals follow Whitney & Evans (2010))

Table 4 Assignation of bands of the FTIR spectra

Table 5 XRF chemical analysis of the Ca-homoionised <0.5-µm size fraction of some samples

Table 6 Calculated structural formulae ($O_{10}(OH)_2$ basis) of the Ca-homoionised <0.5-µm size fraction of some samples (IV: tetrahedral site; VI: octahedral site; Ca, K: interlayer cations; LCh: layer charge; Oct: octahedral)

Table 7 SEM-EDX localised analyses in sample S25. Fill: inside cavity; Wall: cavity rim; Out: external clay surrounding cavity; Bulk: clay analyses in the dense aggregates. 3 analyses in cavity zones and 12 analyses in the dense clay aggregates matrix

Table 8 Structural formulae calculated from the SEM-EDX localised analyses in sample S25 shown in Table 7. Fill: inside cavity; Wall: cavity rim; Out: external clay surrounding cavity; Bulk: clay analyses in the dense aggregates. Ca, Na, K: interlayer cations; LCh: layer charge ($K+(2xCa)+Na/O_{10}(OH)_2$); Sumoct: sum of octahedral cations

Table 9 Average and standard deviation for 6 and 12 SEM-EDX analyses performed in the clay materials of samples S20 and S0, respectively

Table 10 Structural formulae calculated from the SEM-EDX analyses shown in Table 9. Na, Ca, K: interlayer cations; Sumoct: sum of octahedral cations; LCh: layer charge ($K+(2xCa)+Na/O_{10}(OH)_2$)

Table 11 SEM-EDX analyses performed in sample S20 after heating and rehydration at the locations indicated in Figure 45 (a: area analysis; b, c: localised analyses)

Table 12 Results of the swelling pressure (P_s) tests in two samples from test HEE-B

Table 13 Results of the hydraulic conductivity (k_w) measurements in samples from test HEE-B

1 INTRODUCTION

A common design of a high-level radioactive waste (HLW) disposal system consists of the wastes encapsulated within canisters that are emplaced in horizontal tunnels or vertical shafts, with the space between the canisters and the surrounding rock filled with a buffer material, usually consisting of a bentonite-based material. In particular in the Swiss concept (NAGRA 2019), the canisters rest on a lower bed made of highly compacted bentonite blocks and the rest of the gallery is filled by granular buffer material (GBM, i.e. pellets). In the early post closure period the buffer is expected to experience the maximum temperature and be largely unsaturated. The Swiss National Cooperative for the Disposal of Radioactive Waste (NAGRA) simulated the temperature evolution of the buffer and surrounding host rock according to their disposal concept and showed that the canister surface temperatures would reach a maximum value of ~150 °C within a few years after emplacement (Johnson et al. 2002). Considering these premises and with the aim of reproducing the conditions corresponding to the initial emplacement of wastes, i.e. high heat generation and low but increasing moisture in the buffer, a 1:2 scale in situ test was designed and constructed at the Mont Terri Underground Research Laboratory (URL) in Switzerland, the HE-E experiment (Teodori & Gaus 2011; Gaus et al. 2011, 2014).

The experiment is being carried out in a 50-m long horizontal tunnel of 1.3 m diameter, excavated in the shaly facies of the Opalinus Clay, where two heaters are placed in a steel liner supported by MX-80 bentonite blocks. The tunnel is divided in two sections: in one of them the upper part of the gallery is filled with a sand/bentonite mixture and in the other one with MX-80 bentonite pellets (Figure 1). The heater system was switched on in June 2011 and, after a transitory period, has held a constant temperature on the heaters' surface of 140 °C.

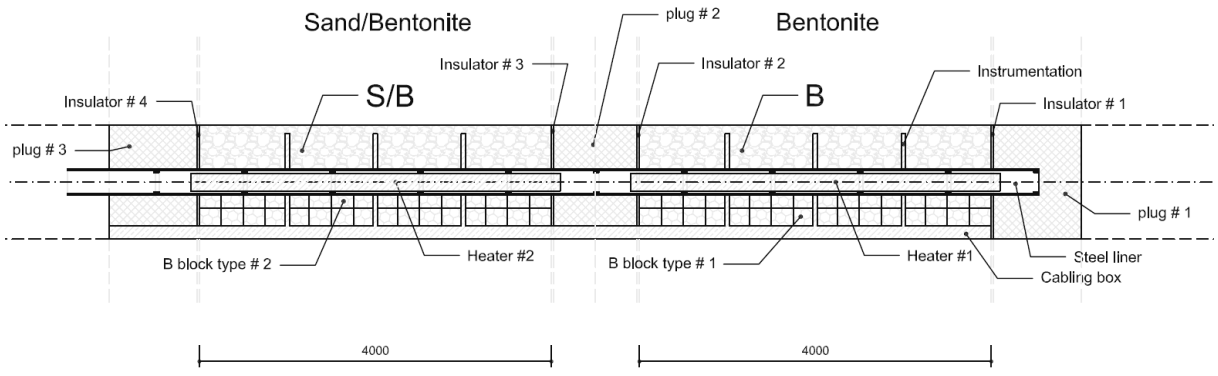

Figure 1 Layout of the in situ HE-E experiment (Teodori & Gaus 2011, Gaus et al. 2011)

The performance of large-scale in situ tests such as the HE-E has a technical demonstration aim and is also very useful to observe the thermo-hydro-mechanical processes that take place in the buffer and the geological medium, because these are usually heavily instrumented systems that provide information required for the verification and validation of mathematical models of the coupled processes and their evolution. However, they are complicated to mount and costly and for these reasons they should run for long periods of time. Additionally, the information that can be obtained online about the mineralogical or geochemical evolution is very limited, because of

the lack of appropriate instruments. As a result, no information about the mineralogy and geochemistry can be obtained until the tests are dismantled. To overcome this lack of experimental evidence at different operation times, laboratory-scale tests in cells are particularly helpful to identify and quantify processes in shorter periods of time and with less uncertainty regarding the boundary conditions than the in situ tests. In these tests in cells the sealing material is subjected simultaneously to heating and hydration in opposite directions, in order to simulate the conditions of the clay barrier in the repository, i.e. the interaction of the water coming from the host rock and the thermal gradient generated by the heat emitted by the wastes in the canisters (Figure 2).

With the aim of complementing the information provided by the HE-E in situ test, CIEMAT undertook in 2012 the performance of two thermo-hydraulic (TH) tests in cells simulating the conditions of the two granular sealing materials used in the two sections of the in situ test. The cell with the sand/bentonite material was dismantled in February 2015, after more than three years of operation (Villar et al. 2015, 2016). The test with the pellets GBM (cell B) was dismantled in November 2021 (Villar et al. 2022), and this report presents the results of the postmortem characterization of the bentonite. To give a background about the conditions to which the material analysed was submitted and of its final state, the next chapter gives an overview of the operation phase, the dismantling, sampling and final physical state of the bentonite.

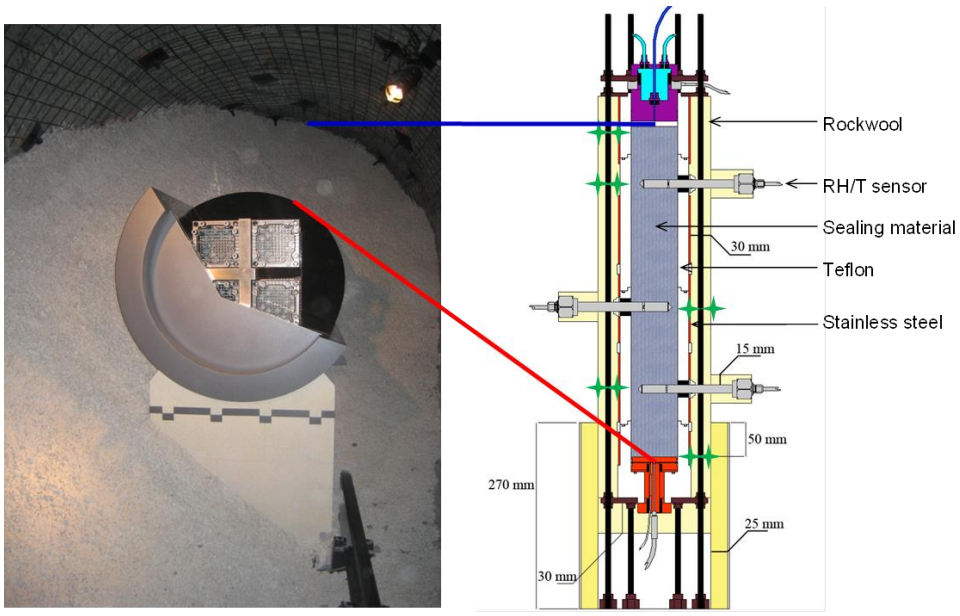

Figure 2 Reproduction of the Swiss repository concept (Mont Terri URL) and transposition to a test in a cell

2 BACKGROUND: THE LABORATORY IN-CELL TEST

To simulate the conditions of the pellets section of the HE-E in situ test, a laboratory TH test was mounted in February 2012 (cell HEE-B). The detailed description of the cell, experimental set-up and online results obtained until the end of the PEBS project were given in Villar et al. (2012a, 2014). Since the end of the PEBS project (February 2014) until June 2018, the laboratory tests went on under contract with the Mont Terri consortium. Villar et al. (2022) presented the online results for cell B obtained from the beginning of the laboratory experiment until its dismantling in November 2021, the description of the dismantling operations of the cell and the final physical state of the bentonite.

Basically, the test setup consisted of a Teflon cell with an inner length of 50 cm into which MX-80 bentonite pellets were poured. The cell was instrumented with three relative humidity (RH) and temperature sensors inserted in the bentonite and a load cell on top (Figure 3), and surrounded by stainless steel semi-cylinders to limit the Teflon deformation upon bentonite swelling. The initial water content of the pellets was 6 %, and the average dry density of the bentonite column was 1.53-1.54 g/cm^3, both values close to those of the GBM once emplaced at the URL (5.9 % and 1.46 g/cm^3). The column was heated at its base at 140°C for seven months and afterwards, it was hydrated through the upper surface at a very low pressure for nine years with a solution contained in a close vessel. In order to better reproduce the *in situ* conditions, Pearson water –a sodium-chloride water with minor amounts of sulphate, calcium and magnesium and a salinity of 19 g/L, replicating Opalinus clay host rock pore water (Pearson 2002)– was used for hydration of the material in the laboratory. Its chemical composition is indicated in Table 1, along with the chemical composition of the water contained in the hydration vessel determined at the end of the test, when it was dismantled.

CONDITIONS	Cl^-	SO_4^{2-}	HCO_3^-	Mg^{2+}	Ca^{2+}	Na^+	K^+	Sr^+	pH
Initial	10,636	1,354	26	413	1,034	5,550	63	47	7.6
Final	10,200	1,100	40	320	570	5,300	63	30	9.5

Table 1 Initial and final chemical composition of the water used to hydrate the bentonite column (mg/L)

The next subsections give a summary of the behaviour of the column during operation and of its dismantling, final physical state and subsampling. The whole postmortem characterisation of the material, including mineralogy, geochemistry and hydro-mechanical properties is presented in the rest of the report.

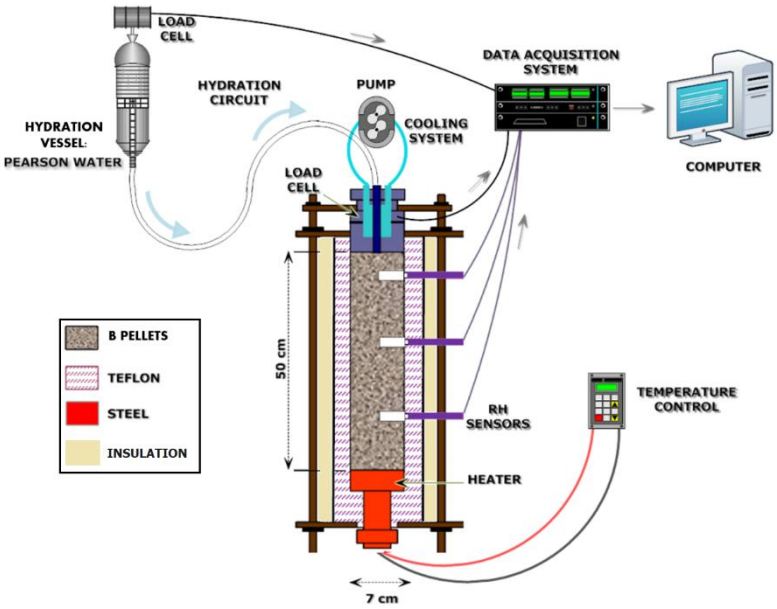

Figure 3 Experimental setup for the tests in thermo-hydraulic cells

2.1 SUMMARY OF BEHAVIOUR DURING OPERATION

The online results were presented in detail in Villar et al. 2022. The stabilisation of the temperature inside the bentonite was very quick. The power needed to keep a temperature of 140 °C was 12 W. The 7-month heating phase showed that the thermal conductivity of the dry materials was low and that heat conduction and dissipation through the bottom of the cell took place despite the insulation material, which caused a high difference in temperature between the heater surface and the sensor located at 10 cm, generating a high thermal gradient near the heater, and relatively low temperatures in the rest of the column. The temperatures did not change at the beginning of hydration and remained approximately constant until the end of the test (Figure 4).

The movement of water in the vapour phase as a result of the thermal gradient during the heating phase was evinced by the increase in relative humidity recorded by the sensor closest to the heater –followed by a continuous decrease– and the slower increase recorded by the two other sensors. The water vapour movement during the heating phase towards the upper, cooler zone, made that at the end of the heating phase the highest relative humidity (RH) values were measured in the middle of the column. During the hydration phase the low water permeability of the saturated pellets mixture was again highlighted by the long time necessary for the relative humidity sensors to record increases. It took more than 5 years for the sensor in the middle of the column to record a RH of 100 %, and for the relative humidity at 40 cm from the hydration surface to reach the initial 40 % value.

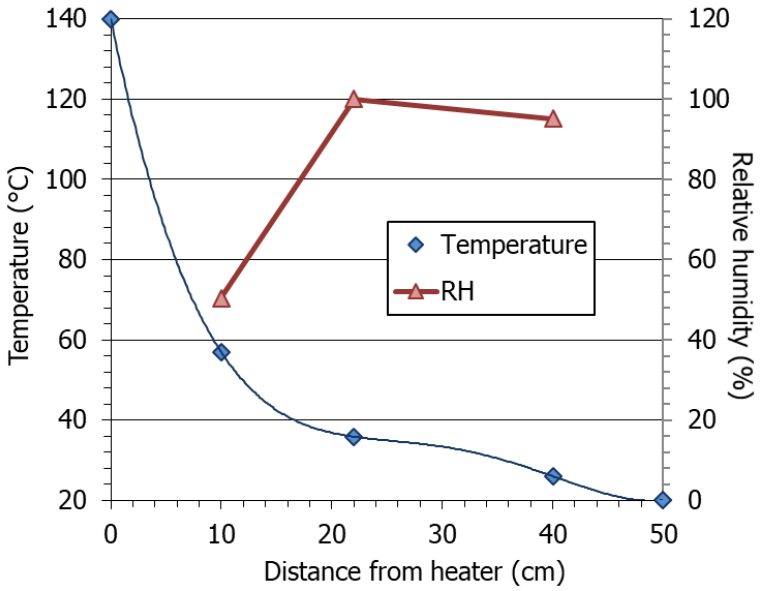

Figure 4 Steady temperatures during hydration and relative humidity at the end of operation (3,444 days of hydration for the middle and upper sensors and 3,059 days of hydration for the bottom sensor, which failed before the end of the test) inside the cell. The temperatures have been fitted to a 4th degree polynomial expression

2.2 FINAL PHYSICAL STATE OF THE COLUMN

The cell dismantling was accomplished on November 22nd 2021 (Villar et al. 2022). During the dismantling and sampling operations, the column was divided into twenty-six sampling sections, numbered from S0 close to the hydration surface to S25 close to the heater (Figure 5). The thickness of the sampling sections was 2 cm, except for sections S24 and S25 which were 1-cm thick to allow for a better discrimination in the hottest area. Each of these sections was subsampled for the different measurements. The subsampling of the sections was performed by sawing or cutting with knives, following patterns such as the one shown in Figure 6. The detailed subsampling of each sampling section can be found in Appendix II of Villar et al. (2022). The subsamples were taken for the physical, mineralogical and geochemical characterisation of the bentonite reported in the following chapters.

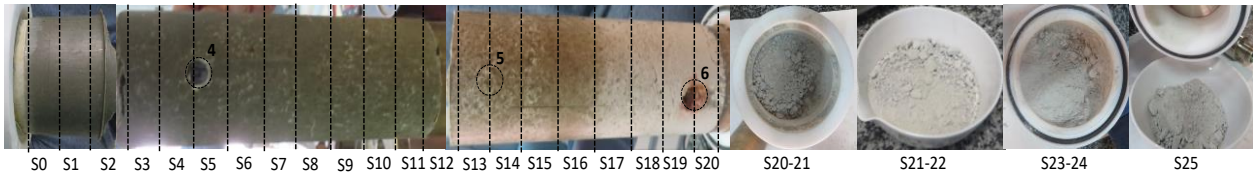

Figure 5 Appearance of the 26 sampling sections (hydration zone on the left, the photographs may show deformed diameters along the column which are not real)

REFERENCE	S0	S1	S2	S3	S4	S5	S6	S7	S8	S9	S10	S11	S12	S13	S14	S15	S16	S17	S18	S19	S20	S21	S22	S23	S24	S25
DISTANCE (cm)	48.1	46.1	44.3	42.8	41.0	39.0	37.0	35.0	33.0	31.0	29.0	27.0	25.0	23.1	21.1	19.1	17.1	15.1	13.1	11.1	9.1	7.1	5.2	3.4	1.9	0.7
TEMPERATURE (°C)	20	21	22	23	25	27	29	30	32	33	34	34	35	35	36	37	39	42	47	53	61	72	85	101	116	131

Table 2 References of the samples taken, their location along the column relative to the heater and temperatures in the area during the test according to Figure 4

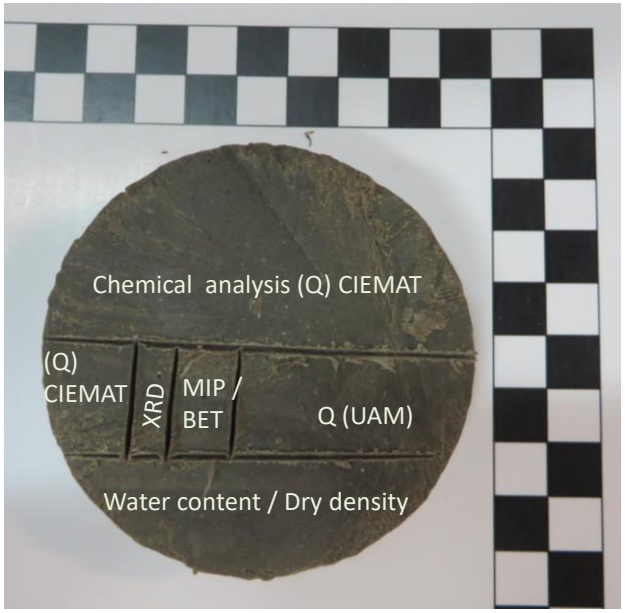

Figure 6 Example of subsampling in a section for different analyses and determinations

The water content and dry density determinations carried out immediately upon dismantling showed that the upper half of the column had water contents around 30 %, which only increased above this value in the 5 cm closest to the hydration surface (Figure 7). These large water contents correspond to uniform degrees of saturation between 92 and 99 % in the upper half of the column, where the bentonite was compact and dark, with a smooth appearance in which no pellets could be discerned. In contrast, the water content and degree of saturation decreased sharply towards the heater in the bottom half of the column, with values close to 0 % in the 5 cm closest to the heater. At less than 16 cm from the heater the bentonite was lighter in colour and was loose. In this respect, the dry density of the upper 30 cm was less than the initial one (particularly close to the hydration surface) but tended to increase towards the heater, where it was difficult to determine because of the disaggregated state of the granulate. The best estimation of the average final water content of the column is 22.0 %, and of the dry density 1.52 g/cm^3, corresponding to a degree of saturation of ~75 %.

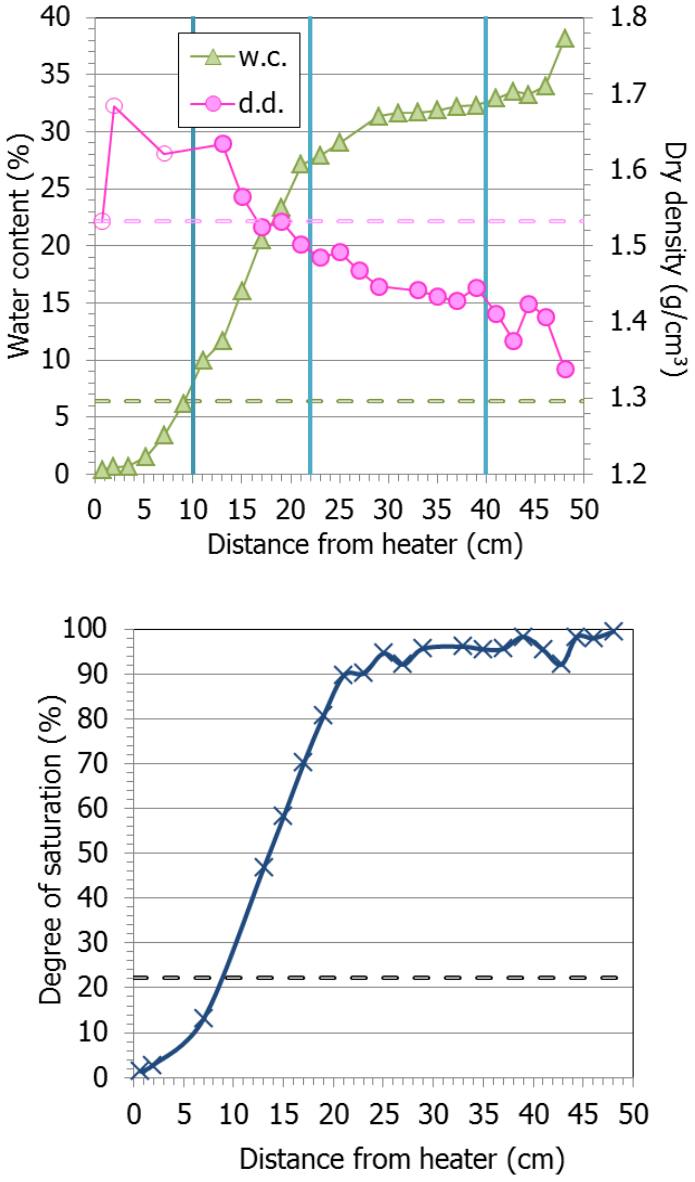

Figure 7 Water content and dry density (empty symbols: estimated from weight and volume) and degree of saturation measured along the bentonite column at the end of the test. The thick vertical lines indicate the location of sensors, and the discontinuous horizontal lines the initial values

3 MATERIAL: MX-80 BENTONITE PELLETS

The material used in the cell test was the same as that used in the *in situ* test and was sent to CIEMAT directly from the Mont Terri test site. Twenty kilos of the MX-80 bentonite pellets were received in June 2011 (Figure 8). The characteristics of the bentonite batch used and the manufacturing process of these pellets are described in detail by Plötze & Weber (2007) and summarised by Valter & Plötze (2013). The following characteristics were determined at CIEMAT:

- The as-received water content of the pellets mixture was 6.4 % and the dry density of the individual pellets was ~2 g/cm^3.
- The grain sizes of the pellets ranged between 10 and 0.1 mm, and they were combined according to the granulometric curve shown in Figure 9, which was obtained by dry sieving.
- The density of the solid grains obtained with pycnometers using water as dispersing agent was 2.75 g/cm^3.

Figure 8 Appearance of the MX-80 bentonite pellets received at CIEMAT

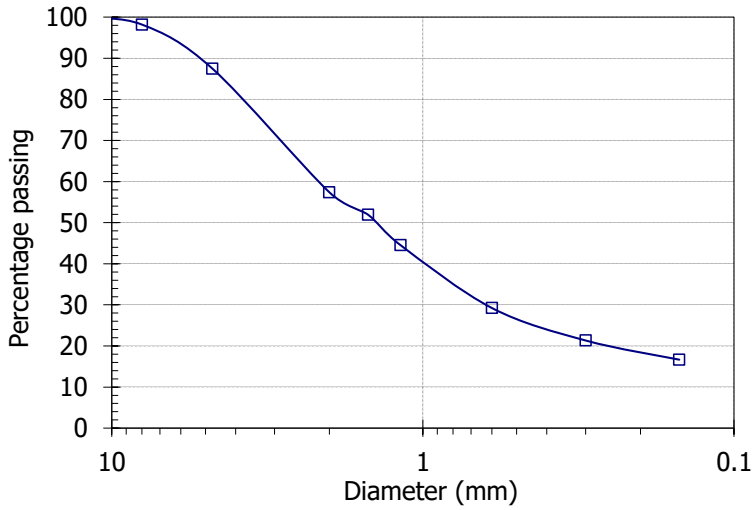

Figure 9 Granulometric curve obtained by dry sieving of the bentonite pellets

The MX-80 bentonite is a brand name used by the American Colloid Company for sodium bentonite from Wyoming (USA), milled to millimetre-sized grains. According to studies performed in different batches of this bentonite by different authors, the montmorillonite content is between 65 and 90 %, with quartz, plagioclase and K-feldspars (contents between 4 and 15 %), and minor amounts of cristobalite, tridymite, calcite, gypsum, pyrite, illite. The cation exchange capacity is 75-82 meq/100g. Na^+ is the main exchangeable cation (50-74 meq/100 g), with also Ca^{2+} (10-30 meq/100 g) and Mg^{2+} (3-8 meq/100g). The main soluble ions are sodium and sulphate. For the sake of comparison, the detailed characteristics and properties of the pellets used in this test are given along with the postmortem characterisation of the material coming from the cell dismantling in chaper 5.

The swelling pressure of small samples (3.8 or 5.0 cm in diameter, 1.2 cm in height) of MX-80 bentonite powder compacted with its hygroscopic water content was determined at CIEMAT at room temperature using deionised water as saturation fluid (Villar 2013). The swelling pressure (P_s, MPa) could be related to final dry density (ρ_d, g/cm^3) through the following equation:

$$\ln P_s = 5.44\ \rho_d - 6.94 \quad (R^2=0.94,\ 33\ \text{values}) \qquad [1]$$

The difference between experimental values and this fitting is, on average, 19 %.

The hydraulic conductivity (k_w, m/s) of samples of powdered MX-80 bentonite, compacted at different dry densities (ρ_d, g/cm^3) and kept in stainless steel cells which hindered the swelling of the material upon saturation, was measured in constant head permeameters using deionised water as permeant. These measurements were performed in the framework of two different projects in which different batches of the material were used, the Prototype project (permeability results in Villar 2005) and the MAB (Mineralogical Alteration of Bentonite) project (Idiart et al. 2022, unpublished permeability results). The results obtained in the two test series differed, particularly towards the low densities. Nevertheless, an exponential relation between dry density (ρ_d, g/cm^3) and hydraulic conductivity (k, m/s) was found considering both sets of results (R^2=0.62):

$$k_w = 1\cdot10^{-8}\ e^{-7.24\ \rho_d} \qquad [2]$$

Although these tests were performed in powder material with a grain size <1 mm (from different batches to that used to manufacture the pellets), it is considered that the saturated hydro-mechanical properties of pellets mixtures are similar to those of fine granulates (e.g. Imbert & Villar 2006).

4 METHODOLOGY OF POSTMORTEM DETERMINATIONS

After the subsamples were obtained according to the distribution detailed in Appendix II of Villar et al. (2022), they were kept in hermetic containers or wrapped in plastic film and analysed following the methods described below.

4.1 PORE SIZE DISTRIBUTION AND SPECIFIC SURFACE AREA

The pore size distribution of each subsample was determined by mercury intrusion porosimetry (MIP). This technique allows the determination of the pore size distribution by injecting mercury into the sample at different pressures while measuring the volume intruded. The pressure applied may be related to the minimum pore diameter intruded taking into account the characteristics of the fluid (Washburn equation). The ratio of the volume of mercury intruded (pore volume) to the applied pressure (which conditions the minimum pore diameter) allows distribution curves to be obtained establishing the percentage of pores of a size included within a given interval.

The pores of the sample have to be empty, i.e. free of water, before the mercury intrusion test. In order to minimise the alteration of the clay microstructure during water removal, the samples were put in the ice condenser of a Telstar LioQuest equipment at -30 °C for 3 hours. Subsequently, they were lyophilised for 22 hours at a temperature of -50 °C under a vacuum of 0.2 mbar, so that to eliminate the water in the pores by sublimation. Thereafter, they were heated at 25-30 °C for 3 hours. The samples were later kept in a desiccator until the MIP analysis. The mass of the subsamples used was between 0.7 and 1.6 g. The porosimeter used was a Micromeritics AutoPore Series IV 9500, which allowed the exploration of pore diameters between approximately 0.006 and 560 µm. Prior to mercury injection the sample was outgassed by applying a vacuum of 50 µm-Hg. Afterwards the mercury injection pressure was increased from 2.7 kPa to 220 MPa in 109 steps. To determine the extrusion branch of the curve, the pressure was released in 56 steps down to a pressure of 68.6 kPa. A contact angle of mercury of 139° both on advancing and receding on the clay surface was considered.

The sorption isotherms were determined in an ASAP 2020 of Micromeritics. The samples were lyophilised (as for the MIP samples explained above) and ground in an automatic agate mortar for 3 minutes. Aliquots of between 0.5 and 2.5 g were degassed at 90<°C for the time necessary to reach a vacuum of 50 µm Hg, which was kept for 10 min. Afterwards the samples were kept at 90 °C under vacuum for 500 minutes. The isotherms obtained had 58 points, 35 in the range of relative pressures between 0.01 and 0.995 and 23 points in the range 0.995 and 0.14.

The specific surface area of the bentonite samples was determined using the BET method (Brunauer et al. 1938) to analyse the adsorption isotherms of nitrogen gas. This parameter represents the external surface area, i.e. the surface of the intra-aggregate and inter-aggregate voids but not that of the interlayer space. Thus, it is a measure of the degree of coherent stacking of smectite platelets (Sposito 1992). The BET method was applied in the range of P/P_0 0.06-0.2.

These determinations were performed at CIEMAT.

4.2 HYDRATION STATE (BASAL SPACING OF SMECTITE)

The (001) reflection or basal spacing gives the distance along the crystallographic *c*-axis between clay lamellae, and for a given clay depends on the exchangeable cations present in the interlayer and their degree of hydration.

From all the sections of the column, subsamples were preserved in paraffined foil and the X-ray profile of a plane surface of them was registered at laboratory temperature after removing the foil and without any further treatment. Around 23 days elapsed since the samples were retrieved until they were X-rayed. An anticatode of Cu (CuKα) radiation was used with a Philips model X'Pert-MPD diffractometer at 40 mA, 45 kV operating condition. X-ray diffraction (XRD) experimental profiles were obtained with a 0.1-mm entrance slit and a scanning rate of 0.025 °2θ/s. Data were collected between 2 and 10 °2θ. The goniometer settings were: automatic divergence slit and diffracted beam slit 2 mm. The position of the reflections was corrected using the XRD pattern obtained under the same conditions of an α-Al_2O_3 standard. The complete mathematical description of the scan pattern was obtained by combination of a polynomial function that describes the background and a profile function that fits the experimental peaks in order to obtain better peak parameters (peak position, net intensity and full width at half maximum (FWHM)). The pseudo-Voigt profile function, which is the weighted mean between a Lorentz and a Gaussian function, was used to fit the peaks as well as to deconvolute overlapped peaks.

4.3 REHYDRATION OF SAMPLES

Some of the samples used for the water content determination at the end of the test (values in Figure 7), which were dried in the oven at 110 °C, were left in the laboratory atmosphere to rehydrate and later placed in a desiccator with a sulphuric acid solution generating a relative humidity of 97 %. In both cases the changes in water content of the clay were followed by periodically weighing the samples.

4.4 MINERALOGICAL CHARACTERISATION BY X-RAY DIFFRACTION

Portions of the samples of ~10 g were gently ground in an agate mortar and dried under vacuum at ambient temperature. 0.5 g of the dried samples were further ground to <5 μm using an MM200 RETCH zircon ball grinder (Verder Scientific GmbH & Co. KG, Haan, Germany). The samples were equilibrated and stored in polycarbonate tubes in a 55 % RH chamber (controlled by $MgNO_3$ saturated solution at 25 °C) during more than 48 hours prior to taking randomly oriented powder XRD patterns. At this RH Na smectite typically exhibits a 1.25-nm basal reflection and Ca-smectites around 1.50 nm (MacEwan & Wilson 1984). The X-ray diffraction (XRD) patterns were recorded in an angular range of 3-70 °2θ in a X-PERT Panalytical instrument with an X-CELERATOR detector (Malvern PANalytical™ Ltd, Malvern, UK), which allowed the taking of measurements equivalent to 0.016°2θ angular steps for 100 s for each step. The voltage and intensity of the X-ray Cu tube were 45 kV and 40 mA, respectively. The equipment used

monochromatic radiation provided by a Ge 111 primary monochromator. The slit settings were: soller slit (0.04 rad), divergence and antiscatter slits both of 0.5°.

The mineralogical composition of these samples was identified qualitatively taking into account the International Centre for Diffraction Data (ICDD) powder diffraction files standards (Table 3) supported by the High Score Expert Plus© software (version 2.1.b 2005) (Cuevas et al. 2014). Direct comparison of graphical representations of XRD sample profiles was preferred to semiquantitative interpretations to assess mineralogical differences related to smectite hydration states or distribution of exchangeable cations.

MINERALOGICAL PHASES	PDF STANDARD REFERENCE
Montmorillonite (Mnt)	00-043-0688[a] 00-013-0135[b]
Illite-mica (Ilt-Mca)	00-006-0263[c]
Quartz (Qz)	01-079-1910
Cristobalite (Crs)	00-039-1425
Calcite (Cal)	00-024-0027
Gypsum (Gp)	01-076-1746
Anhydrite (Anh)	01-072-0916
Sanidine (Sa, Kfsp)	00-010-0353
Plagioclase, anorthite (Pl, An)	00-041-1486
Pyrite (Py)	00-006-0710
Halite (Hl)	00-001-0994 01-075-0306

[a] montmorillonite 15 Å;
[b] beidellite 12 Å (the use of both is justified by the common observation of an asymmetric tail to high 2θ angles in the montmorillonite basal reflection);
[c] moscovite

Table 3 Mineralogical phases used for the identification of minerals in bentonite. ICDD PDF2 standards (2001) used as references are included (abbreviations for minerals follow Whitney & Evans (2010))

The variation of the *d*-values of the basal reflections for montmorillonite in powder patterns was used to confirm changes in the distribution of exchangeable cations. The measurement of the basal spacing was performed also on <0.5 µm fractions previously extracted by means of deionised water suspension and centrifugation. To obtain the <0.5-µm fraction from the 10-g ground portion mentioned above, ~3 g of bentonite (x 2) were wetted in 800 cm^3 of deionised water in a 1-L polypropylene beaker for at least 24 hours. After this time, the clay-water mixture was treated using a rod stirrer and an ultrasonic water bath simultaneously for 5 minutes, then it was just stirred for 5 minutes, and this cycle was repeated five times. After 1 h, none of the mixtures flocculated and the <0.5 µm size fraction was separated by centrifugation with no dispersing agent added in order to avoid changing artificially the structural-chemical composition of the clay fraction. However, as will be discussed in the Results chapter, this was not completely possible due to the dissolution of soluble salts that may change the distribution of exchangeable cations to some extent. A SIGMA centrifuge was used with an oscillating rotor, thus allowing the calculation of the centrifuge time necessary for sedimentation of all particles >0.5 µm, knowing

the distance of the rotor axis to the bottom of the 150 cm^3 centrifuge tube and the liquid height inside the tube. Calculations were done using Centriset© software (Poppe & Eliason 2009).

After centrifugation the <0.5 µm size fraction suspensions were flocculated by the addition of 10 cm^3 of pure ethanol. Washings were performed by repeating ultrasonic bath dispersion and centrifugation until ethanol electrical conductivity was <10 µS/cm, which was achieved typically after 3-5 washing cycles. The ethanol wet slurries were dried in a desiccator with silica gel. The oriented aggregates were prepared using a 0.05-g/mL dispersed slurry that was smeared onto a 2-cm^2 glass tile and left to dry in the laboratory under ambient conditions. Ethylene glycol (EG) solvation was performed inside a close plastic box adding a filter paper inside impregnated with a few drops of EG. EG vapour entered the clay film deposited on the glass tiles lying on the paper (48 h). These samples were scanned from 3 to 40°2θ under the same conditions as the powder patterns. Basal spacing reflections were treated using the DRXWin® software (vs. 2.3.22. V. Primo ©). The reflection positions were determined using a deconvolution algorithm based on Pseudo-Voigt functions.

A portion of the <0.5 µm size fraction of selected samples and of the reference MX-80 bentonite was Ca-homoionised by soaking the centrifuged <0.5 µm size fraction in a 0.5 M $CaCl_2$ solution for one hour. The suspension was washed in a first batch with pure water followed in subsequent steps by using pure ethanol. The XRD random powder profiles were registered for these fractions in order to check their monomineralic character. The Ca-homoionised <0.5-µm size fractions were used for X-ray fluorescence (XRF) and ^{29}Si and ^{27}Al Nuclear Magnetic Resonance (MAS-NMR) measurements.

These determinations were performed by UAM.

4.5 X-RAY FLUORESCENCE ANALYSIS (XRF) AND STRUCTURAL FORMULAE CALCULATION

The structural formulae of the smectite was calculated by UAM using analyses on the Ca-homoionised <0.5-µm fraction obtained as outlined in subchapter 4.4, which was dried at 60 °C and ground in an agate mortar. 0.5 g of the dried sample was fused with lithium tetraborate (0.3:5.5 sample:flux) in a PerlX'3 automatic bead preparation system (PANalytical™ B.V., Almelo, The Netherlands). The quantity of sample used was statistically significant for the analysis and a unique sample procedure was preferred instead of splitting the sample in smaller portions to obtain replicated analyses. The major elements were determined by means of wavelength dispersive XRF analysis in a ZETIUM (PANalytical™) instrument using a rhodium X-ray tube (Malvern PANalytical™ Ltd, Malvern, UK).

In order to obtain comparable structural formulae, the major elements were adjusted with the following criteria: I) Maintaining the relative proportion of structural cations (Si, Al, Fe, Ti, Mn, Mg, Fe as Fe(III)) by setting the total charge structural cations to fit a $O_{10}(OH)_2$ anion structural basis; II) The resulting layer charge was calculated without varying the amount of potassium, which was considered irreversibly fixed and not displaced during the calcium homoionisation

procedure. Na_2O is not properly determined by this technique and was not analysed. It was assumed that sodium was not included in the exchange complex because of the previous Ca-homoionisation.

4.6 FOURIER TRANSFORM INFRARED SPECTROSCOPY

Fourier Transform Infrared Spectroscopy (FTIR) was used by CIEMAT as an additional method for the analysis of the mineral composition and of the chemical changes in the structure of smectite, especially at the octahedral sheets. The measurements were carried out in transmission mode, in the middle-IR region (4000-400 cm^{-1}) with a Nicolet 6700 with a DTGS KBr detector. Spectra were obtained by the summation of 32 scans at a resolution of 4 cm^{-1}, using KBr-pellets obtained by dispersing 2 mg of powder sample (with no further treatment) in 200 mg of KBr.

According to pertinent references (Madejová & Komadel 2001, Estep et al. 1968, Chukanov, N.V. & Chervonnyi, A.D 2016), each vibration was assigned and these assignments are listed in Table 4.

POSITION (cm^{-1})	ASSIGNMENT
3,630	OH stretching of structural hydroxyl groups for dioctahedral smectites
3,422	OH stretching of adsorbed water
3,240	O-H stretching of adsorbed water
1,634	OH deformation of water
1,430	CO_3^{2-} asymmetric stretching of calcite
1,384	NO_3^-
1,115	Si–O stretching (longitudinal mode)
1,040	Si–O stretching typical of a dioctahedral montmorillonite.
915	AlAlOH deformation of smectites
885	AlFeOH deformation of smectites
842	AlMgOH deformation of smectites
797	Si–O stretching of quartz and silica
778	Si–O stretching of quartz
659	S-O bending gypsum
620	Coupled Al–O and Si–O, out-of-plane
594	S-O bending gypsum
520	Al–O–Si deformation (tetrahedral Al)
464	Si–O–Si deformation

Table 4 Assignation of bands of the FTIR spectra

4.7 THERMOGRAVIMETRIC ANALYSIS

Thermogravimetric analysis (TGA) measures the change in weight of a sample as a function of temperature or time in a controlled atmosphere. This technique allows to characterise materials

that exhibit loss or gain of weight due to decomposition, oxidation or dehydration. TGA is an additional diagnostic tool that provides information about the dehydration and dehydroxylation characteristics of the smectite, particularly about the kind of cations in the interlayer and the position of the OH groups, and consequently about the cis/transvacancy character of the octahedral sheet (Emmerich 2011).

Thermal analysis of the samples was performed by TGA with 0.5 g of the bulk sample prepared just by ball milling after having stabilised them at a RH=55 %, as detailed in subchapter 4.4 for bulk randomly oriented powder XRD, ground to <5 µm. They were tested in a DSC/DTA/TGA Q600 TA Instruments R module from 25 to 1000 °C at a temperature increment rate of 10 °C/min.

In addition to the TGA curve, the curve of the first derivative (derivative thermogravimetry, DTG) is used to aid interpretation, measuring the rate of change of mass. The DTG curve gives a higher resolution and presents more accurately the specific temperature maxima corresponding to dehydration and dihydroxylation of montmorillonite.

These analyses were performed by UAM.

4.8 MAGIC ANGLE SPINNING NUCLEAR MAGNETIC RESONANCE (MAS-NMR)

High-resolution ^{29}Si, ^{27}Al and magic angle spinning (MAS) Nuclear Magnetic Resonance (NMR) spectroscopy is a technique that involves the magnetic spin energy of atomic nuclei in elements that have a non-zero nuclear spin. NMR technique on solids is applied for studying the local structure of silicates. However, conventional solid-state NMR measurements give broad and overlapping bands spectra. The standard way to improve the resolution involves minimizing the anisotropic dipolar interactions by rotating the sample about an axis oriented at 54.74° with respect to the external magnetic field (Magic Angle Spinning technique, MAS).

Nuclei with spin quantum numbers (I) greater than 1/2, such as aluminium (I = 5/2), can experience a quadrupolar interaction and therefore cause a significant line-broadening effect in NMR spectra by up to several MHz in extreme cases. This leads to an overall decrease of signal-to-noise ratio and loss of spectral resolution. However, this kind of interaction can also provide important structural information on the environment surrounding the quadrupole nucleus.

The range of isotropic ^{29}Si chemical shifts in silicates and aluminosilicates was shown to be related to polymerization of the SiO_4 tetrahedra (Q^0, Q^1, Q^2, Q^3 and Q^4) and their linkage to AlO_4 tetrahedra (Lippmaa et al. 1980). Q represents the SiO_4 tetrahedron while the superscript refers to the number of other tetrahedra to which it is linked. The shift ranges of aluminosilicates are designated as Q[nAl] where n may vary from 0 to 4.

High-resolution ^{29}Si, ^{27}Al and magic angle spinning (MAS) NMR spectra were recorded at 79.49 and 104.23 MHz (9.4 T magnetic field), with single pulse experiments by spinning the samples at 10000 cps at the magic angle (54°44'') using a Bruker Avance 400 spectrometer equipped with a Fourier transform unit. The pulse lengths were 5 and 2 µs and the recycle delays were 10 and 5 s respectively for the ^{29}Si and ^{27}Al nuclei, to get a maximum in the intensity of the experimental

signal. The number of accumulations was 800 for ^{29}Si (4.6 % abundance) and 400 for ^{27}Al (100 % abundance) signals. Chemical shifts are reported in ppm relative to tetramethylsilane (TMS) for ^{29}Si and 1 M $AlCl_3$ aqueous solution for ^{27}Al. This analysis was performed with 0.5 g of the Ca-homoionised <0.5-µm fraction prepared as outlined in subchapter 4.2 and ground to <5 µm.

These analyses were performed by UAM.

4.9 SCANNING ELECTRON MICROSCOPY AND ENERGY DISPERSIVE X-RAY STUDY (SEM-EDX)

Scanning Electron Microscopy and Energy Dispersive X-ray Spectroscopy (SEM-EDX) studies were performed by UAM trying to detect singular surface characteristics of clay near the hydration surface or materials adhered to the heater. These observations allowed to identify the nature of soluble salts in contacts and metallic compounds characteristic of rust zones, especially near the heater.

The equipment used was an Hitachi S-3000N with a theoretical resolution of 3 nm at 25 kV and voltage from 0.3 to 30 kV. An EDX detector coupled to an Oxford Instruments X-ray Energy Dispersive analyser, model INCAx-sight, was used. Measurements were made in high vacuum, and secondary-electron or backscatter-electron detectors were used.

Samples were prepared by scrapping unaltered chips at the surfaces, which were then dried in vacuum for at least 24 h. Finally, they were adhered to a flat aluminum sample holder by means of graphite adhesive tape and metallized with Au prior to observation.

EDX Chemical analysis included C and O, quantified with significant uncertainty. Nevertheless, they were included in order to support criteria for consideration of the presence of carbonates and Fe oxides.

To analyse sample S20 after the rehydration procedure described in subchapter 4.3, CIEMAT used a ZEISS EVO LS 15 SEM microscope coupled to an Oxford Instruments X-Max energy dispersive X-ray energy spectrometer (XEDS), which allows for the analysis of light elements from boron. Without previous drying, fragments of this sample were subjected either to a gold metallization by applying 0.008 mbar vacuum and a gold coating of 30 to 40 nm thickness or to carbon coating.

4.10 ELEMENTAL ANALYSIS

Simultaneous determination of the percentage of carbon, hydrogen, nitrogen and sulphur was performed by UAM in a fine powder (<5 µm) of the bulk sample obtained by grinding in an agate mortar. Prior to the measurements the powder was equilibrated in an atmosphere of 55 % RH, what reduced the original water content of the samples. The method is based on total sample oxidation by means of a fully instantaneous combustion and thermal-heating, in which these elements are converted to gases (CO_2, H_2O, NO_2 and SO_2). They are transported with a carrier gas (helium) to the flow current to pass through individual and selective sensors implemented in a

LECO CHNS-932™ equipment (Model NO: 601-800-500). The minimum quantified content is 0.2 wt %, and the quantity of sample used was 1 mg (triplicated for each sample).

4.11 AQUEOUS EXTRACTS: SOLUBLE SALTS

The total amount of soluble salts (dissolved inorganic solutes) was analysed by CIEMAT in aqueous extract solutions. The aqueous extracts do not directly give the pore water composition, but just the soluble salts content for a particular solid:liquid ratio.

To prepare the aqueous extracts the samples were crushed after some air drying and mixed with deionised water to give a solid:liquid weight ratio of 1:8 (with 5 g of clay). The suspensions were shaken and allowed to react for 24 h under atmospheric conditions. After phase separation by centrifugation for 30 minutes at 15,500 rpm (26,326 g, using a high-speed refrigerated bench top centrifuge, Sigma 3K30, with a fixed 25°-angle rotor), the supernatants were filtered through a 0.45-µm filter and the concentration of major cations analysed by Inductively Coupled Plasma-Atomic Emission Spectrometry (ICP-AES, in a Varian 735ES spectrometer), sodium and potassium by flame atomic emission spectrometry (FAES, in an Agilent AA 240 FS spectrometer), anions by ion chromatography (using a Dionex ICS-2000 equipment) and alkalinity by potentiometric titration(using a Metrohm Titroprocessor MOD796 equipped with a combined pH micro-electrode 6.0224.100, with a specific dynamic equivalence point titration (DET) method).

The data obtained were corrected taking into account the gravimetric water content of each sample, which was determined for each sample after a period of air drying enough to allow its crushing. All the measurements were performed in duplicate and the values given are the average of the two.

4.12 CATION EXCHANGE CAPACITY AND EXCHANGEABLE CATIONS

The Cation Exchange Capacity (CEC) is a measure of the clay surface negative charges and hence a measure of the potential retention of cations that compensate the charge imbalance. The concentration of the different cations in the exchange complex and the changes with respect to the reference sample give an indication of the geochemical reactions taking place in the solid/water system, since these changes are coupled to dissolution/precipitation and transport processes.

The CEC was measured by CIEMAT with a 0.01 M copper triethylenetetramine (Cu-Trien) solution according to Ammann et al. (2005), dispersing 0.2 g of bentonite in 25 mL of water and 10 mL of Cu-Trien (0.01 M). The standard deviation of the measurement was ±2 meq/100 g. After one hour of shaking a complete exchange of the Cu-Trien complex with the exchangeable cations was guaranteed. Afterwards, the suspensions were centrifuged at a constant rotation speed of 15,500 rpm for 20 minutes (same equipment and conditions as for the soluble salts), 3 mL of the clear solution was filled into 1-cm optical glass cuvettes and the absorbance of the solution at 578 nm was measured by using a Spectroquant VEGA 400 spectrophotometer.

The determination of the exchangeable cation population was performed by using caesium as the index cation (Sawhney 1970). Cs acts as a highly selective cation, displacing all exchangeable cations from the clay minerals if its concentration is sufficiently high. The clay samples were equilibrated at 1:8 (5 g : 40 mL) solid to liquid ratio with a solution 0.5 M of $CsNO_3$ at pH 8.2. After phase separation by centrifugation (30 minutes at 15,500 rpm), the supernatant solutions were analysed. Sodium and potassium were determined by FAES and the concentration of the rest of the major cations was analysed by ICP-AES, using the same equipment as for the soluble salts.

The concentration of chloride and sulphate was also measured in the same extracts in which the exchangeable cations were measured. This was performed with the aim of correcting the content of exchangeable cations by subtracting the soluble cations content, since the samples were not washed prior to the determination of the exchangeable cations, and the content of soluble salts in them was sometimes very high. For that, the anions measured should be coupled to the right cation. This is not always evident, firstly because the cell was hydrated with saline water, and secondly, because during the preparation of the suspensions some soluble species dissolve and the liberated cations may replace others in the interlayer, as geochemical modelling shows. This is further discussed in the corresponding subchapter.

The values obtained for CEC and exchangeable cations were corrected taking into account the water content of the samples, i.e. the values were recalculated for bentonite dry weight. All the measurements were performed in duplicate and the values given are the average of the two.

4.13 SWELLING PRESSURE AND PERMEABILITY

A custom-built high-pressure oedometer that keeps the samples at constant volume while measuring the water intake and the swelling pressure developed on saturation was used by CIEMAT to measure swelling pressure and hydraulic conductivity of two samples, S3 and S11, taken at 45 and 29 cm from the heater, respectively. It was not possible to obtain samples closest to the heater because of their incoherent state (Figure 5).

To prepare the samples, a large enough portion of each bentonite cylindrical section was cut with a knife and later adapted to the diameter of the oedometer ring by working it with a cylindrical cutter, attempting not to modify either its moisture or density. The cylindrical specimens thus obtained were then pushed inside the oedometer ring (Figure 10). The oedometer ring was 5.0 cm in inner diameter, and the hight of the specimens was ~1.5 cm.

The tests were performed in the oedometer equipment shown in Figure 11. The sample, confined between porous stainless steel sinters, was hydrated at constant volume through the bottom face with deionised water from a water column (pressure of 15 kPa), while the upper outlet remained open to atmosphere. At the same time, a load cell installed in the loading frame measured the swelling pressure exerted by the clay. The small vertical deformation of the specimen, due mainly to load cell and frame deformability, was measured by two linear strain transducers. An automatic volume change apparatus measured the water intake of the specimen. The values of load, strain and water intake were automatically recorded.

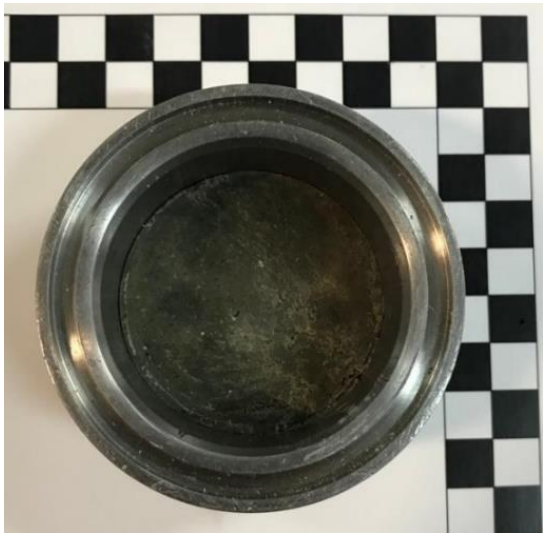

Figure 10 Appearance of sample S3 once in the oedometer ring

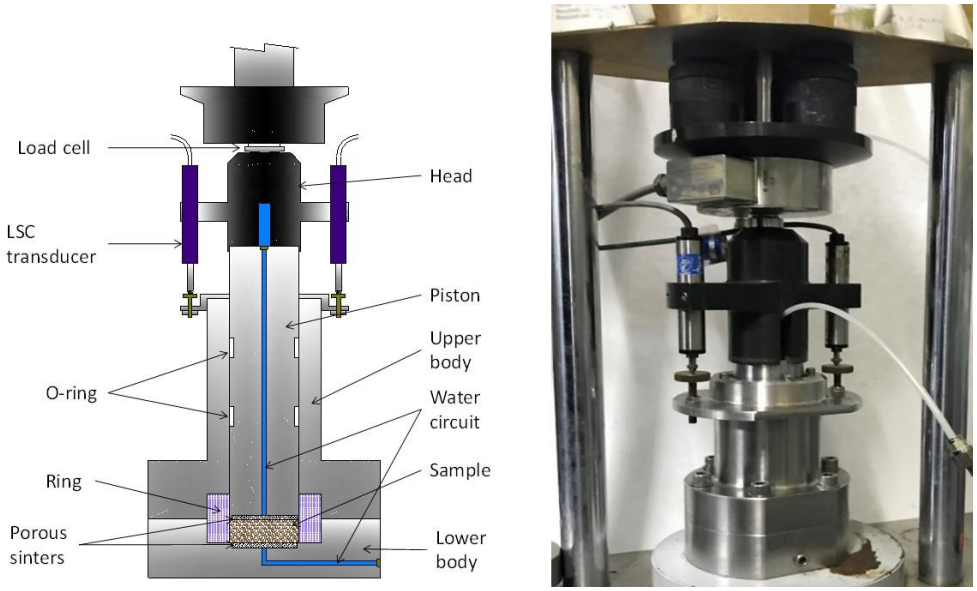

Figure 11 Schematic layout and photograph of the high-pressure oedometric equipment

After complete saturation (which was assumed by the stabilisation of water intake and swelling pressure development), the pressure registered was considered the swelling pressure value for the dry density attained. The actual density may differ slightly from the initial one due to the small displacement allowed by the equipment (about 10 µm when a vertical stress of 2.2 MPa was applied), and this was taken into account.

Afterwards, hydraulic conductivity was determined in the same equipment and on the same samples, which were kept at constant volume. In order to perform this determination, the water pressure at the bottom of the samples was increased to 1.8 and 2.0 MPa consecutively, while a backpressure of 0.6 MPa was applied on top, resulting in hydraulic gradients between 8000 and 9500 m/m. The water outflow was measured with the same volume change apparatus used to measure the water intake during saturation. The hydraulic conductivity for each gradient was calculated applying Darcy's law. After this determination the top and bottom hydraulic pressures

were reduced to 0.1 MPa and the system was left stabilise until the pressure recorded by the axial load cell did not change for several days. Deionised water was used during all the process.

On dismantling of the tests, the height of the sample was immediately checked and the water content of the specimen was determined by oven drying at 110 °C for 48 hours. The tests were performed at laboratory temperature. The procedure followed is described in detail a CIEMAT's internal standard PT-MA-04-01 Gómez-Espina & Villar 2008).

5 RESULTS

5.1 PORE SIZE DISTRIBUTION AND SPECIFIC SURFACE AREA

5.1.1 PORE SIZE DISTRIBUTION

Figure 12 and Figure 13 show the incremental curves of mercury intrusion as a function of the mean pore diameter of the diameter size intervals corresponding to each pressure increase step for the samples from the upper and lower half of the column, respectively. The curve corresponding to the initial GBM is also included. This sample was prepared trying to reproduce the same granulometry of the material placed inside the column (Figure 9) and with the same dry density (1.50 g/cm^3) as that inside the column, so it is considered that the curve obtained displays the main features of the pore size distribution of the mixture: a large volume of pores of a size larger than 100 µm and a family of pores with a mode size ~9 nm. Namely, the bentonite granulate had 69 % of pores larger than 200 nm, more than half of which were actually larger than 550 µm. Although pores larger than this size cannot be detected by MIP (and are not shown in the Figure), they were inferred following the procedure explained in Villar et al. (2021). This is a usual pore size distribution pattern for pellets mixtures (Villar et al. 2021a).

As for the samples from the upper half of the column (located at more than 24 cm from the heater, Figure 12) two major pore families could be identified, the separation between them being set at ~200 nm, approximately separating macro and mesopores. As a result of hydration the macroporosity of the GBM shifted to smaller pore sizes with respect to the original GBM (Figure 14), i.e. the largest pores were lost. The mode size of the mesopores increased with respect to the initial GBM and was similar for all samples (19.6±1.5 nm). Sample S-15, at 19 cm from the heater, showed a change in the pore size distribution pattern (Figure 13). In fact, for the samples closest to the heater (S-24 and S-25), the pore size distribution was similar to that of the original material, with a predominant mode size higher than 200 µm.

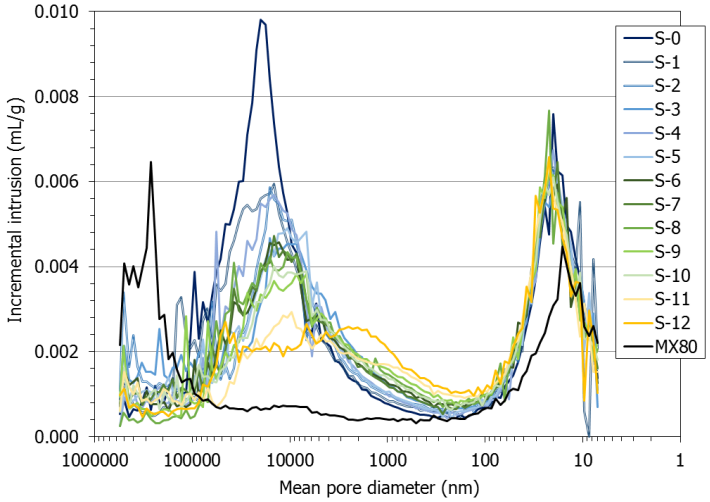

Figure 12 Incremental mercury intrusion in subsamples from the upper half of the column and of the initial GBM (see Table 2 for the location of samples)

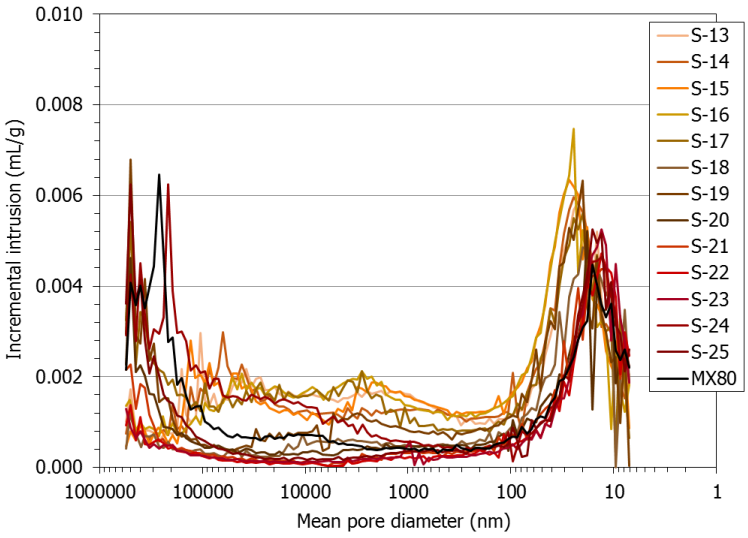

Figure 13 Incremental mercury intrusion in subsamples from the bottom half of the column and of the initial GBM (see Table 2 for the location of samples)

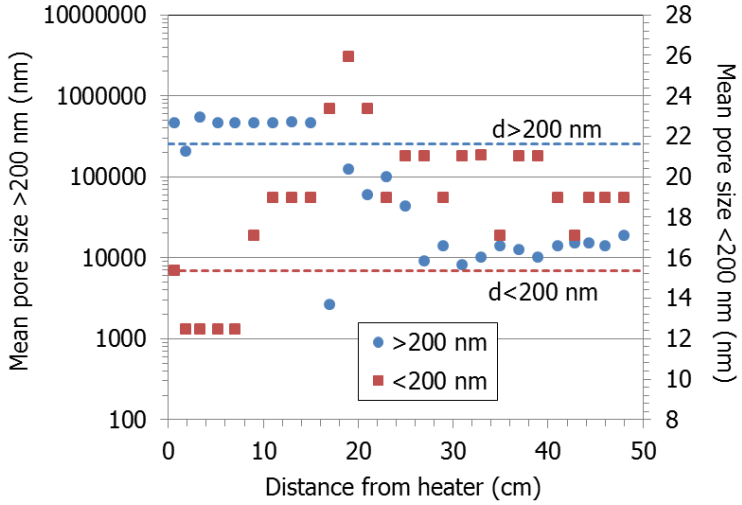

Figure 14 Mean pore size obtained by MIP in samples along the column (the discontinuous horizontal lines indicate the reference values)

The mercury intrusion method allows access to be gained only to part of the macroporosity (pores of diameter smaller than ~560 µm) and to part of the mesopores (those of diameters larger than 7 nm). The microporosity (pores of a size of less than 2 nm) is not intruded. An estimation of the percentage of pores actually intruded can be made by comparing the actual void ratio of the samples (computed from their dry density and density of solid particles) and the apparent void ratio calculated from mercury intrusion by the equipment software. Thus, the percentage of pores intruded by mercury in these subsamples was between 31 and 78 %. The non-intruded porosity is usually associated in compacted clays to the pores of a size smaller than the limit of the apparatus (~7 nm). There is uncertainty in this approach, since it is possible that pores larger than 7 nm were not intruded because of the bottleneck effect. All of the volume of such pores will be allocated to the threshold radius class of the most restricted part of the entryway, which will result in an overestimation of the smaller pore sizes volume. Likewise, although in compacted clay materials pores larger than those that can be quantified by MIP are not expected, pores of this size (i.e. >560 µm) could be present in samples from the bottom half

of the column, which were friable and crumbly. A visual inspection of the samples upon dismantling allowed to conclude that this was the case for most of them. Hence, to take into account the large pores observed in those upper subsamples, an estimation of the volume of pores larger than 550 µm was made following this approach (Villar et al. 2021a):

At the beginning of a MIP test the calibrated sample holder is filled with mercury under a low injection pressure (3 kPa). Considering the sample mass and the volumes of the sample holder and of the mercury intruded, the dry density of the sample is computed by the equipment software. This initial mercury injection is considered by the equipment as the zero value for the rest of the MIP test, which actually starts when injection pressure is increased above this value. Thus, all the large porosity filled during this initial step is disregarded. The comparison between the dry density determined by the equipment at this step and the actual dry density of the sample allows estimating the volume of pores larger than 560 µm: when the sample contains a significant volume of large pores, the dry density determined by the porosimeter is considerably higher than the actual dry density of the sample, whereas if there are not large pores the two values tend to be similar.

Taking all the above into account, the void ratio corresponding to pores larger and smaller than 200 nm (e_M and e_m, macro and micro, respectively) was recalculated, assuming that the non-intruded porosity corresponded to pores smaller than the equipment injection capacity and, in the subsamples at less than 20 cm from the heater, also to pores larger than 560 µm. The percentage of void ratio intruded, the void ratio corresponding to each pore size interval and the respective modes are shown in Table A- 1. The void ratio along the column corresponding to pores larger and smaller than 200 nm is plotted in Figure 15, along with the e_m/e_M ratio of the samples. From the hydration surface towards the bottom of the column, the void ratio corresponding to pores larger than 200 nm decreased in a continuous way until a distance of ~20 cm from the heater, whereas the void ratio corresponding to smaller pores kept in this area approximately constant and much higher than the initial one. Hence, hydration entailed an increase in the void ratio corresponding to pores smaller than 200 nm and a decrease in the void ratio of the larger ones. As a result, the ratio between e_m and e_M, increased towards the bottom of the column. However, in the 20 cm closest to the heater, corresponding to the area where the degree of saturation decreased sharply from 90 % (Figure 7), the pore size distribution gradually changed: the void ratio corresponding to macropores started to increase towards the heater, whereas the void ratio corresponding to pores smaller than 200 nm decreased sharply down to a distance of ~10 cm and then continued softly decreasing towards the heater. Indeed these changes also entailed a sudden change in the e_m/e_M ratio. In the 10 cm closest to the heater, where the sample was very dry and disaggregated, the e_m/e_M ratio was below 1 (more volume of pores higher than 200 nm than smaller). There was a transition area between 10 and 20 cm from the heater, corresponding to the unsaturated but consistent bentonite (Figure 5, sampling sections S13-S20), and at more than 15 cm from the heater the ratio was higher than 1. In fact there is a clear relation between the pore size distribution and the degree of saturation (Figure 16): as the degree of saturation increased from the initial 21 % to 90 %, e_M decreased and e_m increased, but for higher degrees of saturation the trend was reverted, with a significant increase

in e_M likely caused by the less constrained swelling of the bentonite on top of the column which was first hydrated. However, in samples with degrees of saturation lower than the initial value (those at less than 10 cm from the heater), e_m barely changed (which seems logical since there was no water content increase), whereas e_M experienced an overall decrease with respect to the initial value, likely related to the compression caused by the more wetted swelling bentonite on top.

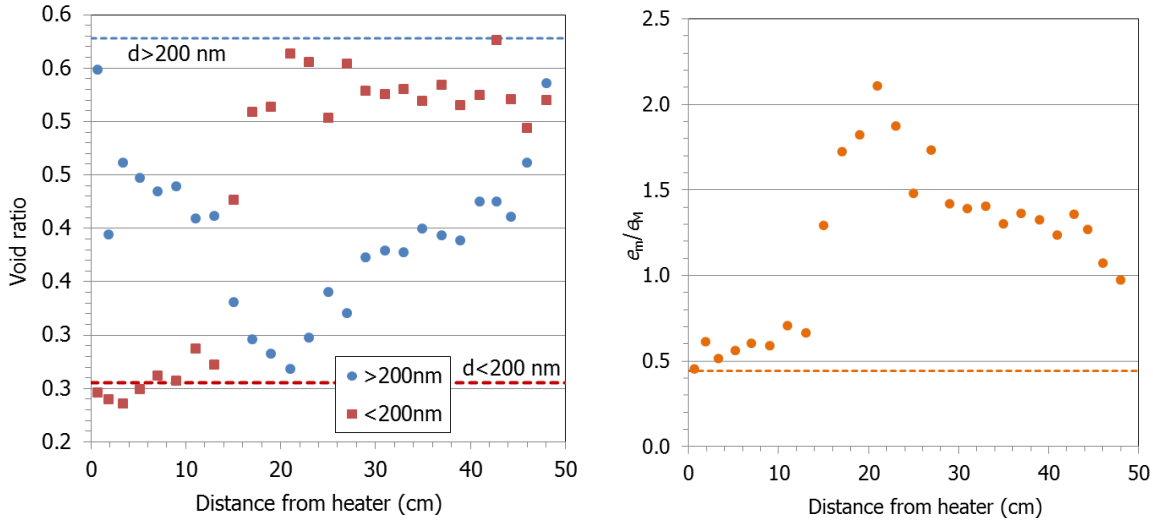

Figure 15 Void ratio corresponding to pores smaller (e_m) and larger (e_M) than 200 nm and ratio between them (the discontinuous horizontal lines indicate the reference values)

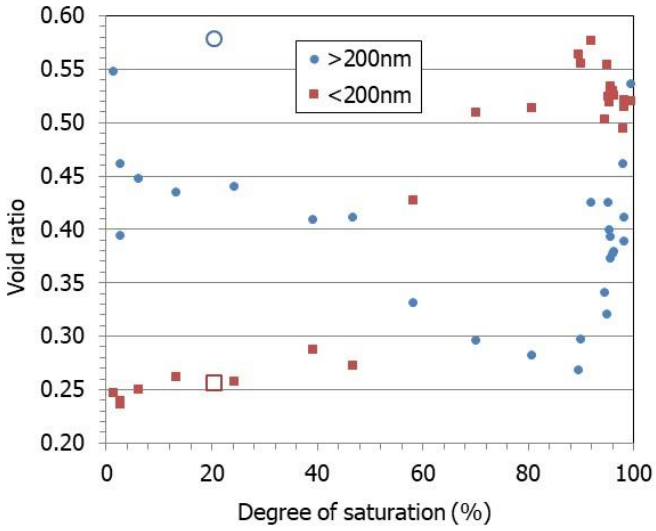

Figure 16 Void ratio corresponding to pores smaller (e_m) and larger (e_M) than 200 nm as a function of the degree of saturation of the samples. The open symbols correspond to the initial material

5.1.2 SPECIFIC SURFACE AREA

The BET specific surface area, a_s, determined in powder samples and calculated from the sorption isotherms, is shown in Figure 17 and Table A- 1. In the 30 cm closest to the hydration surface, where the degree of saturation was higher than 80 %, a_s was constant and higher than the initial value (31 m^2/g), then it decreased sharply downwards to the lowest value (17 m^2/g) at 11 cm from the heater, it increased again to the initial value and in the 5 cm closest to the heater, where

the water content was close to 0 %, decreased again. Hence, although the specific surface area of samples from TH tests has usually been seen to decrease with the decrease in water content (Villar et al. 2021b), in this case there is not a direct relation between a_s and water content (Figure 18). Indeed the samples with water content higher than 25 % and dry density below the initial value (1.50 g/cm^3) had the highest specific surface areas, but other samples with higher water content than the initial one had values below the initial reference. It is also significant that the samples with dry density higher than the initial one showed a decrease in a_s. The fact that the lowest values corresponded to samples at distances around 10 cm from the heater could indicate that continuous evaporation (through the RH3 sensor inlet, see Discussion below) had an effect on the specific surface area. The water content around the sensor was likely higher than the final one for an undetermined period of time (from the arrival of the water front to the start of leakage). Then evaporation would have caused desiccation and shrinkage in this area, hence, densification of the material and particle agglomeration, resulting in a decrease of the specific surface area with respect to the initial value.

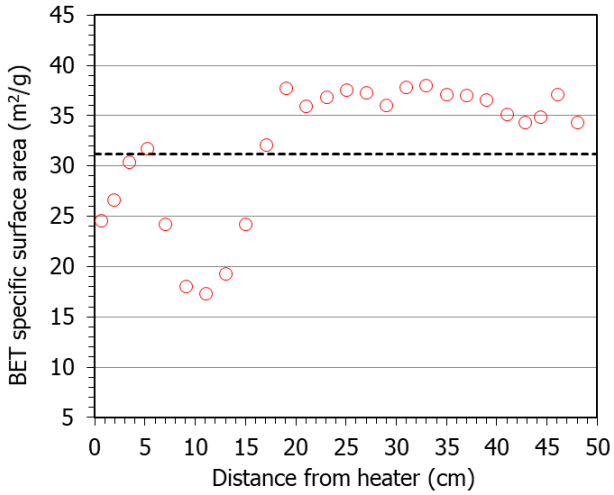

Figure 17 BET specific surface area of samples from cell HEE-B and of the initial pellets (dotted horizontal line)

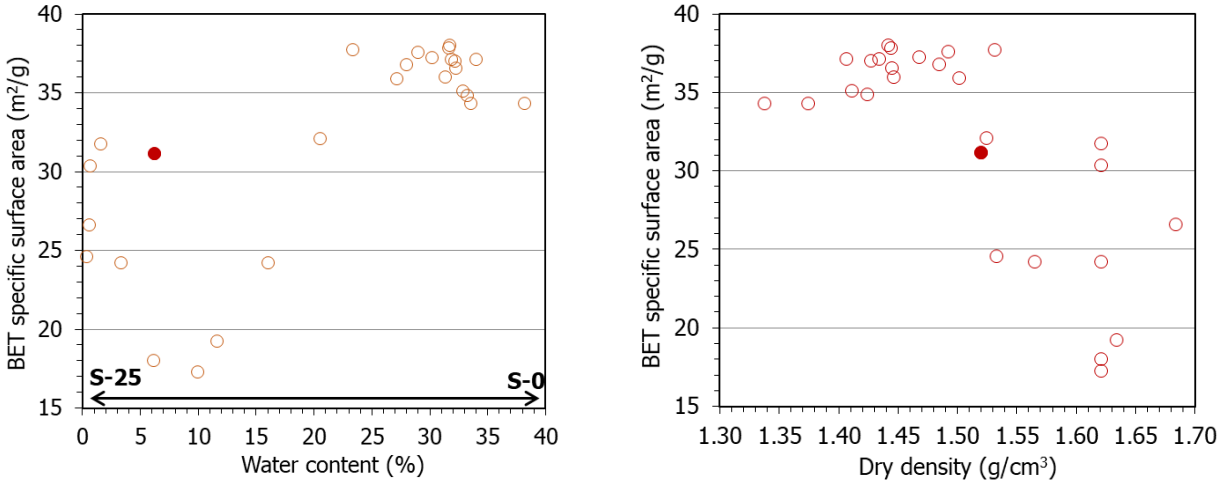

Figure 18 BET specific surface area of samples from cell HEE-B and of the initial pellets (filled symbols) as a function of water content and dry density

5.2 HYDRATION STATE (BASAL SPACING OF SMECTITE)

The basal reflection (d_{001} value) gives a measure of the interlayer distance between smectite particles, a minimum value of about 1 nm corresponding to a collapsed interlayer with no water in it. It is considered that smectites display basal reflections of about 1.25, 1.55 and 1.85 nm for the homogeneous 1, 2 and 3 water layers hydration states, respectively, the exact values mainly depending, for a given smectite type, on the exchangeable cations. Under the initial water content of the pellets (6 %), the basal spacing of the MX-80 bentonite pellets was about 1.2 nm.

The smectite basal reflection of the samples was determined from X-ray profiles recorded on a sufficiently flat surface at room temperature, without any previous treatment but trying to preserve as much as possible the water content the samples had when they were retrieved. The values obtained are plotted in Figure 19 as a function of the distance to the heater and as a function of the water content. The values measured for samples taken at more than 15 cm from the heater were in a narrow range, 1.552±0.020 nm, and corresponded to the two-layer hydration state. These samples had water contents higher than 24 %. From that distance the basal spacings decreased towards the heater and in the 5 cm closest to the heater were 0.965±0.006 nm, indicating that the interlayer was collapsed. The water content of these samples was lower than 2 %. Between 5 and 17 cm from the heater, where the samples had water contents between 3 and 20 %, the basal spacings corresponded to the 1-layer hydrate or transitions to it. Hence, there was a direct relation between basal spacing and water content.

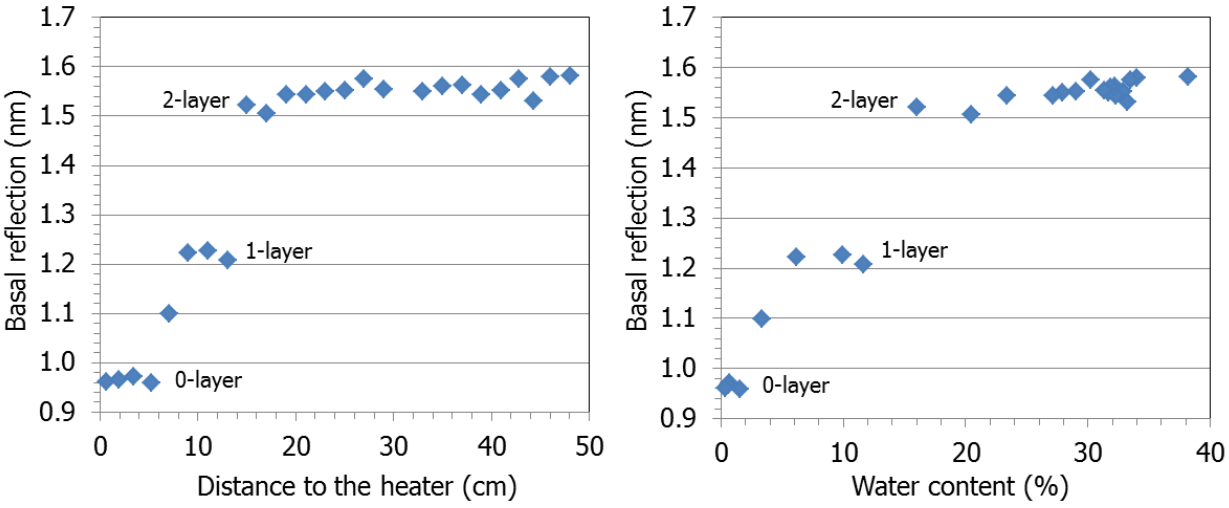

Figure 19 Main diffraction reflection of the basal spacing of untreated subsamples of test HEE-B as a function of their position inside the cell (left) and their water content (right)

In addition to these main reflections, other minor reflections could be identified from profile fitting of the XRD pattern. In the most hydrated samples the secondary reflections were towards higher basal spacings (lower angles, Figure 20), indicating the coexistence of 2 and 3-layer hydrates. In fact, the ratio between the intensities of the main and the secondary reflections increased continuously away from the hydration surface (ratio ~1) for a distance of approximately 15 cm (where the ratio was ~8), which would indicate that the contribution of the 3-layer hydrate increased towards the hydration surface. Some of these wet samples also

showed secondary reflections towards lower basal spacings (Figure 21), which could be indicating certain drying during storage, since the samples were X-rayed 3 weeks after dismantling. In the driest samples, in addition to the main diffraction peak shown in Figure 19, there was a minor one around 1 nm (Figure 22).

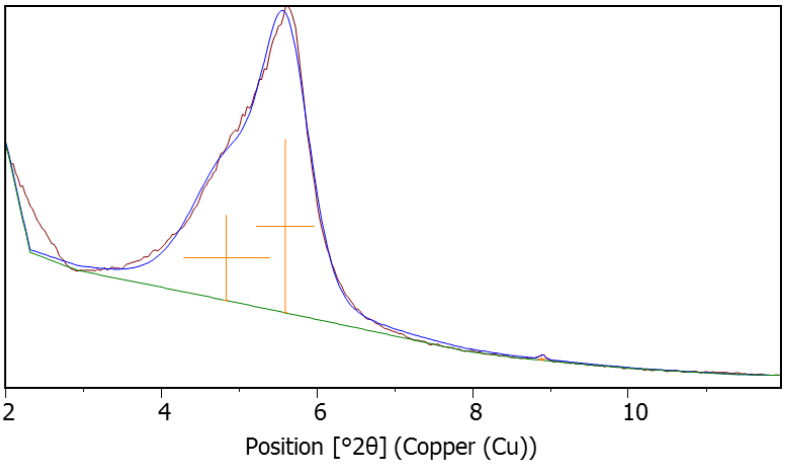

Figure 20 Profile fitting of the XRD pattern of the untreated sample S1 (46 cm from the heater)

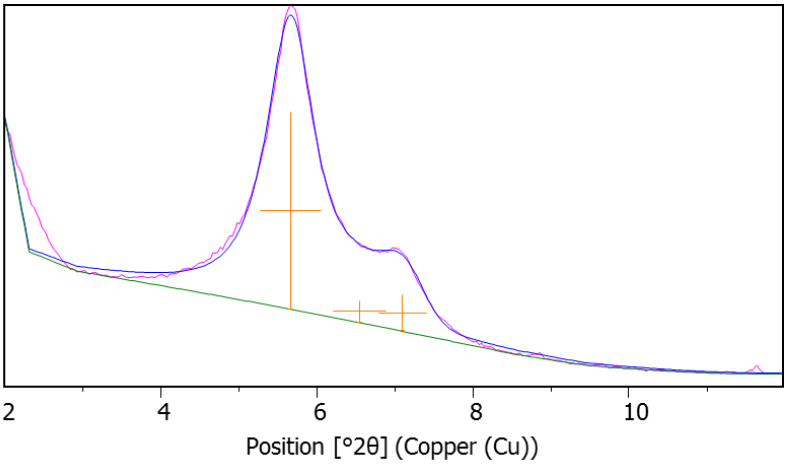

Figure 21 Profile fitting of the XRD pattern of the untreated sample S7 (35 cm from the heater)

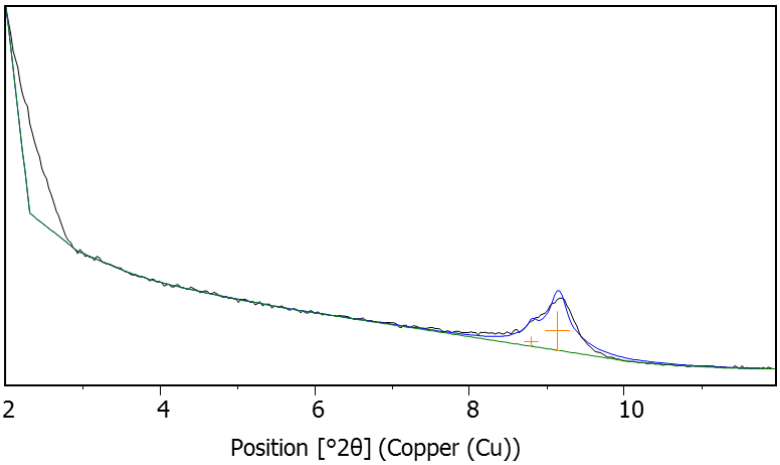

Figure 22 Profile fitting of the XRD pattern of the untreated sample S24 (2 cm from the heater)

5.3 REHYDRATION OF SAMPLES

The cell subsamples used for the determination of water content (values shown in Figure 7), were dried for two days at 110 °C and then kept protected in plastic film for 118 days. After this time the water content of some of these samples was determined again by drying them at 110 °C for two days. The average water contents were 1.3±0.2 %, very low because they had only remained in the open air for a few hours before being protected. Afterwards these samples were left in the open air of the laboratory and periodically weighed to check the evolution of water content, along with some untreated pellets that had also been previously dried at 110 °C (Figure 23). During the stabilisation period the relative humidity of the laboratory was 41±4 % and the temperature 23±1 °C. The evolution of the water content of the samples during this period is shown in Figure 24. The water content reached for all the samples an equilibrium value after ~40 days, with oscillations reflecting those in the laboratory relative humidity. Overall, the closer to the heater the sample was taken, the lower the water content it reached. The samples taken at less than 2 cm from the heater reached water contents below 4 %, which were lower than the water content of the pellets at the beginning of the TH test (6 %).

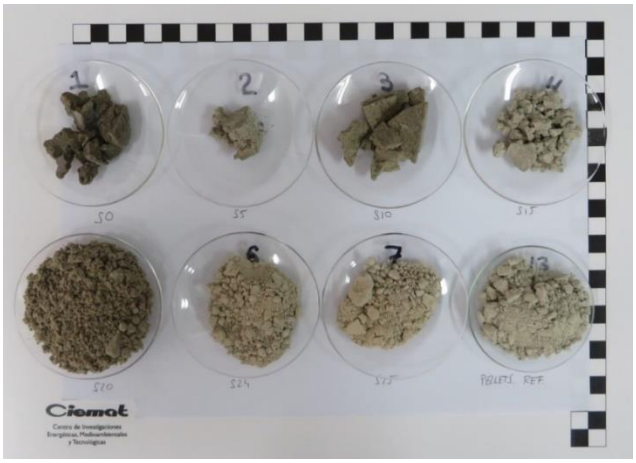

Figure 23 Samples left in the laboratory atmosphere for water content stabilisation

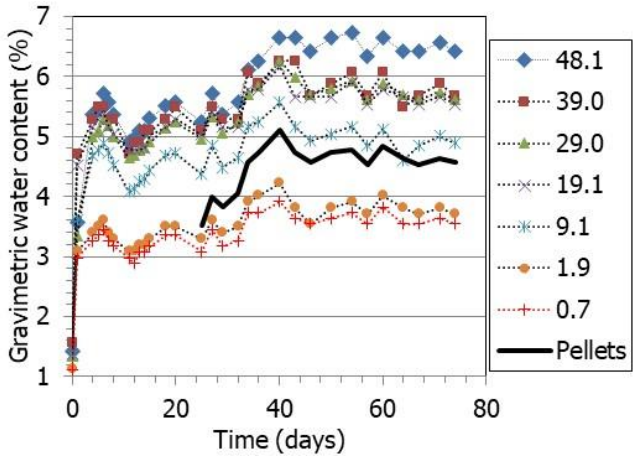

Figure 24 Evolution of water content under room conditions of samples from the HEE-B cell and of the initial pellets previously dried at 110 °C (the legend shows the distance to the heater in cm)

Afterwards (75 days after the samples had been left to stabilise in the open air), the samples were placed in a desiccator with a sulphuric acid solution of concentration 6 %, generating a relative humidity of 97 %, and they were also periodically weighed. The evolution of water content during this period is shown in Figure 25. After approximately 3 months, the samples in the desiccator had stable water contents, in all cases higher than 28 %. Even those samples that were closest to the heater reached water contents similar to that of the original, untreated pellets. Only the sample taken closest to the hydration surface reached an equilibrium water content remarkably higher than the others (32 %). There was also the sample taken at 9 cm from the heater (S20) which reached an extraordinarily high water content, maybe as a consequence of the rehydration of some deliquescent salt precipitated in this area (see subchapter 5.8).

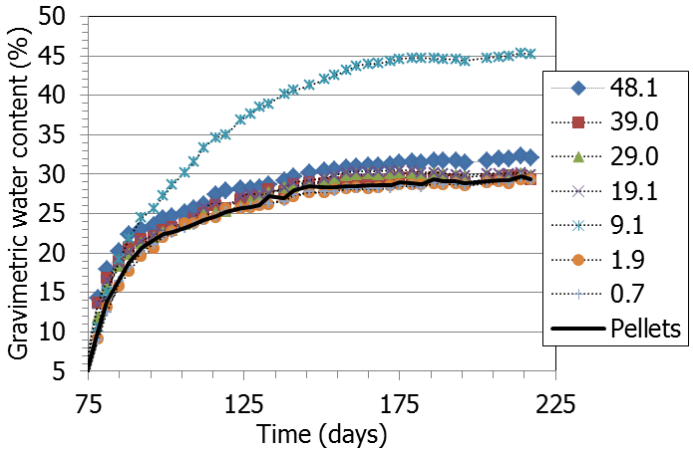

Figure 25 Evolution of water content under a RH=97 % of samples from the HEE-B cell and of the initial pellets previously dried at 110 °C and stabilized at room conditions (the legend shows the distance to the heater in cm)

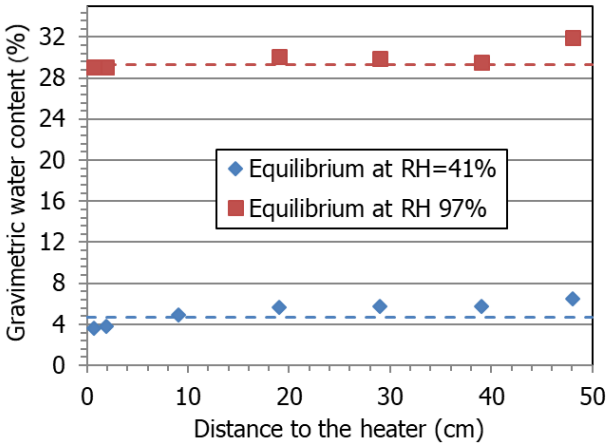

Figure 26 Equilibrium water contents for samples from the HEE-B cell under two different relative humidities (the dotted horizontal lines indicate the values for the untreated pellets)

The equilibrium water content values under the two relative humidities are shown in Figure 26 (the value corresponding to sample S20 at RH=97 % has not been plotted), which shows that, although the samples closest to the heater were not able to properly rehydrate under room conditions, when the relative humidity was high they reached approximately the same water content as the untreated pellets.

5.4 MINERALOGICAL CHARACTERISATION BY X-RAY DIFFRACTION

5.4.1 PHASE QUANTIFICATION

The X-ray patterns of the powder samples analysed are shown in Figure 27. Indeed the main mineralogical component of the bentonite is montmorillonite, with percentages likely between 70 and 80 %, although the semi-quantification of these samples was particularly difficult among other reasons because of the different hydration states commented below and the high heterogeneity of intensity ratios and apparently the type of plagioclase components. The (*hk*0) XRD random powder montmorillonite reflections near °2θ=20 and °2θ=62 corresponding to a di-octahedral smectite maintained shape and intensity in all the analysed samples. Gypsum was detected in the raw bentonite and in the samples located at distances between 10 and 44 cm from the heater, with a maximum at 17 cm from the heater (where the intensity of the 0.76 nm reflection was remarkable). Halite was present at 10 cm from the heater and the calcite reflection was seen in samples S24 and S25 (2 cm from the heater). Other minerals identified in most of the samples were plagioclase, quartz, illite, cristobalite.

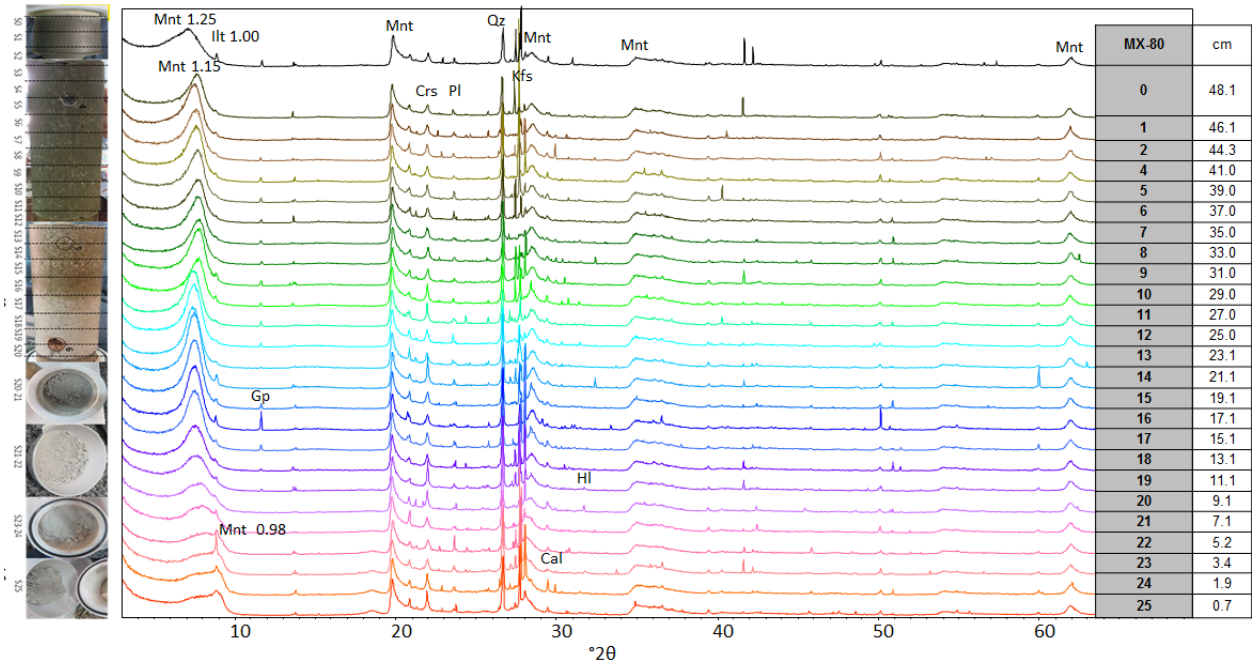

Figure 27 Random powder XRD patterns of MX-80 column samples taken at various distances from the heater (see Table 2) equilibrated for 48 h at RH 55 %. The spacing of some reflections is indicated in Å. Montmorillonte (Mnt), illite (Ill), gypsum (Gp), cristobalite (Crs), plagioclase (Pl), quartz (Qz), K-feldspar (Kfs), halite (Hl), calcite (Cal)

5.4.2 ANALYSIS OF THE BASAL REFLECTIONS

Hydration of smectite under increasing relative humidity entails a stepwise expansion, the different steps corresponding to the intercalation of 0, 1, 2, or 3 planes of H_2O molecules in the interlayer. Depending on the exchangeable cations, the basal spacings corresponding to the dehydrated layer may range between 0.97 and 1.02 nm, monohydrated between 1.16 and 1.29 nm, bi-hydrated between 1.49 and 1.57 nm, and tri-hydrated between 1.8 and 1.9 nm (Ferrage et al. 2010), the lower values corresponding to smectite with sodium as main cation in the interlayer and the higher values corresponding to predominantly divalent smectites.

The dominant basal spacing of the montmorillonite samples stabilised for 48 h at RH=55 % was between 1.11 and 1.25 nm (Figure 27), in agreement with the Na-smectite character of MX-80, although a peak shoulder towards lower angles pointed to some divalent cation substitution. In the region between 10 and 20 cm from the heater, the reflection at 1.25 nm plus a low angle shoulder were present. In the 10 cm closest to the heater, the main reflection was at 1.14 nm, a 1.0-nm illite spacing became outlined and a tail centered in 0.98 nm (dehydrated smectite) was also visible. Close to the heater, where the temperature was highest (Figure 4), a severe dehydration of the smectite structure occurred which was not recovered even after placing the samples at 55 % RH conditions for 48 h.

The basal reflections (001) of the bulk samples and of the oriented aggregates were analysed by mathematical deconvolution to identify their components. The basal reflection of the bulk samples stabilised at a relative humidity of 5 % (Figure 27) could be deconvoluted into two peaks, as shown in Figure 28. The values of these two peaks were significantly different in the samples at less than 10 cm from the heater than in the other ones. In most of the samples the main reflection corresponded to the 1-layer hydrate of a predominantly sodium montmorillonite (between 1.2 and 1.3 nm), but with a trend to increase towards the hydration surface, which would be consistent with the incorporation of divalent cations towards it. In these samples the secondary reflection had a rather constant value at 1.14±0.01 nm. However, in the four samples closest to the heater the main reflection corresponded to an incomplete 1-layer hydrate (1.1 nm) and the secondary one to the totally collapsed interlayer (0.98 nm) (Figure 29, left), which highlights their difficult rehydration under room conditions, as also the tests reported in subchapter 5.3 put forward. Nevertheless, a shoulder at 1.2 nm in sample S25 indicates some rehydration (~2 %) after equilibration under RH=55 %. The two samples in Figure 28 show also the reflection at 1.00 nm corresponding to illite.

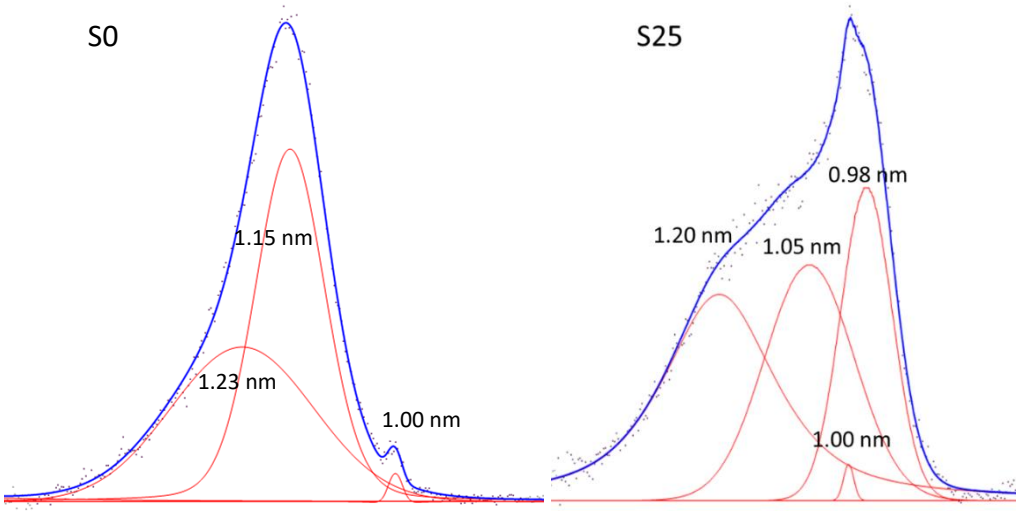

Figure 28 Deconvolution of the basal reflection in the XRD patterns of the bulk samples S0 (~49 cm from the heater) and S25 (~1 cm from the heater)

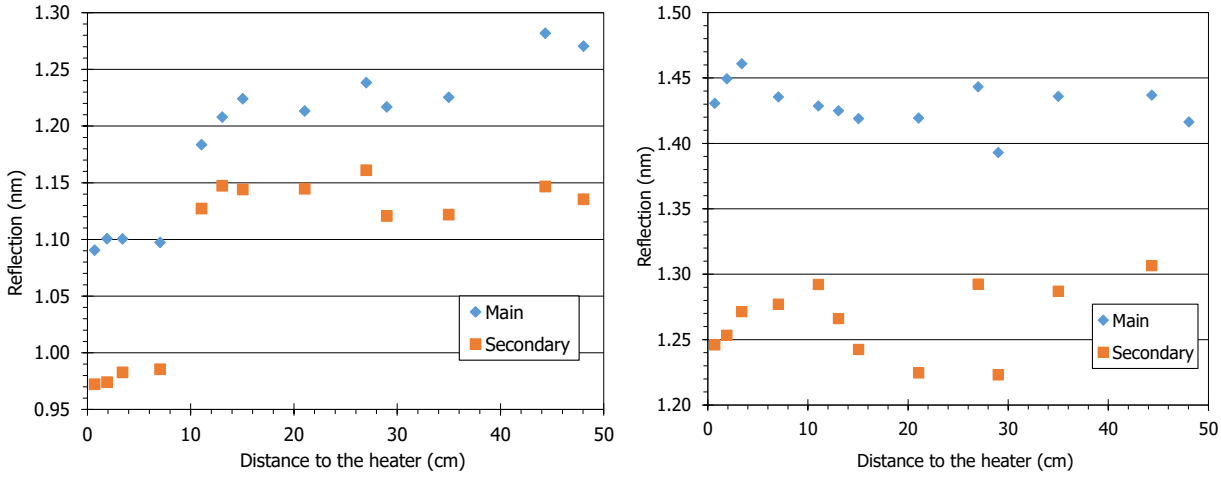

Figure 29 Main and secondary peaks obtained by deconvolution of the basal reflection of the of bulk powder samples stabilised at 50 % RH (left) and of air-dried oriented aggregates (right)

As explained in subchapter 4.4, the 0.5-µm size fraction was separated by suspension in water and centrifugation and the slurries obtained were smeared onto glass tiles to be air dried and EG solvated. The procedure involving the direct wetting of bulk samples should be valid to produce rehydration if the smectite structure was not damaged. Indeed air-dried oriented aggregates revealed the hydration state corresponding to room conditions for a montmorillonite containing both sodium and divalent cations (mainly calcium, as it will be shown below) in the exchange complex, evinced by a bimodal reflection in the basal spacing (Figure 30). Regular EG expansion was also observed (1.67±0.02 nm), as expected for an unaltered fully expandable smectite. Additionally, in the EG-OA patterns a 1.0-nm low-intensity illite reflection was identified along with the (002) 0.84-nm reflection of smectite.

Namely, the deconvolution of the basal reflection of the XRD patterns of the air-dried oriented aggregates showed in most cases four peaks (Figure 31), the two major ones being at 1.26±0.03 nm and at 1.43±0.02 nm (Figure 29, right), with no clear trend along the column. The ratio between the area of the 1.4-nm reflection (2-layer hydrate) to the 1.3-nm reflection (1-layer

hydrate) indicates the predominance of the first one, which would correspond to a divalent smectite dried at room conditions, in contrast with what was observed in the random powders of the bulk samples (Figure 29, left). The incomplete rehydration at 55 % RH of the bulk samples taken at less than 10 cm from the heater was not seen in the oriented aggregates, because the latter were performed in samples solubilised and completely hydrated before being dried at room conditions once in the glass tile. This observation is consistent with the full rehydration of all the samples (including those closest to the heater) under RH=97 % discussed in subchapter 5.3. As well, the fact that the OA patterns corresponded to divalent smectite whereas the bulk-sample patterns corresponded to sodic smectite would confirm that, during the preparation of the OA, dissolution of Ca-containing minerals (calcite, gypsum) and exchange of this dissolved calcium for sodium in the interlayer took place.

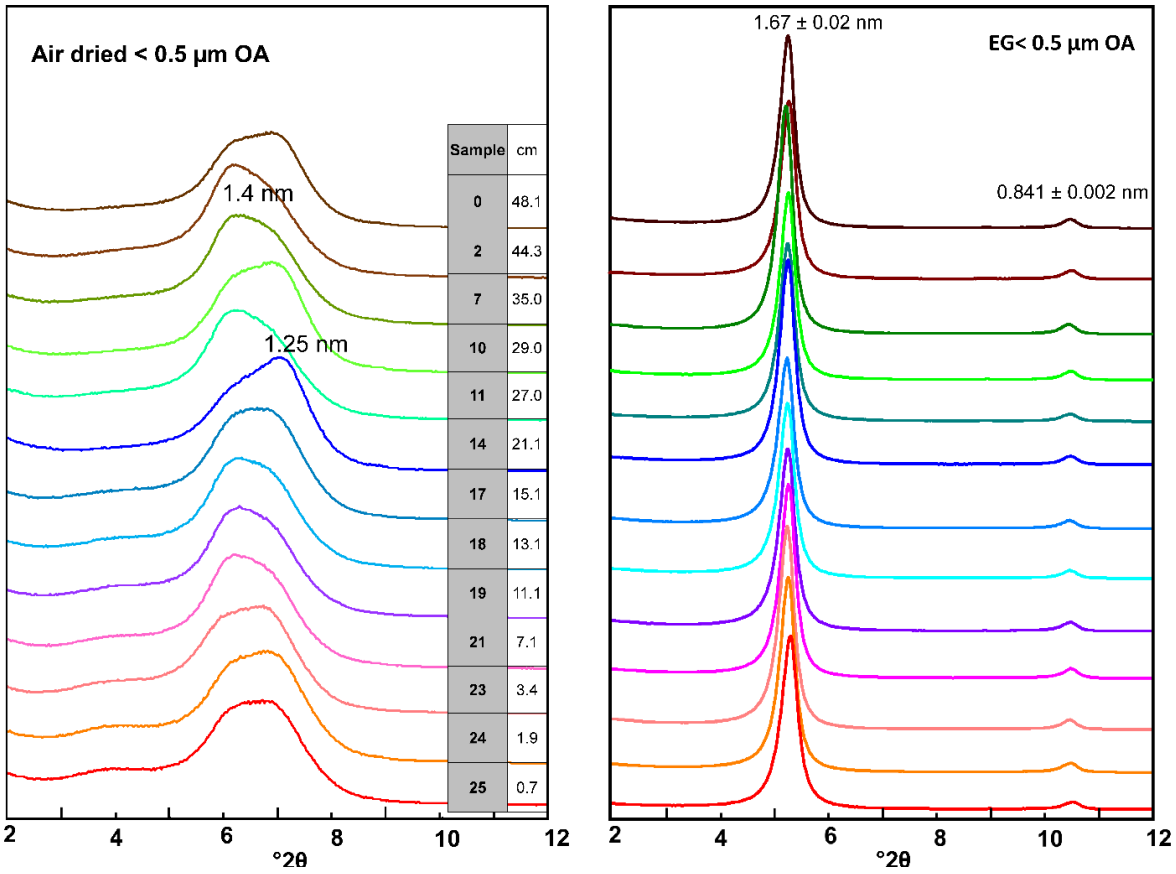

Figure 30 XRD patterns of the air dried (OA) and ethylene-glycol solvated (EG) oriented aggregates of samples taken along the bentonite column (the reference of the samples according to Table 2 and their distance to the heater is indicated)

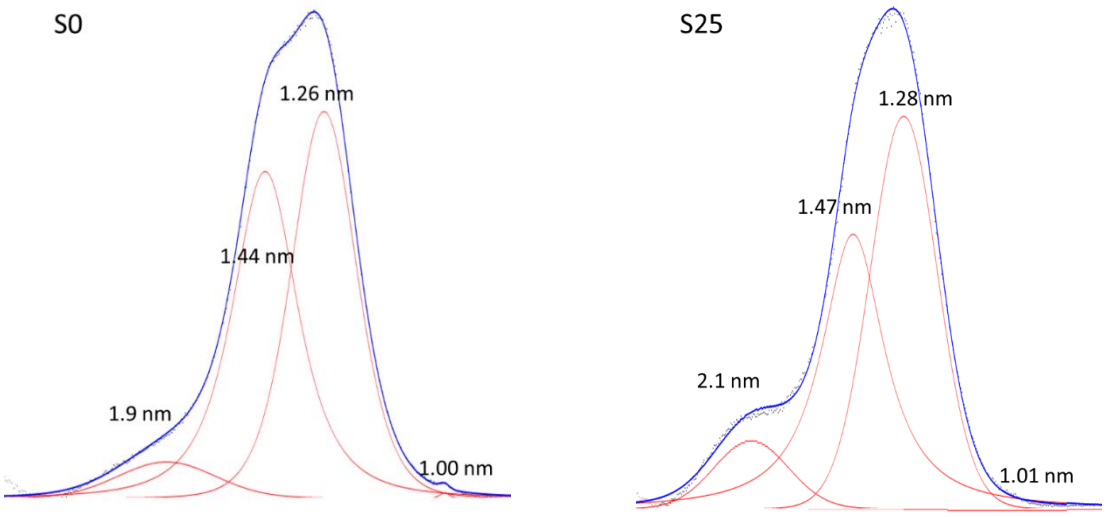

Figure 31 Deconvolution of the basal reflection in the XRD patterns of the oriented aggregates of samples S0 (~49 cm from the heater) and S25 (~1 cm from the heater)

5.4.3 CALCULATION OF STRUCTURAL FORMULAE

The analyses of major elements by XRF in the separated Ca-homoionised <0.5-µm size fraction are shown in Table 5. They were used to calculate structural formulae on a $O_{10}(OH)_2$ 2:1 sheet silicate basis (Table 6). The dry mass for extracting this size fraction obtained by using, at least, twice the two-step suspension and centrifugation method was 1-0.5 g, and frequently it was not possible to obtain a precise loss on ignition percentage to fulfil the major oxide analysis inventory using XRF. Figure 32 shows an example of XRD patterns of the random powders of this Ca-homoionised <0.5-µm fraction.

% [a]	MX-80	S0	S2	S7	S10	S11	S14	S17	S18	S19	S21	S23	S24	S25
SiO_2	66.52	68.75	67.46	69.59	68.54	68.17	68.98	67.88	67.59	67.19	67.66	67.73	67.84	67.86
Al_2O_3	22.88	21.59	22.49	21.00	21.84	22.10	21.40	22.21	22.40	22.52	22.39	22.24	22.11	22.21
Fe_2O_3	4.09	4.02	4.16	3.86	4.00	4.06	3.98	4.06	4.10	4.15	4.15	4.16	4.18	4.17
CaO	3.54	2.65	2.85	2.59	2.64	2.68	2.68	2.85	2.90	3.04	2.74	2.86	2.86	2.79
TiO_2	0.14	0.22	0.18	0.24	0.21	0.21	0.22	0.18	0.18	0.17	0.22	0.18	0.19	0.19
K_2O	0.08	0.30	0.21	0.41	0.30	0.30	0.34	0.20	0.20	0.16	0.28	0.21	0.21	0.21
MgO	2.75	2.48	2.66	2.32	2.46	2.47	2.39	2.62	2.63	2.77	2.56	2.63	2.62	2.57

[a] Major ions recalculated to sum to 100 %. P2O5 and MnO were also analysed (<0.05 %)

Table 5 XRF chemical analysis of the Ca-homoionised <0.5-µm size fraction of some samples

SITE	MX-80	S0	S2	S7	S10	S11	S14	S17	S18	S19	S21	S23	S24	S25
Si(IV)	3.93	4.00	3.97	4.00	4.00	4.00	4.00	3.99	3.98	3.96	3.98	3.99	3.99	3.99
Al(IV)	0.07	0.00	0.03	0.00	0.00	0.00	0.00	0.01	0.02	0.04	0.02	0.01	0.01	0.01
Al(VI)	1.52	1.53	1.53	1.54	1.54	1.54	1.53	1.53	1.53	1.53	1.54	1.53	1.53	1.53
Fe(VI)	0.18	0.18	0.18	0.18	0.18	0.18	0.18	0.18	0.18	0.18	0.18	0.18	0.19	0.19
Ti(VI)	0.01	0.01	0.01	0.01	0.01	0.01	0.01	0.01	0.01	0.01	0.01	0.01	0.01	0.01
Mg(VI)	0.24	0.22	0.23	0.22	0.22	0.22	0.22	0.23	0.23	0.24	0.23	0.23	0.23	0.23
Ca	0.22	0.17	0.18	0.17	0.17	0.17	0.18	0.18	0.18	0.19	0.17	0.18	0.18	0.18
K	0.01	0.02	0.02	0.03	0.02	0.02	0.03	0.02	0.02	0.01	0.02	0.02	0.02	0.02
LCh	0.45	0.37	0.38	0.38	0.36	0.36	0.38	0.38	0.38	0.40	0.37	0.38	0.38	0.37
Oct	0.38	0.37	0.35	0.38	0.36	0.36	0.38	0.37	0.36	0.36	0.35	0.36	0.37	0.36
Formulae corrected for SiO_2 and K_2O (see text and Figure 33)														
Si(IV)	3.89	3.89	3.89	3.88	3.88	3.88	3.88	3.89	3.89	3.89	3.88	3.89	3.89	3.89
Al(IV)	0.11	0.11	0.12	0.12	0.12	0.12	0.12	0.12	0.12	0.11	0.12	0.11	0.11	0.12
Al(VI)	1.53	1.56	1.55	1.56	1.56	1.56	1.56	1.55	1.55	1.54	1.56	1.55	1.54	1.55
Fe(VI)	0.19	0.20	0.20	0.20	0.20	0.20	0.20	0.19	0.19	0.19	0.20	0.20	0.20	0.20
Mg(VI)	0.25	0.22	0.25	0.23	0.24	0.24	0.22	0.25	0.25	0.26	0.24	0.25	0.25	0.24
Ca	0.23	0.19	0.19	0.19	0.18	0.19	0.19	0.19	0.20	0.20	0.19	0.19	0.19	0.19
LCh	0.46	0.37	0.38	0.38	0.37	0.37	0.42	0.39	0.39	0.41	0.37	0.39	0.39	0.38
Octch	0.35	0.26	0.27	0.26	0.25	0.25	0.30	0.27	0.28	0.29	0.26	0.27	0.28	0.27

Table 6 Calculated structural formulae ($O_{10}(OH)_2$ basis) of the Ca-homoionised <0.5-µm size fraction of some samples (IV: tetrahedral site; VI: octahedral site; Ca, K: interlayer cations; LCh: layer charge; Oct: octahedral)

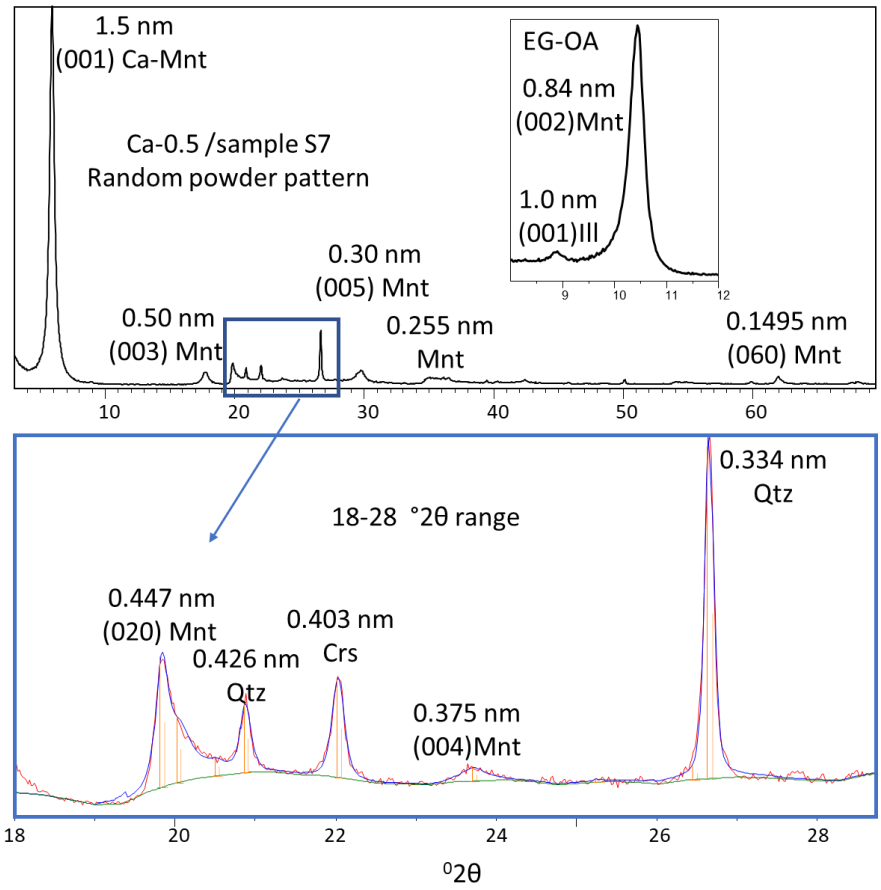

Figure 32 Random powder XRD pattern of the Ca-homoionised <0.5-µm size fraction of sample S7 (up) and detail of presence of cristobalite (Crs) and quartz (Qtz) (bottom)

The chemistry of the clay fractions in the experiment varied systematically from the reference MX-80. All the samples had more K_2O than the reference one, and the K occupation increase was related to the Ca decrease in the calculated structural formulae. The calculated Si was set to 4 in the samples in which the first calculation gave numbers above 4. Although the <0.5-µm fraction was mostly composed of montmorillonite, the enlargement of the 18-28 °2θ range shows the presence of cristobalite and quartz as fitted by Xpert Highscore Plus vs. 2.1b (2005), without any traces of plagioclase and feldspars (Figure 32, bottom). K_2O and SiO_2 were well correlated (Figure 33, left), which evinces the presence in this small-size clay fraction of both silica minerals and confirms the presence of a discrete illite-like phase, the latter in very small amounts (<2 % if illite is considered ideally as $K_{0.7}Al_2Al_{0.7}Si_{3.3}O_{10}(OH)_2$; Guggenheim et al. 2006; Nieto et al. 2010). This discrete illite-like mineral was an original accessory mineral in the MX-80 bentonite as shown by its presence both in the untreated MX-80 sample and in several samples along the column (Fig. 2, Figure 28). It would not be a new mineral produced by a progressive illitisation process, which is usually characterised by the formation of random illite-smectite mixed-layering (e.g. several examples in Meunier 2013). The areas measured in the EG-OA patterns for the illite main reflection (Figure 32, upper inset) and for the silica minerals in the <0.5-µm clay fraction random powder (Figure 32, bottom) were well correlated (Figure 33, right). In any case, this is to be taken just as a qualitative trend because the relationships between the XRD reflection areas could be perturbed by differences in preferred orientation (powder or oriented aggregates mounts) of

these mineral of very distinct habits (Dohrmann et al. 2009). The presence of these impurities in the analysed fraction does not allow a discussion of the precise changes in layer charge and cation occupancy, although compositions tend to be constant along the column with respect to the original montmorillonitic (octahedral charge predominance) character. A correlation analysis showed significant correlation among K_2O, TiO_2 and SiO_2 percentages (r>0.9, p-value<1‰), which were negatively correlated with MgO percentage (r<-0.9, p-value< 1‰), whereas octahedral Al and Fe and octahedral charge itself did not show significant correlation with any variable. This led to assume that the formulae calculated in a first trial contained accessory quartz and cristobalite related also to the presence of a micaceous (illite-like) mineral. Hence, in an attempt to obtain more reliable tetrahedral Si values in the formulae, the analyses were corrected. For that, the regression equations in Figure 33 were used, setting SiO_2 to the value corresponding to K_2O=0 and ignoring K_2O and TiO_2 (to eliminate specific cations of illite). Then, it was possible to recalculate to 100 % the percentage of the remaining cation oxides and give alternative structural formulae (bottom part of Table 6). The modified formulae showed that Ca was related to octahedral charge and Mg occupancy (Mg for Al substitutions in montmorillonite), which as expected were inversely correlated to octahedral Al (Figure 34). Iron did not relate significantly to charge.

The constancy of the values in the calculated formulae reflects minor alteration of montmorillonite along the bentonite column, with no clear trends along it.

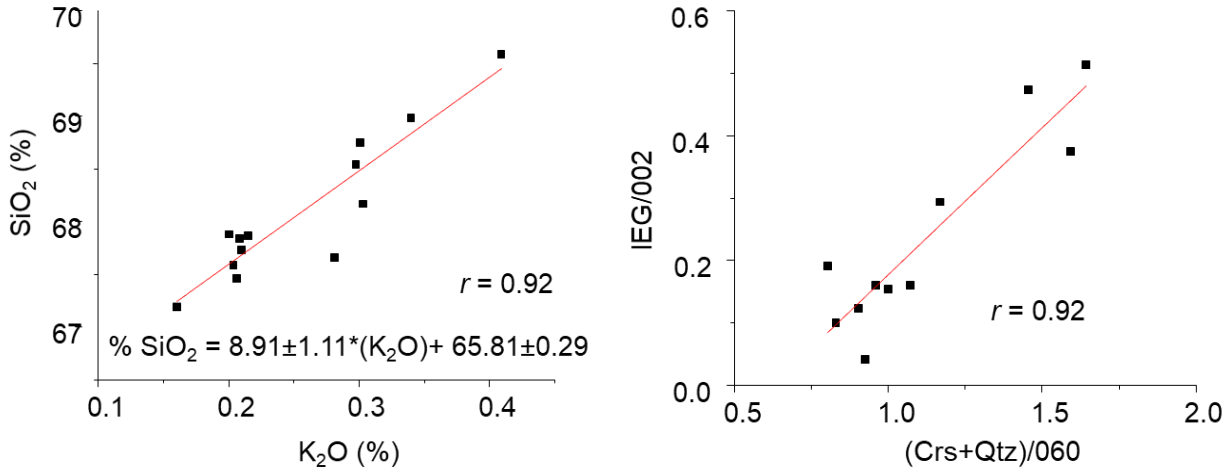

Figure 33 Linear regression for K_2O and SiO_2 in the XRF analyses (left); Area ratios of 1.0 nm illite to (002) Mnt (IEG/002) in the ethylene-glycol solvated oriented aggregate (EG-OA) XRD patterns versus cristobalite (0.403 nm) plus quartz (0.334 nm) reflection areas normalised to the (060) montmorillonite reflection areas (right)

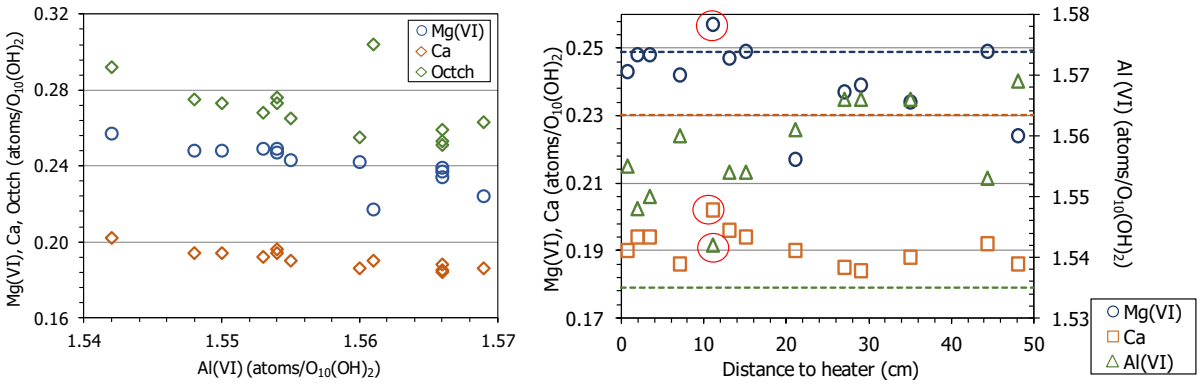

Figure 34 Ca, Mg and octahedral charge in the corrected structural formulae as a function of octahedral Al (left) and of the distance to the heater (right). The horizontal dotted lines indicate the values for the reference sample (the circled symbols correspond to sample S19, at 11 cm from the heater)

5.5 FOURIER TRANSFORM INFRARED SPECTROSCOPY

The samples were analysed by FTIR for acquiring information of the mineral composition and of the possible changes in the smectite structure. The mid-FTIR spectra of several samples analysed (including the ones closest to the hydration surface, S0, and to the heater, S25) and of the reference MX-80 are shown in Figure 35.

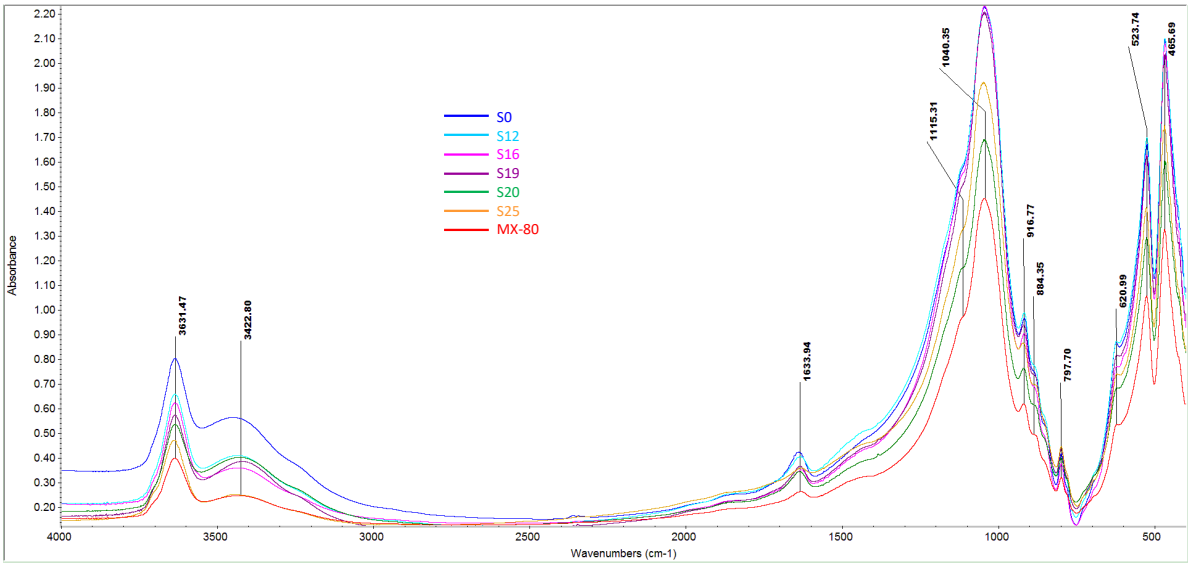

Figure 35 Mid-FTIR spectra of MX-80, as reference bentonite, and several samples from S25 (hydration zone) to S0 (heater zone)

The mid-FTIR (from 4,000 cm^{-1} to 400 cm^{-1}) absorption spectra of all samples indicates that montmorillonite is the dominant mineral phase, with the main typical dioctahedral smectite bands. The absorption band observed at 3,630 cm^{-1} followed by broad bands at 3,422 cm^{-1} and 3,240 cm^{-1} is assigned to OH stretching (ν3) of structural hydroxyl groups and water present in montmorillonite. A very sharp and intense band observed around 1,634 cm^{-1} results from the vibrations in OH group in adsorbed water. Furthermore, adsorption bands at 522, 464, and 915 cm^{-1} confirm the presence of montmorillonite. The band observed at 915 cm^{-1} is assigned to

OH deformation mode of Al-Al-OH or Al-OH-Al. The band observed at 522 cm^{-1} corresponds to ν2, the deformation mode of Al-O-Si group. The band at 464 cm^{-1} is attributed to Si-O-Si deformation. The AlAlOH band at 915 cm^{-1} is strong, whereas the $AlFe^{3+}OH$ band at 885 cm^{-1} as well as the AlMgOH band at 842 cm^{-1} are weaker, indicating the dominance of aluminium in the octahedral sheets. The band at 620 cm^{-1} is assigned to coupled Al-O and Si-O out-of-plane vibrations. Complex Si-O stretching vibration out of plane band at around 1,115 cm^{-1} and Si-O stretching vibration in plane band at 1,040 cm^{-1} are characteristic of montmorillonite.

In addition to these bands common to dioctahedral montmorillonites, other minerals are present in the samples, as indicated by a sharp band at 798 cm^{-1} with inflexion near 779 cm^{-1} that confirms the presence of quartz (Madejová & Komadel 2001) and also the absorption band at 1,430 cm^{-1}, owing to the CO_3^{2-} vibration of calcite.

Although no alterations were observed in the bulk samples, it should be highlighted that samples containing a high content of SO_4^{2-} and Ca^{2+} according to the aqueous extracts results (see subchapter 5.9), such as S16, showed bands at 659 and 594 cm^{-1} corresponding to SO_4^{2-} antisymmetric bending vibrations for gypsum (Estep et al. 1968). The MX-80 reference sample has traces of gypsum, although in low proportions that were not detected in the FTIR spectra. Figure 36 and Figure 37 illustrate the mid-FTIR spectra and the detail in the low wavelength region for sample S16.

A small band at 1,384 cm^{-1} was observed in samples S19, S20 and S21 (Figure 39). It could be due to high nitrate content (Chukanov & Chervonnyi 2016, Verma & Deb 2007) in these samples, which agrees with the results of soluble salts (Table A- 2).

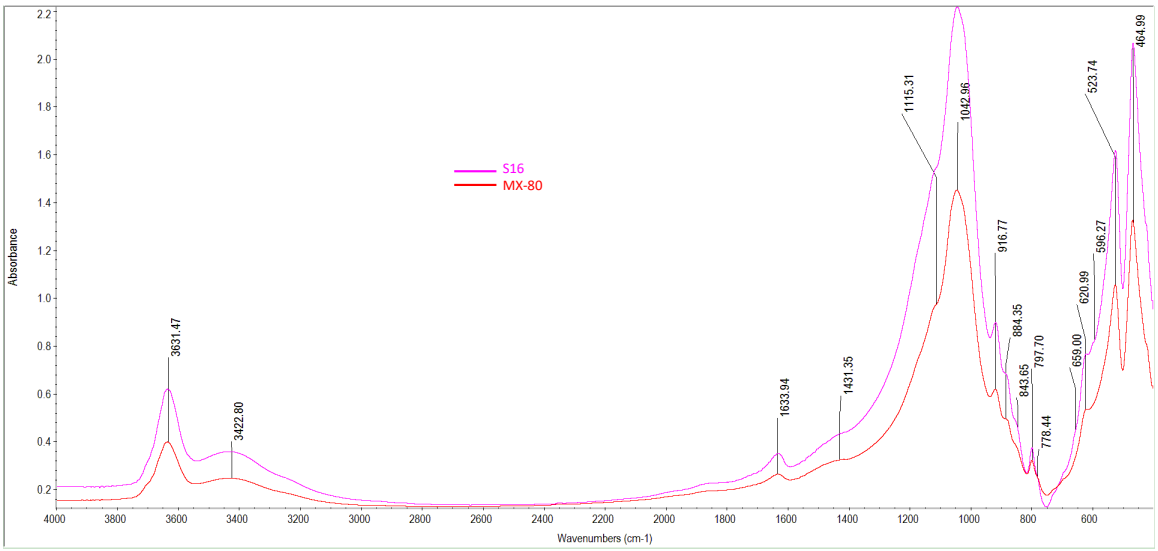

Figure 36 IR spectra of sample S16 from cell HEE-B and of the initial MX-80

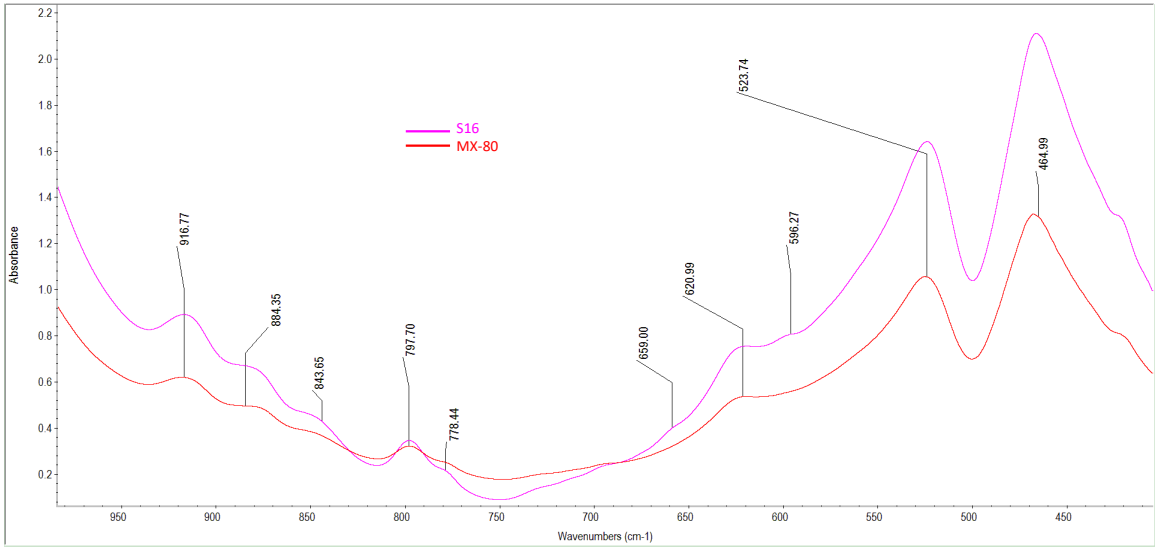

Figure 37 Detail of the IR spectra of sample S16 and the initial MX-80 in the low-wavelength region

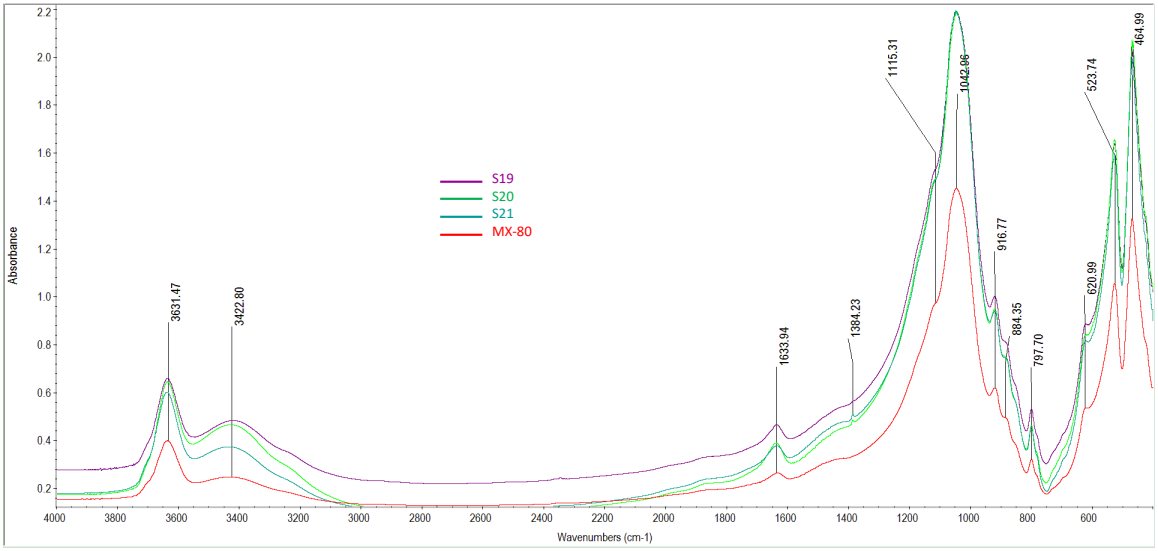

Figure 38 Mid-FTIR spectra of MX-80, as reference bentonite, and several samples S19, S20, S21

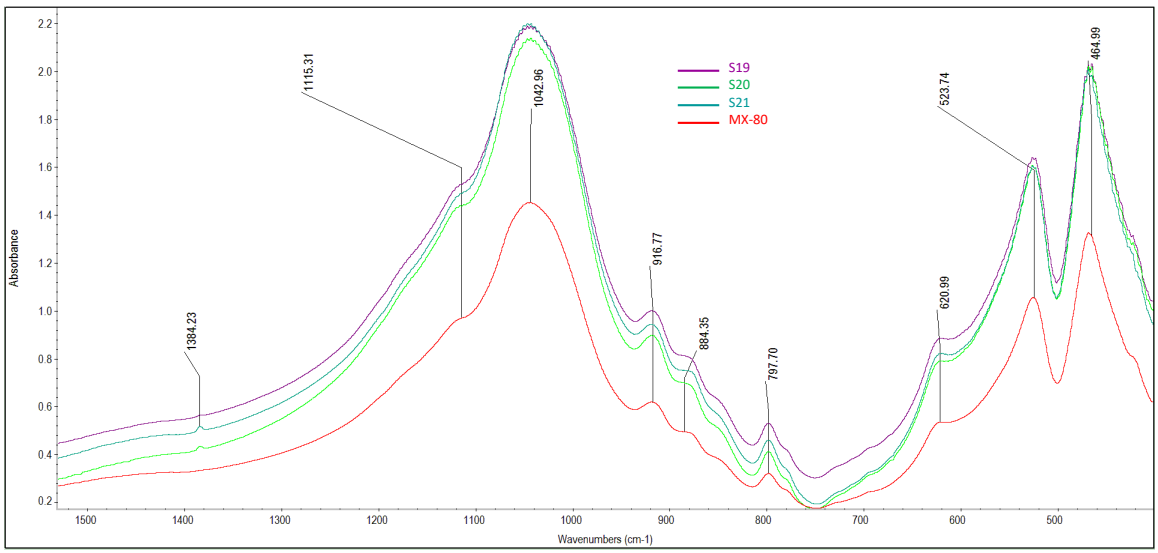

Figure 39 Detail of the IR spectra of samples S19, S20, S21 and of the initial MX-80 in the low-wavelength region

5.6 THERMOGRAVIMETRIC ANALYSIS

Differential thermogravimetric analysis (DTG) determines changes in the dehydration temperature. The patterns of some of the samples taken along the column are shown in Figure 40. The samples taken very near to the heater and close to the hydration surface (S25, S24, S0, which showed basal spacings at 1.15 nm, Figure 27) experienced a clear dehydration at 54 °C. In contrast, samples taken at distances from the heater between 10 and 30 cm (S19 to S11, in blue-green colour, with basal reflections at 1.25 nm in the random powders) exhibited an increased dehydration temperature to ~75 °C and also a 110 °C effect; all this indicated more divalent cation occupancy in the exchange complex (Caglar et al. 2009). Low intensities in the 54-75 °C dehydration peaks in samples near the heater were related to smaller water contents than in the rest of the samples, in agreement with the rehydration particularities of these samples described in subchapters 5.3 and 5.4.2. The de-hydroxylation temperature at 670-680 °C and the identical peak shape and area among the samples indicate that no relevant changes occurred in the smectite structure.

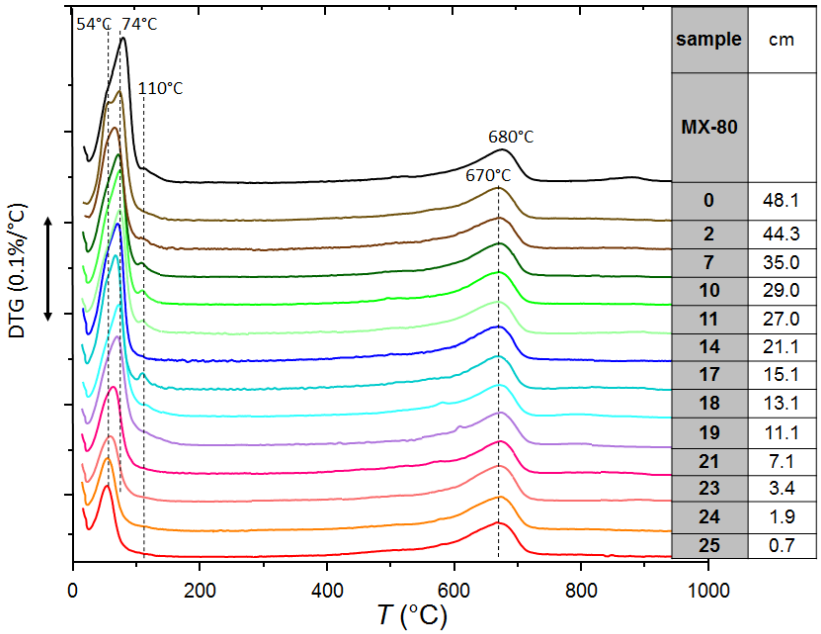

Figure 40 Differential thermogravimetric analysis data of selected samples along the HEE-B column experiment

5.7 NUCLEAR MAGNETIC RESONANCE (MAS-NMR)

The ^{27}Al MAS NMR spectra of the treated samples and of the reference MX-80 bentonite contain a central-transition resonance for one octahedrally coordinated Al site, at δ=1.5 ppm (Figure 41), related to the Al in the octahedral sheet. This central band from octahedrally coordinated Al, exhibited an asymmetric line shape with a tail to lower frequency that is characteristic of Al sites experiencing a small distribution in quadrupole coupling parameters and chemical shifts. This distribution may reflect the presence of multiple Al sites in the octahedral ^{VI}Al layer, having different surrounding environments as a result of the partial substitution of Al by Mg and Fe (Morris et al., 1990).

Besides, Al occupied sites in two tetrahedral environments (δ=58 and 70 ppm). The higher-frequency tetrahedral resonance reflects a small degree of isomorphic substitution of aluminium into the tetrahedral silicon layer, whereas the ^{27}Al signal at around 58 ppm indicates the presence of a very small quantity of an impurity phase from an $Al(OSi)_4$ site typical of the illite-like component mentioned in section 5.4 (Mantovani et al. 2009).

The ^{29}Si NMR spectra displayed the main signal at δ~-94 ppm, which is attributed to ^{IV}Si in montmorillonite and corresponds to Q^3Si (Lippmaa et al. 1980). The corresponding signal had a rather broad line indicating local disordering of the Si environment within the montmorillonite structure. The presence of a shoulder in the main signal at relative lower chemical shifts can be assigned to Q^3 [1Al] sites and indicates a low degree of partial substitution of ^{IV}Al for ^{IV}Si in the tetrahedral sheets (Sánchez et al. 2006). Signals at -101 ppm, corresponding to [(SiO), SiOH], and around -108 and -112 ppm were assigned to Q^4-^{29}Si chemical shifts (Q^4(0Al) and Q^4(1Al), respectively) of the silica polymorphs: quartz and cristobalite present in the <0.5 µm size fraction (Smith & Blackwell 1983).

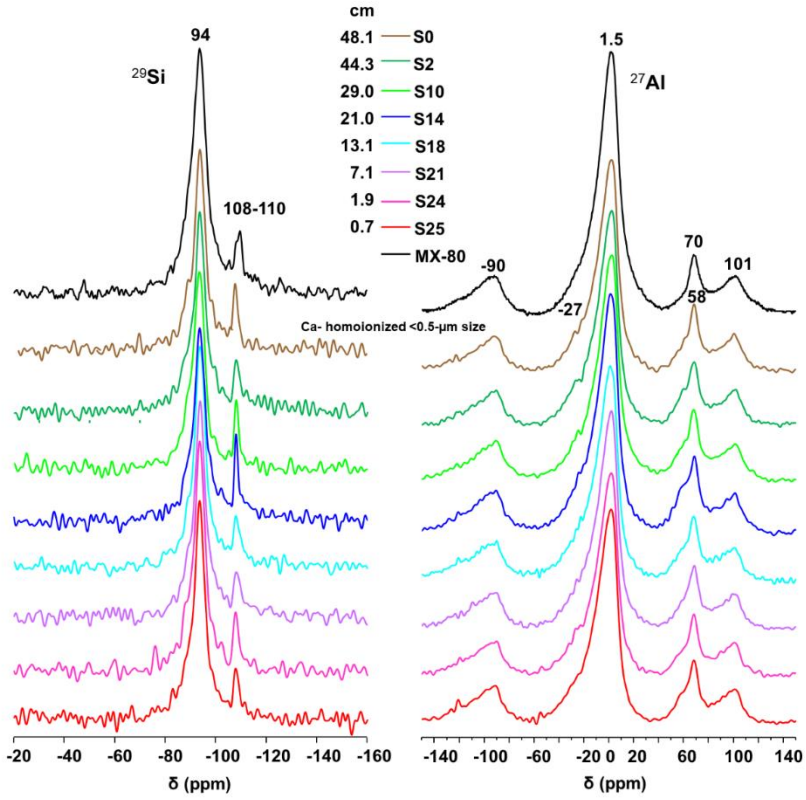

Figure 41 ^{29}Si and ^{27}Al MAS-NMR spectra for the Ca-homoionised <0.5-µm size fraction of selected samples

Summarising these observations, the NMR analyses showed that Si was in pure SiO_4 environments with Al mostly in octahedral coordination, with small tetrahedral coordination for Al replacing Si. Hence, no changes were observed with respect to the reference MX-80 montmorillonite.

5.8 SCANNING ELECTRON MICROSCOPY (SEM-EDX)

Electron microscopy observation was used to show the morphological and compositional characteristics of three main zones along the column experiment: (1) the heater contact, with loose dry pellets and bentonite powder (S25), (2) the >60 °C zone (10 cm closest to the heater), where there was evidence of difficult rehydration (S20); and (3) the hydration surface (S0).

The pellets taken from the heater contact (S25 sample) were fractured and examined. Clay surfa ces taken from fresh fracture of these dry pellets had the aspect of dense stacked laminar aggregates. In the borders of the laminar aggregates there were disperse cavities with very fine-grained coatings inside (Figure 42). Table 7 shows the localised EDX analyses taken there along with those taken in the cavity clay wall and in the clay at the border outside the cavity. The structural formulae calculated from them are shown in Table 8. The fillings or crusts in the voids contained relatively large C, Na and S proportions with respect to the clay walls of the cavities or the outer clay. These clays had greater quantities of exchangeable K and octahedral Fe than the surrounding clay analyses. In spite of the large K content they had layer charge magnitudes very similar to the average for the clay at the heater contact calculated from 12 analyses. The calculated clay formulae were in agreement with the presence of di-octahedral smectite (2 octahedral cations/$O_{10}(OH)_2$ basis). Na predominated in the exchangeable cation distribution. The tetrahedral charge was greater than those calculated from XRF analysis in the Ca-homoionized <0.5-µm fraction shown in Table 5. The values obtained by EDX should be taken as an approximation, because some Mg could be allocated to the interlayers and the octahedral charge might rise (García-Romero et al. 2021). Sulphur was present in small quantities in the clay; dispersed spots (<1 µm in size) were identified as pyrite (FeS_2).

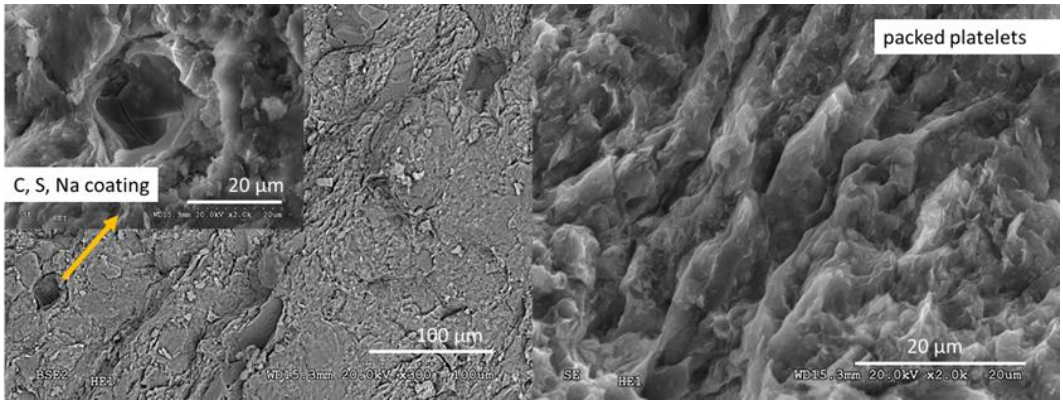

Figure 42 SEM-EDX observation at the heater contact (S25 sample): scattered cavities with fine grained coatings (left); dense stacked clay aggregates fabric in the heater zone (right)

ELEMENT (%)	FILL	WALL	OUT	BULK
C	55.42±3.51	9.80±0.44	11.66±0.55	10.75±1.50
O	36.25±2.80	62.00±7.16	64.65±1.67	65.79±2.71
Na	1.39±0.40	0.96±0.01	1.18±0.18	1.09±0.15
Mg	0.15±0.13	0.95±0.24	1.01±0.01	1.06±0.10
Al	1.38±1.41	8.02±1.52	6.43±0.01	6.58±0.61
Si	2.83±2.83	16.32±4.29	13.87±2.14	13.57±1.70
S	1.49±0.46	-	-	-
K	0.24±0.29	0.15±0.13	0.18±0.05	0.20±0.11
Ca	0.69±0.60	0.41±0.08	0.30±0.06	0.05±0.06
Fe	0.21±0.21	1.38±0.51	0.75±0.21	0.05±0.06
Ca/Na	0.45±0.30	0.43±0.09	0.25±0.02	0.22±0.10

Table 7 SEM-EDX localised analyses in sample S25. Fill: inside cavity; Wall: cavity rim; Out: external clay surrounding cavity; Bulk: clay analyses in the dense aggregates. 3 analyses in cavity zones and 12 analyses in the dense clay aggregates matrix

SITE	WALL	OUT	BULK
Mg(VI)	0.21±0.00	0.27±0.03	0.29±0.04
Al(VI)	1.51±0.04	1.51±0.02	1.52±0.05
Fe(VI)	0.31±0.04	0.21±0.08	0.24±0.03
Al(IV)	0.32±0.06	0.24±0.20	0.28±0.13
Si(IV)	3.68±0.06	3.76±0.20	3.72±0.13
K	0.04±0.01	0.05±0.01	0.02±0.02
Ca	0.09±0.00	0.08±0.01	0.06±0.03
Na	0.22±0.05	0.32±0.02	0.31±0.06
LCh	0.53±0.04	0.42±0.13	0.33±0.21
Sumoct	2.03±0.00	2.00±0.09	2.05±0.05

Table 8 Structural formulae calculated from the SEM-EDX localised analyses in sample S25 shown in Table 7. Fill: inside cavity; Wall: cavity rim; Out: external clay surrounding cavity; Bulk: clay analyses in the dense aggregates. Ca, Na, K: interlayer cations; LCh: layer charge ($K+(2xCa)+Na/O_{10}(OH)_2$); Sumoct: sum of octahedral cations

Sample S20 (taken at 9 cm from the heater) was characterised by the bright patched surfaces corresponding to NaCl glassy coatings (Figure 43 a). These coatings did not have the typical euhedral crystalline cubic morphologies expected from NaCl crystallization. This would mean that fast precipitation was involved in the formation of these coatings. Gypsum was detected inside the relatively dry pellets (Figure 43 d), as well as in the more hydrated samples S17 and S19 (e.g. Figure 44). The chemical analyses of clay zones in samples S0 and S20 are presented in Table 9. The structural formulae calculated from them were corrected for sodium chloride and they were very similar to those obtained previously with no indication of crystal-chemical changes in this saline environment (Table 10).

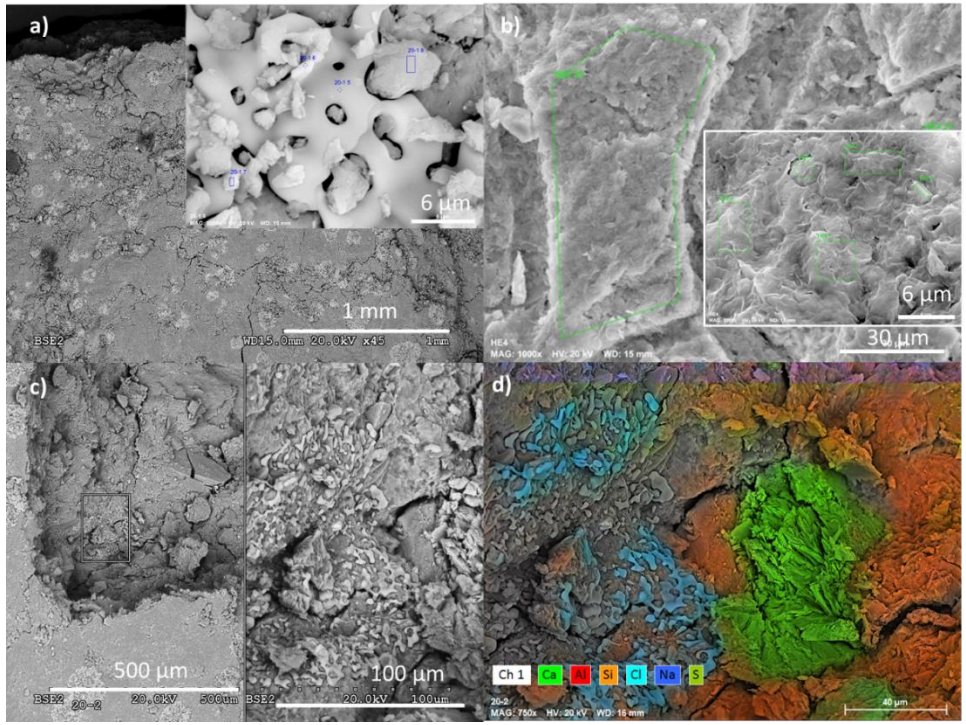

Figure 43 SEM-EDX examination of clay pellets at 9 cm from the heater (sample S20) and at the hydration surface (sample S0); a) S20 pellet surface and detail of NaCl glassy morphology coatings; b) hydration zone with filter cellulose fibres marks and detail of typical smectite platelets fabric; c) backscattered electron images of S20 pellets showing glassy NaCl coatings also inside a broken pellet; d) EDX characteristic X-rays used to outline colours corresponding to NaCl and $CaSO_4$ precipitated around cracks and plate-like discontinuities within the pellets (Ch1: backscattered electron background image channel)

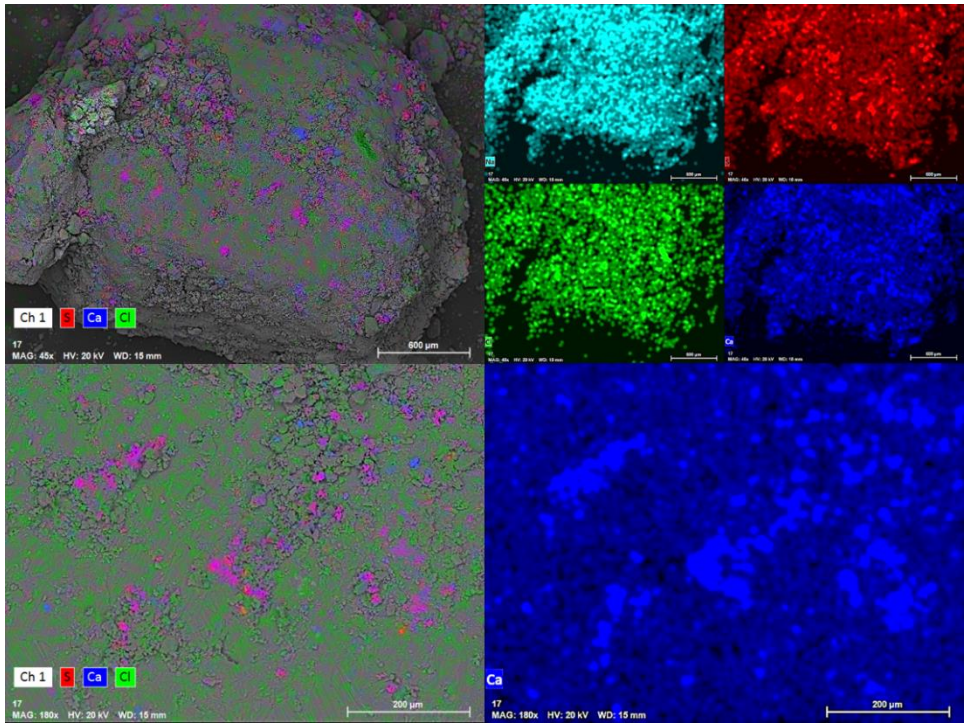

Figure 44 NaCl and $CaSO_4$ (presumably hydrated) in pellets surface of sample S17. Purple grains are calcium sulphate as detailed in the bottom photographs (Ch1: backscattered electron background image channel)

ELEMENT (%)	S20	S0
C	10.01±1.67	11.18±1.67
O	60.85±5.86	62.15±2.99
Na	1.71±0.83	1.84±0.29
Mg	1.26±0.26	1.23±0.20
Al	7.84±2.26	6.87±0.81
Si	16.38±3.02	14.23±1.84
S	0.14±0.00	0.43±0.31
Cl	0.83±0.87	0.37±0.26
K	0.03±0.05	0.30±0.38
Ca	0.26±0.16	0.50±0.30
Fe	0.85±0.16	0.80±0.19
Zn	-	0.72±0.24
Ca/Na	0.16±0.10	0.27±0.15

Table 9 Average and standard deviation for 6 and 12 SEM-EDX analyses performed in the clay materials of samples S20 and S0, respectively

SITE	S20	S0
Mg(VI)	0.29±0.02	0.32±0.05
Al(VI)	1.58±0.08	1.44±0.08
Fe(VI)	0.19±0.07	0.21±0.04
Al(IV)	0.21±0.07	0.34±0.07
Si(IV)	3.79±0.16	3.66±0.07
K^a	0.02±0.04	0.03±0.08
Ca^a	0.05±0.04	0.13±0.07
Na^a	0.19±0.07	0.49±0.13
LCh	0.31±0.25	0.67(^{a})±0.25
Sumoct	2.06±0.10	1.96±0.09

Table 10 Structural formulae calculated from the SEM-EDX analyses shown in Table 9: Na, Ca, K: interlayer cations; Sumoct: sum of octahedral cations; LCh: layer charge (K+(2xCa)+Na/$O_{10}(OH)_2$)

Fragments from sample S20 were also analysed after they had been dried at 110 °C and then allowed to rehydrate first under ambient conditions and then under a relative humidity of 97 %, following the procedures described in chapter 5.3. The sample from this section took much more water than the rest of samples (Figure 25) and for this reason it was analysed by SEM. Some of the images taken are shown in Figure 45 and the corresponding analyses in Table 11. These analyses show that Ca and S are close to stoichiometry 1:1 of anhydrite or gypsum (a, b). The image in Figure 25c corresponds to a platy morphology with Na, Mg, Ca polycationic salt composition (disordered phases that would take water).

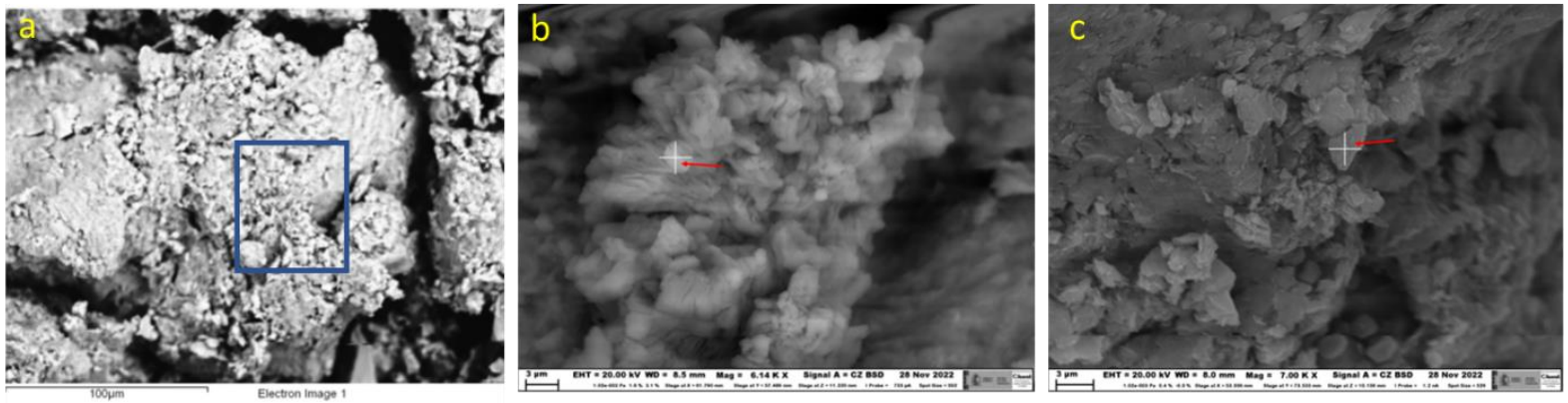

Figure 45 Detail of SEM polycrystalline aggregate morphologies rich in Ca, S and Cl characteristic of soluble salt composing elements in S20 sample after drying at 110 °C and rehydrating under RH=97 % (a, b: carbon coating; c: gold coating)

ELEMENT (%)	a	b	c
C	10.08	-	-
O	79.79	89.90	77.19
Na	-	0.08	0.56
Mg	-	-	0.43
Al	0.43	0.20	2.57
Si	0.97	0.44	7.76
S	4.67	5.04	2.99
Cl	-	0.05	0.65
Ca	4.06	4.26	6.75
Fe	-	0.02	1.11
S/Ca	1.15	1.18	0.44
Cl/Na	-	0.63	1.16

Table 11 SEM-EDX analyses performed in sample S20 after heating and rehydration at the locations indicated in Figure 45 (a: area analysis; b, c: localised analyses)

The sample closest to the hydration surface (sample S0) was composed of a homogeneous clay material in which the clay aggregates borders were not easily distinguished (Figure 43b). Fresh fractures revealed polygonal honeycomb textures typical of low-density porous zones in smectitic clays (Fesharaki et al. 2007). These zones and the hydration contact surface (in which cellulose fibres from the filter paper remained), were analysed by EDX once the cellulose filter had been removed (Table 9). Clay formulae, calculated from EDX analyses, were in agreement with the presence of di-octahedral smectite (2 octahedral cations/ $O_{10}(OH)_2$ basis). The Ca/Na ratio in the analyses of the hydration zone was greater than at the heater zone (bulk sample S25), although Na predominated. The Na and Ca contents were large compared to those at the heater zone. Tetrahedral charge predominated slightly over octahedral. Zinc was probably leached from the metallic parts of the water inlet connections and was observed to have precipitated as chloride and sulphate. The structural formulae of sample S0 are also compatible with montmorillonite, although it was not possible to apply a reasonable correction because the layer charge was too high to be consistent with the previous data. Small spots (<1 µm in size), bright under back-scattering electron mode, with pyrite composition were also observed at numerous locations in this zone.

5.9 ELEMENTAL ANALYSIS

The contents of C, H and S in the samples along the column obtained by elemental analysis are shown in Figure 46. Sulphur measurements are uncertain because of the technique limitations and the low contents. It peaks at 9 and 17 cm from the heater, but with a decreasing trend towards it. The maximum at 17 cm agrees with the presence of gypsum detected by XRD and the high concentration of soluble sulphate (see section 5.10). A significant decrease of H towards the heater, starting 10 cm away from it, would be related to the dehydration of the montmorillonite in this zone commented above.

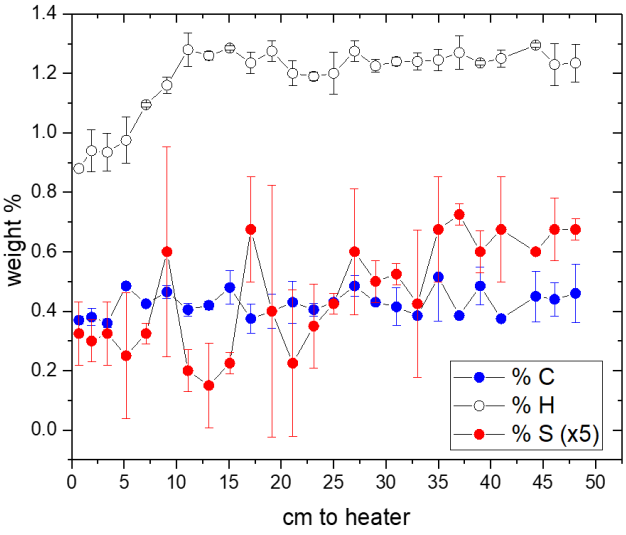

Figure 46 Elemental analysis of samples along the column (note that S contents have been multiplied by 5)

5.10 AQUEOUS EXTRACTS: SOLUBLE SALTS

The concentration of ions measured in the aqueous extracts of the samples is shown in Table A-2, in which the values obtained for the reference MX-80 pellets are also shown. The main ions in the aqueous extracts of the untreated MX-80 pellets were sulphate and sodium (with a ionic strength of 0.02 mmol/L). The modelling of aqueous extracts in similar experiments shows that part of the sodium could in fact come from the interlayer, because during the suspension of the bentonite in deionised water, calcium coming from the dissolution of soluble species (e.g. sulphates) would replace sodium in the interlayer (Idiart et al. 2022). However, this process might have not been too relevant in the aqueous extracts prepared with samples from cell HEE-B, since the bentonite column was hydrated with a quite saline water, containing mainly sodium and chloride (Table 1). Indeed the average amount of these two ions increased with respect to the initial content: the average Na^+ content in the column after the test was 19.9 meq/L and the Cl^- content was 7.0 meq/L, whereas the initial values were 17.0 and 0.4 meq/L, respectively. The fact that the increase in chloride was much more significant could indicate that part of the sodium content measured in the aqueous extracts of the initial material actually corresponded to exchangeable sodium.

The average amount of calcium, magnesium and potassium ions clearly increased with respect to the initial material, as did that for sulphate. The solubilisation of mineral species by the increase in water content, along with the input of ions with the hydration water would be responsible for the overall increase in ions content. Bicarbonate was the only ion that decreased on average with respect to the initial value.

Figure 47 and Figure 48 show the concentration of the main cations and anions along the bentonite column. As it has been explained above, and given the composition of the hydration water, the overall content of most ions increased all along the column, but most significantly in the region between 5 and 20 cm from the heater. Only potassium and bicarbonate (in minor concentrations in the hydration water, see Table 1) decreased in the uppermost 30 cm of the column, whereas sulphate remained in this area in concentrations similar to the initial one, except in the 5 cm closest to the hydration surface, where it decreased. The concentration of all the cations peaked at two different distances from the heater, at between 9 and 11 cm (closer to the heater for Ca^{2+} and Na^+) and at 17 cm from the heater. However, the anions behaved differently, since Cl^- peaked just at 9 cm from the heater and SO_4^{2-} at 17 cm from it. It is worth mentioning that the concentration peak closest to the heater coincided with the location of sensor RH3 (indicated in the Figures with dotted vertical lines), which was found corroded and not well sealed (Villar et al. 2022). From this location towards the heater, the concentration of all the ions decreased, reaching minima at 5 cm from the heater, and then increased again. In the case of sulphate the minimum concentration region spanned from 5 to 13 cm from the heater. In contrast to the rest of the ions, bicarbonate, which was below its initial concentration in most of the column, started to increase at 17 cm from the heater towards it and reached greater values than the initial one in the 5 cm closest to the heater.

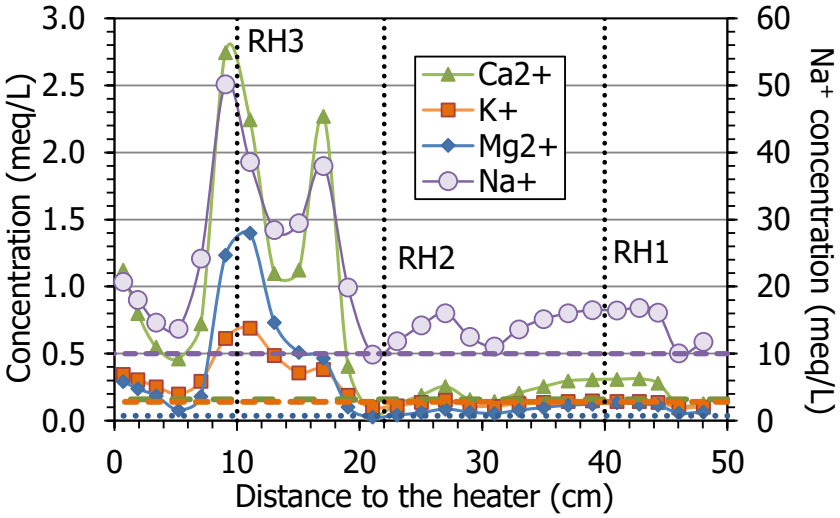

Figure 47 Main cations measured in aqueous extracts of samples of cell HEE-B (the horizontal lines indicate the concentrations in the untreated pellets and the vertical dotted lines the positions of the sensors)

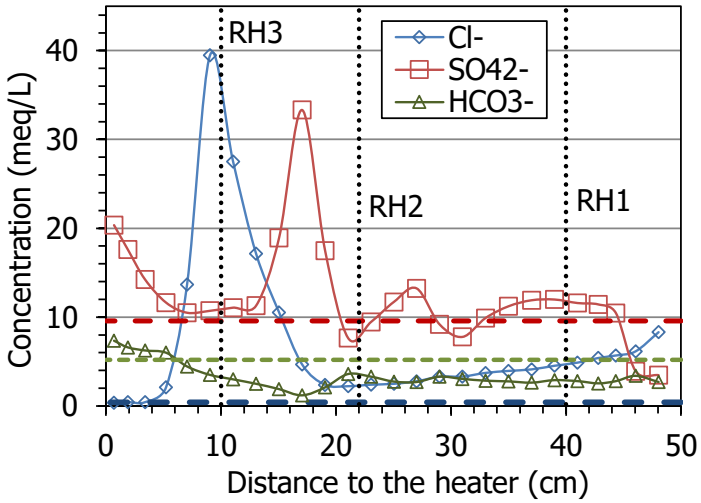

Figure 48 Main anions measured in aqueous extracts of samples of cell HEE-B (the horizontal lines indicate the concentrations in the untreated pellets and the vertical dotted lines the positions of the sensors)

To counterbalance the huge sodium concentration, chloride and sulphate have to be summed up, otherwise there is a significant excess of sodium (except at 9 cm from the heater, Figure 49). The balance is slightly improved if not only sodium, but also the rest of the cations (Mg^{2+}, Ca^{2+} and K^{+}) are considered. However, close to the heater there was an excess of cations (Na^{+}) with respect to sulphate, which are counteracted by inorganic carbon anionic species (bicarbonate in aqueous extracts).

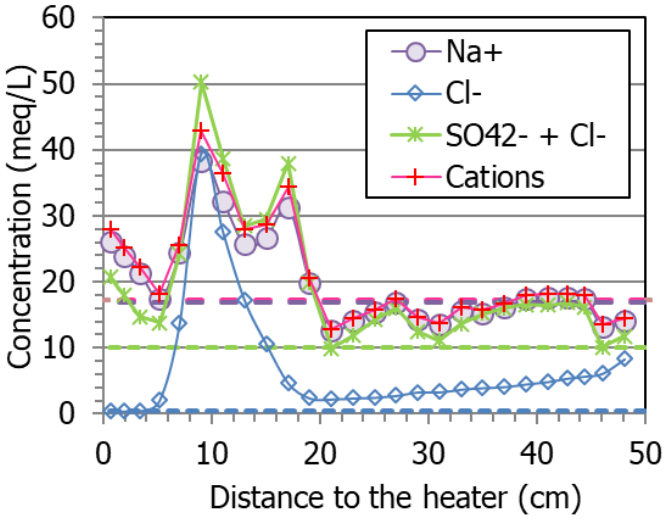

Figure 49 Concentration of main cations (Na^{2+}, Ca^{2+}, Mg^{2+} and K^{+}), sodium, chloride and sulphate measured in aqueous extracts of samples of cell HEE-B (the horizontal lines indicate the concentrations in the untreated pellets)

In contrast with what was observed in other highly saturated Wyoming-type samples coming from TH cells (Gómez-Espina & Villar 2016, Villar et al. 2021b), where the presence of non-filtered colloids was considered responsible for the large contents of Fe^{3+}, Al^{3+} and Si^{4+} measured in the aqueous extracts, in the present column no remarkable contents of Fe^{3+} and Al^{3+} were measured in any sample (although the largest contents were measured in drier samples). The fact that the column was hydrated with a highly saline water would have avoided the formation of colloids. In addition, the amount of aqueous silica was below the initial one in most of the samples and only increased above it in the 10 cm closest to the heater, peaking at 5 cm (Figure 50). This could be explained by the dissolution of quartz and cristobalite during the test because of the high temperature in the area (solubility is increased), and the precipitation of Si as amorphous silica during the cooling stage previous to sampling.

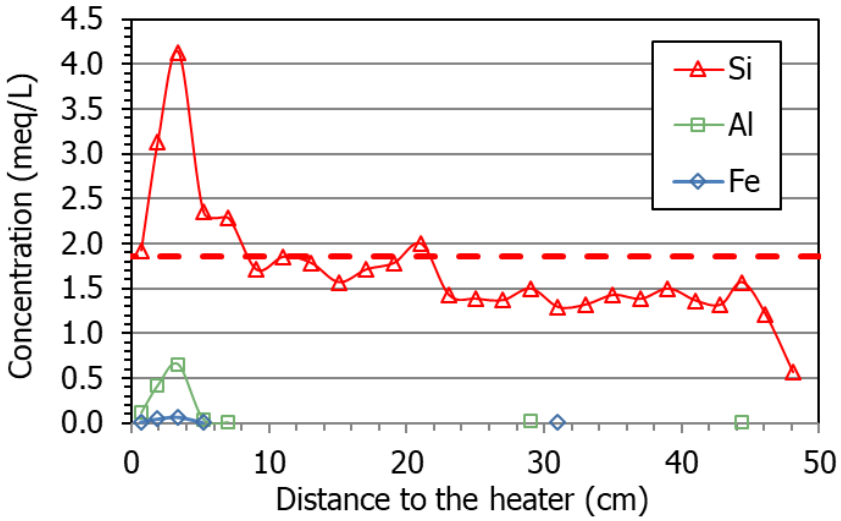

Figure 50 Cations measured in aqueous extracts of samples of cell HEE-B (the horizontal line indicates the Si4+ concentration in the untreated pellets, the other ions were not detected)

5.11 CATION EXCHANGE CAPACITY AND EXCHANGEABLE CATIONS

The results of the exchangeable cations measurements and of the cation exchange capacity (CEC) for all the samples are shown in Table A- 3. These values are plotted as a function of the distance to the heater in Figure 52 and Figure 51. Since the methodology followed for the extraction of exchangeable cations did not involve prior washing of the samples, both exchangeable and soluble cations were actually measured in the extracts prepared. For this reason the values given in the Table and plotted in the Figures correspond in fact to "extractable" cations, in the sense that they may include soluble cations in addition to exchangeable ones. This seems to be particularly the case in the lower half of the column (distances to the heater of less than 20 cm), where the sum of extractable cations was considerably greater than the CEC value (Figure 51), and this would indicate that part of the extractable cations in this area were not exchangeable. In fact, the aqueous extracts of samples from this area also showed a significantly greater salinity than that of the initial bentonite (Table A- 2), as a result of hydration with saline water. Figure 53 plots together the sum of cations extracted with $CsNO_3$ (exchangeable + soluble) and those solubilised with deionised water and discussed in the previous subchapter. The spatial pattern is similar (maxima and minima are displayed approximately at the same locations), but the difference between extractable and soluble cations is highest in the 30 cm closest to the hydration surface and is lower in the 20 cm closest to the heater, which would confirm that part of the extractable cations in this area were actually soluble. Furthermore, the sum of extractable cations even reflected the minimum at 5 cm from the heater observed for the soluble salts.

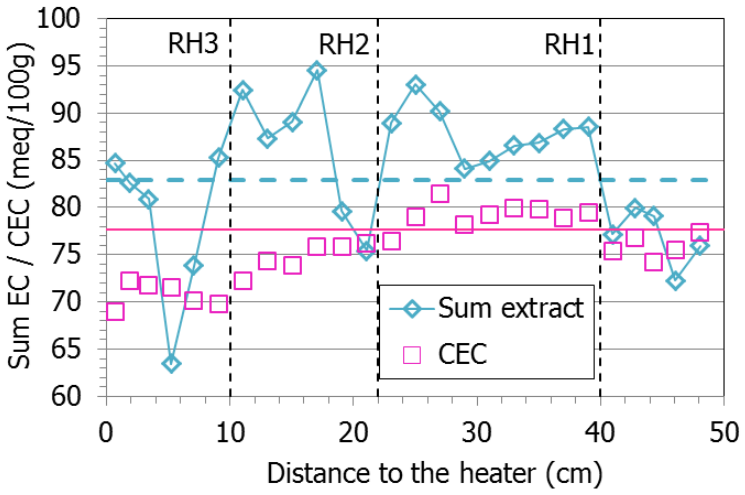

Figure 51 Sum of extractable cations and CEC along the bentonite column of cell HEE-B (the dotted horizontal lines indicate the initial values)

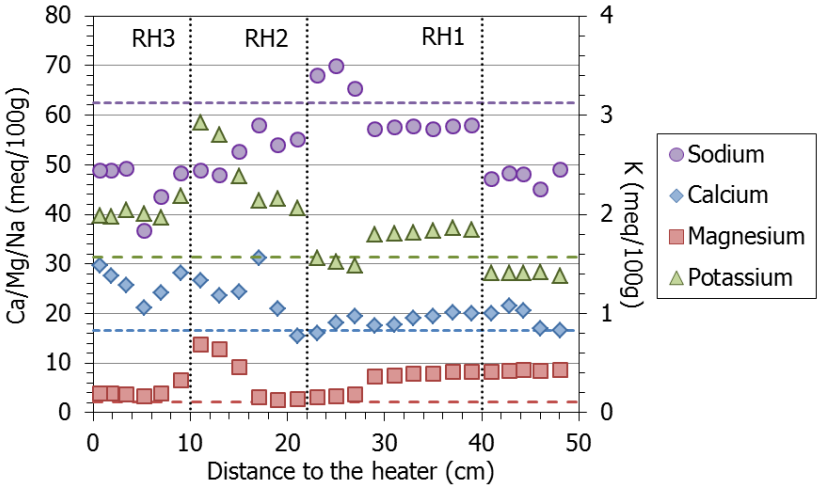

Figure 52 Main extractable cations along the bentonite column of cell HEE-B (the horizontal lines indicate the concentrations in the untreated pellets and the vertical dotted lines correspond to the positions of the sensors)

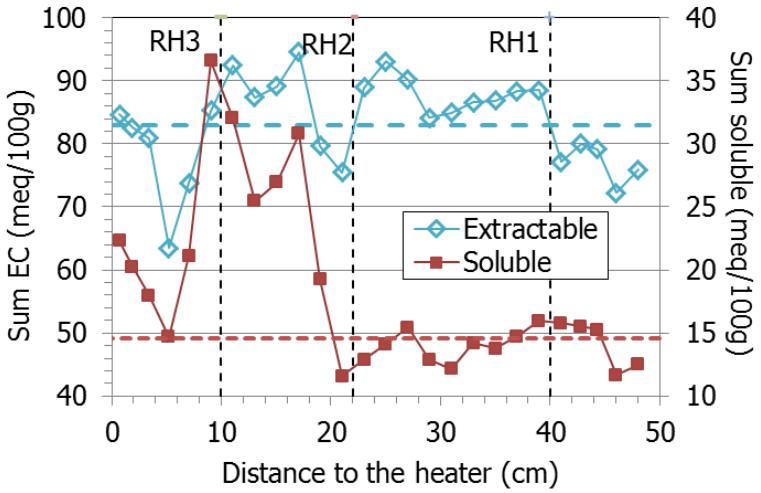

Figure 53 Sum of cations extracted with $CsNO_3$ and of soluble cations (solubilised with aqua) along the bentonite column of cell HEE-B (the dotted horizontal lines indicate the initial values)

The extractable calcium, magnesium and potassium increased globally with respect to the initial values, whereas sodium decreased, particularly towards the column's ends, which is striking because this was the main cation in the hydration water. Nevertheless, it remained the main extractable cation in all the samples. The extractable magnesium content was greater than the initial one in the 20 cm closest to the hydration surface, and then peaked at between 10 and 15 cm from the heater, along with potassium. In contrast, the extractable calcium was approximately constant in the upper part of the column and at approximately 20 cm from the heater started to increase towards it.

5.12 SWELLING PRESSURE AND PERMEABILITY

The swelling pressure and hydraulic conductivity of samples S3 and S11 were determined in the oedometers described in subchapter 4.13. It was not possible to test samples closer to the heater because of their inconsistent state, which did not allow trimming to obtain regular specimens to

fit the rings of the testing equipments. To determine the swelling pressure the samples were saturated under isochoric conditions with deionised water. Subsequently, using the same samples kept in the same apparatus, hydraulic conductivity was measured. A summary of the results obtained concerning swelling pressure is shown in Table 12 and for the subsequent hydraulic conductivity measurements in Table 13. The hydraulic conductivity (k_w) values presented in Table 13 are the average of those obtained under two different hydraulic gradients. The differences between the initial and final dry densities of the samples were caused by the slight vertical deformation allowed by the equipment. Table 12 includes also the axial pressure recorded after the permeability measurement: once the hydraulic gradient was removed the samples were let equilibrate under an injection pressure on top and bottom of 0.1 MPa. This procedure resulted in a decrease of the axial pressure recorded that eventually stabilised. This equilibrium axial pressure was usually higher than the one determined before the permeability test. The axial pressure evolution as the samples became saturated prior to the permeability tests is shown in Figure 54. In log scale it does not seem fully stabilised and maybe a more complete and thorough water saturation was reached during the permeability test, contributing to the final higher axial pressure measured. As for the permeability values obtained, they were below those expected for the untreated powder bentonite (Equation 2).

REFERENCE	DISTANCE TO HEATER (cm)	INITIAL ρ_d (g/cm^3)	INITIAL w (%)	INITIAL S_r (%)	P_s (MPa)	P_s [a] (MPa)	DURATION (days)	T (°C)
S3	44-46	1.41	33.8	96.0	1.7	2.3	76	22
S11	28-30	1.48	30.8	97.0	2.3	2.8	76	22

[a] after permeability measurement

Table 12 Results of the swelling pressure (P_s) tests in two samples from test HEE-B

REFERENCE	DISTANCE TO HEATER (cm)	k_w (m/s)	DURATION (days)	FINAL w (%)	FINAL [a] ρ_d (g/cm^3)	FINAL S_r (%)	T (°C)
S3	44-46	$1.7 \cdot 10^{-13}$	28	37.3	1.40	106	22
S11	28-30	$1.4 \cdot 10^{-13}$	28	35.9	1.46	112	22

[a] just before dismantling, inside the oedometer

Table 13 Results of the hydraulic conductivity (k_w) measurements in samples from test HEE-B

The equilibrium swelling pressure values after the permeability tests are shown in Figure 55 as a function of the final dry density of the samples (shown in Table 13). The empirical exponential correlation between dry density and axial swelling pressure obtained from tests in standard oedometers in which MX-80 samples compacted to different dry densities were saturated with deionised water (Equation 1) is also plotted in the Figure. The values obtained in the treated samples before the permeability tests were slightly below the expected ones (although within the expected range of variation), and after the permeability tests they increased. It is known that the initial water content may also have an influence on the swelling pressure value, the latter decreasing when the initial water content is very high (e.g. Sudjianto et al. 2009, Rao & Ravi 2015), which could be the reason why the treated samples, whose initial degrees of saturation were higher than 96 % (Table 12), had slightly lower swelling pressures than the reference

bentonite. After the permeability tests, the complete saturation of the samples would have made the swelling pressure increase.

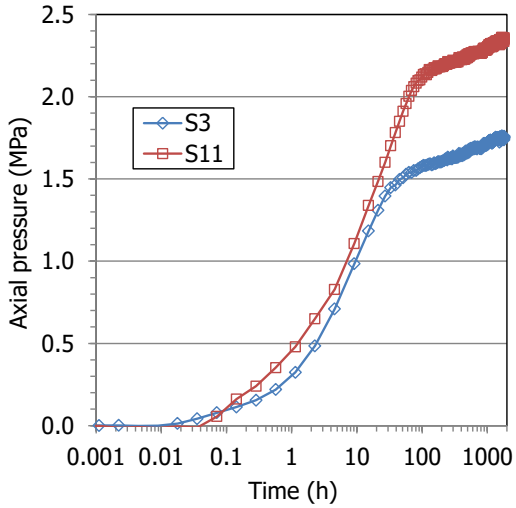

Figure 54 Evolution over time of axial pressure developed by samples from the HEE-B test saturated with deionised water

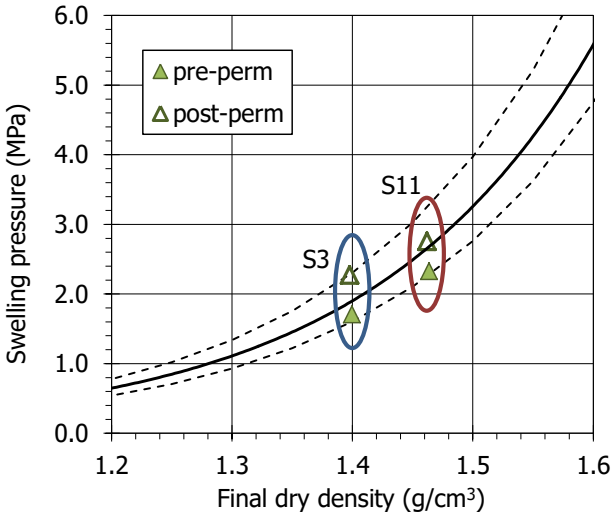

Figure 55 Swelling pressure values measured in samples from the HEE-B test before and after the permeability tests and for MX-80 bentonite samples (Eq. 1)

When evaluating the results concerning hydro-mechanical properties, it should be noted that some boundary conditions (water availability and salinity, stress state, temperature) were different in the oedometer tests than during TH operation. Hence, the values obtained in the oedometers are not those that the bentonite would have during cell operation. Indeed the aim of the tests reported here was to check if the values measured in the material retrieved were similar to those that could be expected for the reference bentonite under similar conditions or if they had been irreversibly affected, which does not seem to have been the case.

6 DISCUSSION

A 50-cm long column of Wyoming-type bentonite pellets was heated at its base at 140 °C while Pearson water was supplied through its upper surface at a very low pressure for nine years. During the test the temperatures remained constant and relatively low in most of the column: only in the 10 cm closest to the heater the temperatures were higher than 60 °C, and higher than 100 °C in the 5 cm closest to the heater. At the end of the experiment the upper half of the column was virtually saturated, but in the lower half the water content decreased sharply towards the heater, where it was close to 0 %. There was also a dry density gradient along the column: it increased from the hydration surface towards the heater. The previous chapter showed the detailed postmortem characterization of the samples taken along the column at the end of the test. A combined interpretation of those results, obtained using different techniques, is given below. This will allow to clarify some observations and support their interpretation.

6.1 MINERALOGY

XRD and FTIR showed that all the samples were composed predominantly of di-octahedral smectite. This was confirmed by the chemical composition obtained by XRF of the <0.5-µm fraction and by numerous localised analyses performed in clay-prevailing areas by SEM-EDX. Smectite showed a remarkable structural stability supported by the constancy of de-hydroxylation temperatures recorded by TGA, in agreement with the constancy of layer charge magnitude and distribution and NMR measurements for all samples. The smectite is actually a montmorillonite, maintaining its composition along the column independently of the temperature during operation, hydration degree reached or salt concentration in specific zones.

Cristobalite and quartz were also present as accessory minerals in this fine fraction, correlated with the presence of small amounts of a micaceous illite-like accessory mineral phase. This illite could not be coupled to mixed-layer formation, as the smectite expanded regularly upon EG solvation without signs of alteration. Then, its detection is not considered an indication of alteration and is attributed to the decrease in the size of the illite-like aggregates contained in the original pellets.

Although pyrite was observed by SEM in several locations along the bentonite column (but not close to the heater), it cannot be related to precipitation under reducing conditions because it is an accessory mineral of the untreated bentonite (e.g. Kumar et al. 2021, Valter & Plotze 2013).

6.2 CATION EXCHANGE COMPLEX

As for the exchangeable cation complex, its population could be assessed using results obtained with different techniques: XRD, TGA, the localised structural formula calculations by SEM-EDX and the direct chemical analysis after displacement with Cs:

- The XRD of the bulk samples showed basal spacings corresponding to predominantly monovalent exchangeable complexes, with values <1.3 nm, tending to decrease towards the

heater. The deconvolution of the random powder XRD patterns showed a contribution of divalent cations in the areas at more than 10 cm from the heater, where the value of the main basal spacing was clearly greater (Figure 29).

- The TGA results, with dehydration temperatures at 54 °C, also pointed to sodium as the main exchangeable cation, particularly nearer the heater. In the middle part of the column the dehydration temperatures were higher, indicating a more divalent cation occupancy in the exchange complex (Caglar et al. 2009).

- Consistently, the structural formulae calculated from SEM-EDX showed a predominance of Na as the exchangeable cation.

These observations could be related to the replacement of cations in the original exchange complex (in which Na predominates, but also Ca and Mg were included) by the sodium coming with the hydrating saline water.

However, it is remarkable that the basal reflections of the smectite in the oriented aggregates pointed to the presence of divalent cations in the interlayer space (d_{001} ~1.4 nm). It is generally acknowledged that during the preparation of suspensions some soluble species are expected to be dissolved and the released cations may replace others in the interlayer according to the differences in adsorption selectivity influenced by the cation distribution itself (Tournassat et al. 2009, 2011). Hence, it is considered that during the preparation of the oriented aggregates some species could be dissolved (gypsum) and the calcium released could substitute for sodium in the interlayer. Even though the random powders showed basal spacings corresponding to predominantly monovalent exchangeable complexes, dissolution during sample preparation could be the reason why the oriented aggregates presented larger spacings corresponding to predominantly divalent smectites (although with a bimodal reflection that evinced the presence of both types of cations). However, this explanation is not obvious for the samples near the hydration source, where gypsum was scarce. In the area at 2 cm from the heater calcite was clearly detected (as well as anhydrite), and this would be a potential calcium source during the preparation of the oriented aggregates of samples from the hottest area.

The exchange of Na by Ca during suspension would also have occurred in the samples prepared for the determination of the exchangeable complex by Cs displacement, and could explain the smaller amount of extractable sodium measured in the drier samples, where calcium sulphates (and carbonates) dissolved during sample preparation were present (as shown by SEM observations). Hence, this distribution pattern would not reflect the actual distribution during the test. Nevertheless, the exchangeable cation complex determined showed the predominance at the end of the test of sodium in the interlayer, in agreement with the population in the initial bentonite and the large sodium concentration of the hydration solution. At 10 cm from the heater, the exchangeable magnesium (and potassium) content peaked, but the increase did not progress towards the heater, so maybe it was more related to the accidental evaporation at this level (see below in section 6.4) than to temperature. The fact that this cell was hydrated with a highly saline water may also have affected the kind and magnitude of interlayer changes.

The CEC decreased slightly towards the heater. This was not reflected in the evolution of the montmorillonite structural formula and its calcium content along the column (Figure 34, left), with the exception of the perturbation at 11 cm, with the increase in calcium and magnesium (S19, Figure 34, right). Hence, the decrease in CEC has no obvious explanation, although this phenomenon has been observed systematically in other bentonite heating experiments (Gómez-Espina & Villar 2016, Kaufhold et al. 2017, Dohrmann & Kaufhold 2017, Villar 2017). In contrast to the generalised reduction of CEC observed in those tests, in the present column the CEC decreased only in the warmer areas. Dehydration and the decrease in surface area as a result of aggregation and formation of dense aggregates have been argued as possible explanations. In turn these processes could lead to a decrease in some surface positions for cation exchange. Heuser et al. (2014) observed that steam treatment on different bentonites reduced CEC, especially in monovalent (Na, K) specimens compared to divalent bentonites. Considering that full rehydration of these samples was achieved during the continuous batch steps for calcium saturation of the montmorillonite (Figure 30), it is possible that CEC could also be recovered, which should be tested in the future. Another explanation for the CEC decrease would be the smectite alteration, but the results of this research point to no significant changes in its crystal-chemistry.

6.3 MOVEMENT OF SOLUBLE SPECIES

Other similar heating-hydration tests showed that hydration caused the dissolution of some species and that the solubilised ions were transported towards the heater and precipitated farther away along the bentonite column as the test was longer (Fernández & Villar 2010; Gómez-Espina & Villar 2016, Kober et al. 2021). Those tests also showed that, for a given duration, the chloride concentration in the aqueous extracts peaked closer to the heater than the sulphate one, given their different size and the implication of sulphate in other dissolution/precipitation processes. Indeed sulphate peaked in this test at ~18 cm from the heater, where the temperature during the test was 40 °C, whereas the chloride maximum was at 9 cm from it (T~60 °C), approximately at the location of sensor RH3 (Figure 48). Interestingly, the calcium and sodium concentrations had maxima at these two distances, so they must be related both to sulphate and chloride. In fact, gypsum solubility increases in the presence of dissolved NaCl and has its maximum at approximately 40 °C (0.05 mol/kg at 1-5 M NaCl, Marshall & Slusher 1966), which was the temperature at ~18 cm from the heater, where maxima of the two anions were recorded. The high salinity in these areas likely triggered the corrosion of the sensors, particularly the bottom one (Villar et al. 2022).

The pattern of gypsum distribution as observed by XRD would indicate that sulphate leaching took place. In the more hydrated bentonite, gypsum could not be detected, which could indicate its dissolution and transport. In fact, gypsum appeared in the region between 10 and 30 cm from the heater, where its solubility would tend to decrease because of the progressively higher temperature (Table 2): between 40 °C, close to its maximum solubility, and 60 °C, close to an anhydrite-predominant environment. Hence, it would precipitate or be replaced by the less soluble anhydrite (Serafeimidis & Anagnostou 2015, Marshall & Slussher 1966). In fact, SEM observations allowed to spot occasional calcium sulphates close to the heater (presumably

anhydrite traces that were not possible to detect by XRD), as also the FTIR results showed (Figure 36). In the 10 cm closest to the heater (temperatures higher than 60 °C) gypsum was again absent. However, the sulphate concentration in the aqueous extracts was greater than the initial one in this area, tending to increase towards the heater. Olsson & Karnland (2011) reported in the large-scale LOT project a redistribution of Ca-sulphate phases. Their results indicated that gypsum dissolution occurred in the colder part of the bentonite barrier at the host rock contact and anhydrite precipitated in the bentonite close to the heater within six years. These observations were reproduced by modelling (Itälä & Olin 2011). In the LOT A3 parcel, with MX-80 bentonite submitted for 10 years to heater temperatures of 120-150 °C, significant anhydrite accumulation at less than 2 cm from the heater was found (reported by Villar et al. 2021). Anhydrite accumulations in the bentonite close to the heater were reported by Dueck et al. (2011) for the in situ large-scale Canister Retrieval Test and by Kaufhold et al. (2017) in the ABM-2 in situ test, where the peak temperatures at the heater surface were 140 °C.

The increase of bicarbonate in the aqueous extracts near the heater zone may relate to the observed presence of calcite and its dissolution during the preparation of the aqueous extracts. The observation of carbon-rich fill in the cavities could indicate the evolution of a gas phase either with carbon coming from the steel heater or CO_2 appearing as a co-product of the evaporation of the salty solutions produced at ~10 cm from the heater. CO_2 degassing was invoked to explain calcite precipitation in similar TH tests (Fernández & Villar 2010). Calcite was not detected close to the hydration surface and the bicarbonate content was small in this area. In contrast, the analysis of the water left in the hydration vessel after the test (Table 1) showed a significant decrease in calcium and an increase in bicarbonate content relative to the initial value. Both observations could be related to the dissolution of calcite in the more hydrated area, the diffusion of bicarbonate towards the hydration source and the incorporation of the calcium released to the exchangeable complex substituting for sodium.

The high temperature in the 5 cm closest to the heater could have also caused the dissolution of quartz and cristobalite inferred from the results in Figure 50 (Telster et al. 1994). The relatively high extractable silica in this zone could be related to the presence of amorphous silica, more soluble than quartz (Gunnarson & Arnórsson 2000) and not easily detected by XRD due to its small amount. Svensson & Hansen (2013) and Kaufhold et al. (2013) observed cristobalite dissolution in large-scale tests performed with MX-80 bentonite at locations where the temperature was between 130 and 150 °C. It must be pointed out that, although it seems evident that vapour leaked through the bottom sensor inlet, this did not happen from the beginning of the test, and during an undetermined period of time (which may have been long) liquid water was probably able to reach areas closer to the heater than the level of the sensor location. In fact, the distribution pattern of soluble ions (Figure 47 and Figure 48, and also that for extractable cations in Figure 51) shows minimum values at 5 cm from the heater followed by a progressive increase towards it, with overall values in the area higher than the initial ones. This would indicate that water loaded with soluble species was able to reach the area at less than 10 cm from the heater and when this water supply stopped as a consequence of the vapour leak, the accumulated salts redistributed by convection-concentration processes.

6.4 EFFECTS OF ACCIDENTAL EVAPORATION

Halite was observed at ~9 cm from the heater (sample S20) by XRD and its presence was confirmed by SEM observations. Instead of the usual small cubic or dendritic crystallizations, halite presented undifferentiated morphologies, like rounded glassy efflorescences in which also Ca was detected by EDX (Figure 43). Sub-millimetric rounded morphologies were prepared by evaporation at 58 °C in industrial processes looking for crystal growth inhibition (Mukhopadhyay et al. 2010), and subhedral rounded morphologies were reported for naturally-induced weathering of polyelectrolyte salt brines (Rodriguez-Navarro & Dohene 1999). This agrees with the large sodium (and calcium, Figure 47) and chloride contents measured in the aqueous extracts of this region. The hypothesis is that $CaCl_2$ deliquescent salt could take part in the crystallisation inhibition during evaporation, although this aspect requires further elucidation. Sample S20 was located at the level of sensor RH3, which was extracted completely corroded at the end of the test (Villar et al. 2022). The inlet of this sensor across the Teflon cell wall was likely a leak path from an undetermined moment during the operation, allowing vapour to scape and creating an area of evaporation around it. Around the sensor inlet the specific surface area of the bentonite was lowest (Figure 17), indicating aggregation of particles likely caused by shrinkage when water evaporated from bentonite whose water content was higher prior to the start of the leak. From this point towards the heater the bentonite was disaggregated and had a water content smaller than the initial one (Figure 7). Also, from this point towards the heater (temperatures >60 °C) the rehydration of the bentonite at room conditions was more difficult (Figure 24). In the nearby sample S19, the amounts of exchangeable magnesium and potassium reached maxima (Figure 52). Hence it seems that the accidental evaporation through the sensor inlet gave place to particular conditions that significantly affected the processes in this area.

The samples that had been submitted to temperatures greater than 60 °C (those at less than 9 cm from the heater) were not able to completely develop the 1-layer hydrate after 48 h of stabilisation at RH 55 % and they even showed the reflection corresponding to the completely dehydrated interlayer (Figure 27). These rather small d_{001} values for monovalent hydrates in smectite were predicted for RH conditions <5 % by the modelling of hydrates in Na-smectite by Dazas et al. (2015) and Ferrage et al. (2010). However, the d_{001} values of oriented aggregates were similar for all the samples, irrespective of their location along the column, because they were performed using aqueous-suspended samples, completely hydrated before being dried at room conditions once on the glass tile. The stabilisation of samples taken at different distances from the heater under relative humidity of ~41 % first and 97 % afterwards showed that, although the samples that had been submitted to the highest temperatures reached lower equilibrium water contents than the other samples under the lowest RH, they were able to take as much water as the other ones when stabilised under higher RH, irrespective of the reaction time. This would indicate that the rehydration capacity of the bentonite was only reduced for low relative humidity, but completely recovered when the relative humidity was high or hydration with liquid water was involved. Valter & Plötze (2013) observed that samples stabilised under RH=75 % after having been treated at temperatures of up to 105 °C had the same water adsorption capacity as untreated samples, and although for higher treatment temperatures the water adsorption capacity decreased, it recovered after remoulding.

6.5 MICROSTRUCTURE AND HYDRO-MECHANICAL PROPERTIES

The pore size distribution obtained by MIP showed that initially the bentonite granulate had 69 % of pores larger than 200 nm, more than half of which were actually larger than 550 µm, and a family of pores with a mode size ~9 nm. As a result of hydration the macroporosity of the GBM from the upper half of the column (samples located at more than 24 cm from the heater and with water contents greater than ~29 %) shifted to smaller pore sizes with respect to the original GBM, i.e. the largest pores were lost and the void ratio corresponding to macropores decreased. In contrast, the void ratio corresponding to pores smaller than 200 nm increased with respect to the reference material, as well as their mode size, and both parameters were similar for all the samples in this area. From the middle part of the column downwards (samples below S15), there was a change in the pore size distribution pattern: the void ratio corresponding to macropores started to increase towards the heater, whereas the void ratio for smaller pores became similar to the initial one. Thus, close to the heater the pore size distribution was similar to that of the untreated pellets. Hence, as a result of the thermo-hydraulic treatment, the ratio between the void ratio corresponding to pores smaller and larger than 200 nm (e_m/e_M) increased overall in all the samples, but particularly in the upper half of the column. This was observed in other in situ and laboratory hydration tests (Villar 2017, Villar et al. 2021a, b). In the 10 cm closest to the heater, where the sample was very dry and disaggregated, the e_m/e_M ratio was below 1 (more volume of pores higher than 200 nm than smaller). This seems logical since their water content was below the initial one, so no crystalline swelling developed and e_m remained small. The direct relation between crystalline swelling (basal spacing determined in samples without previous treatment, subchapter 4.2) and void ratio corresponding to pores smaller than 200 nm is shown in Figure 56. This Figure also highlights that the abrupt increase in basal spacing corresponding to the change from a predominant 1-layer hydrate (~1.2 nm) to a 2-layer one (~1.5 nm) coincided with a jump in void ratio.

The basal spacing measurements also showed that there was a direct relation between basal spacing and water content (Figure 19). Figure 57 shows again these values plotted along with the basal reflection measurements performed in samples of MX-80 bentonite compacted with different water contents and dry densities (Villar et al. 2012b, Villar 2013 and unpublished results). For water contents below 30 % the relationship between water content and basal spacing in the HEE-B samples follows the overall trend found in other MX-80 samples. Namely, the values agreed well with those of samples from an infiltration test performed under ambient temperature with the same MX-80 pellets as in test HEE-B and using Pearson water as hydration fluid (test MGR18, Villar 2013). In this test the basal spacings corresponding to the fully saturated bentonite pellets (w=27.2 %) after 446 days of hydration were between 1.49 and 1.56 nm. However, for higher water contents, the basal spacings measured in samples from the HEE-B cell are lower than those measured in other compacted samples of similar water contents. The fact that the samples from the HEE-B cell were saturated with a highly saline water could have affected their hydration behaviour with respect to the other samples, which were all saturated with deionised water. Also, the samples from the HEE-B cell were X-rayed three weeks after

dismantling, which may have reduced the contribution of the 3-layer hydrate in favour of the 2-layer one, predominant in the samples from the HEE-B cell.

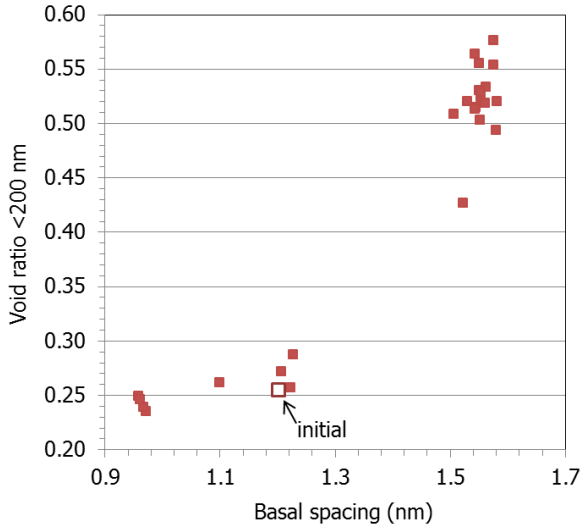

Figure 56 Relation between void ratio corresponding to pores <200 nm (as determined by MIP) and the basal spacing determined in untreated samples from test HEE-B

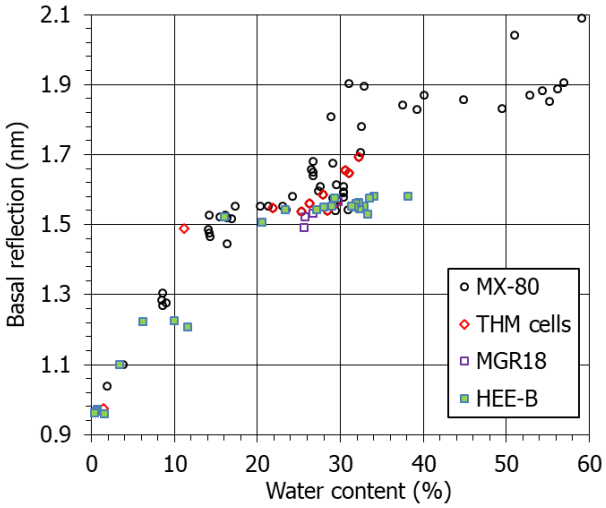

Figure 57 Main diffraction reflection of the basal reflection of subsamples of lab tests performed with MX-80 bentonite (values from Villar et al. 2012b, Villar 2013 and other unpublished results) and of the HEE-B cell

Another microstructural effect observed was the decrease in specific surface area for those samples at less than 15 cm from the heater (T>42 °C), which were also those with dry density higher than the initial one. However, the decreases observed were not as acute as those reported by Valter & Plötze (2013), who measured values smaller than the initial one even for temperatures of only 50 °C, but particularly reduced for temperatures above 100 °C, with values as low as 12 m^2/g. These authors considered that the thermally-induced decrease of a_s was related to bentonite aggregation. However, such low values of a_s were only measured in the column samples located at 10 cm from the heater (minimum value was 17 m^2/g, around the sensor RH3 leaking inlet), where the temperature was lower than 60 °C. For this reason it is considered that the decrease in a_s was more related to sustained evaporation than to

temperature. Evaporation through the sensor inlet would cause shrinkage, densification and aggregation of particles in an area where the water content had been previously higher. Nevertheless, in the 5 cm closest to the heater (where presumably the water content was never higher than the initial one), a_s decreased towards the heater, reaching at the contact a value of 25 m^2/g. Conversely, the specific surface area of all the samples at more than 15 cm from the heater increased with respect to the initial value.

The swelling pressure and hydraulic conductivity were determined only in two samples (S3 and S11) corresponding to the more saturated part of the column. It took very long to reach a quasi-equilibrium swelling pressure value, and this corresponded well with that expected for untreated MX-80 bentonite of the same dry density according to determinations previously performed at CIEMAT in compacted samples. As for the permeability values obtained, they were below those expected for the untreated compacted bentonite powder. Previous studies with samples that were saturated for very long periods of time (e.g. Villar et al. 2018 for FEBEX bentonite, Villar et al. 2021b for MX-80 bentonite) showed a decrease of hydraulic conductivity with respect to the values obtained in untreated samples just saturated for a few weeks before the determination (such as those used to obtain the empirical correlation of Equation 2, saturated for less than 50 days). This decrease was explained by the "maturation" of the microstructure during the thermo-hydraulic treatment, consisting for the samples of the HEE-B test in the suppression of the macropores and the decrease of the overall mean pore size, which would give place to the decrease of the intrinsic permeability.

Although no worsening of the HM properties of the bentonite was observed in the two samples analysed, it must be taken into account that none of them was subjected to high temperature during the test, because they were taken at more than 27 cm from the heater (T<34 °C). Consequently, these results do not provide experimental evidence about the effect of sustained high temperature on the HM properties of the bentonite, but on the effect of saturation with saline water under representative confinement conditions for a long period of time.

7 SUMMARY AND CONCLUSIONS

With the aim of simulating in the laboratory the conditions in one of the barrier materials used in the HE-E *in situ* test, a 50-cm long column of a granulate of MX-80 bentonite pellets was heated at its base to 140 °C while Pearson water was supplied through its upper surface at a very low pressure. The test, carried out in a Teflon cell equipped with relative humidity and temperature sensors, consisted of a heating phase that lasted from November 2011 to June 2012 (with an initial period in which the heater was set at 100 °C) and a heating+hydration phase that went on for more than nine years (final dismantling in November 2021). The initial dry density of the bentonite inside the column was 1.53-1.54 g/cm^3 and its water content 5.8-6.4 %.

The temperatures in the bentonite remained approximately constant during the whole duration of the experiment, with a steep thermal gradient close to the heater: the temperature was higher than 100 °C only in the 5 cm closest to the heater. Upon dismantling it was seen that the upper half of the column, where no pellets could be discerned, had water contents around 30 % and uniform degrees of saturation between 92 and 99 %. In contrast, the water content and degree of saturation decreased sharply towards the heater in the bottom half of the column, with values close to 0 % in the 5 cm closest to the heater. In the 16 cm closest to the heater the bentonite was lighter in colour and was loose.

At the end of the test all the samples continued to consist predominantly of a dioctahedral smectite, with no significant differences from the original with respect to the distribution of structural cations and layer charge. No evidence of mixed-layer formation was detected. Sodium continued to predominate in the exchangeable cation complex (according to the measurement of the basal spacing, thermogravimetry, and Cs displacement results), probably as a consequence of the hydration with a predominantly sodic solution. However, some contribution of divalent cations toward the hydration surface could be detected.

Despite the lack of montmorillonite alteration at the structural level, the drier samples, those that were submitted to temperatures >60 °C, remarkably had a significant resistance to rehydration under room relative humidity conditions. However, this was not an irreversible process, as the samples hydrated normally when the relative humidity was high (97 %) and expanded as expected when suspended in water.

Although hydration took place with a highly saline water – which seems to have inhibited the formation of colloids – the overall increase in water content allowed the dissolution of some species and the solubilised ions were transported toward the heater and precipitated at two distinct areas: sulphate, sodium, and calcium peaked at ~18 cm from the heater whereas chloride moved closer to the heater (accompanied by sodium and calcium), concentrating at 9 cm from it, coinciding with a vapour leak area. This leak started at some undetermined moment during the test through a sensor inlet. This experimental artefact seems to have conditioned the processes around it, such as the movement of solubilised ions. The liquid-water availability was probably affected also in the areas of temperatures higher than 60 °C, which would limit the reactivity there. Nevertheless, evidence of precipitation of calcite and calcium sulphates and

dissolution of cristobalite and quartz were observed in the areas where the temperature was higher than 100 °C.

Around this sensor inlet the specific surface area of the bentonite was lowest, indicating aggregation of particles likely caused by shrinkage when water evaporated from bentonite whose water content was higher prior to the start of the leak. From this point towards the heater the bentonite was disaggregated, with specific surface areas smaller than the initial one.

The pore size distribution was also affected by operation. As a result of hydration, in the upper half of the column (samples with water contents greater than ~29 %) the largest pores were lost and the void ratio corresponding to macropores decreased. In contrast, the void ratio corresponding to pores smaller than 200 nm increased with respect to the reference material, as well as their mode size. This reorganisation of the pore size distribution in hydrated areas was likely responsible of the observed decrease in hydraulic conductivity with respect to the untreated bentonite. From the middle part of the column downwards, the void ratio corresponding to macropores started to increase towards the heater, whereas the void ratio for smaller pores became similar to the initial one. Thus, close to the heater the pore size distribution was similar to that of the untreated pellets, reflecting that no crystalline swelling had taken place.

Overall, the processes described are similar to those observed in other large-scale tests simulating the conditions of a bentonite barrier with temperatures higher than 100 °C. The use of pellets instead of compacted blocks does not seem to have been an additional source of uncertainty.

8 REFERENCES

[1] Ammann, L., Bergaya, F., Lagaly, G. 2005. Determination of the cation exchange capacity of clays with copper complexes revisited. Clay Minerals 40: 441-453.

[2] Brindley, G.W. 1980. Order-disorder in clay mineral structures of clay minerals and their X-ray identification. Mineralogical Society, London, 496 pp.

[3] Caglar B., Afsin, B., Tabak, A., Eren, E. 2009. Characterization of the cation-exchanged bentonites by XRPD, ATR, DTA/TG analyses and BET measurement. Chemical Engineering Journal 149: 242–248.

[4] Chukanov, N.V., Chervonnyi, A.D. 2016. Infrared Spectroscopy of Minerals and Related Compounds. Springer Mineralogy: 1109 pp.

[5] Cuevas, J.F., Fernández, R., Ortega, A., Ruiz, A.I. 2014. Comparison of alternative bentonites for potential use as buffer and sealing materials in the Swiss concept for radioactive waste disposal. Part 2: Results. Nagra Arbeitsbericht NAB 14-65.

[6] Dazas, B., Lanson, B., Delville, A., Robert, J.L., Komarneni, S., Michot, L.J., Ferrage, E. 2015. Influence of Tetrahedral Layer Charge on the Organization of Inter Layer Water and Ions in Synthetic Na-Saturated Smectites. The Journal of Physical Chemistry C 119(8): 4158-4172.

[7] Dohrmann, R., Kaufhold, S. 2017. Characterization of the second package of the Alternative Buffer Material experiment (ABM) – II Exchangeable cation population rearrangement. Clays and Clay Minerals 65: 104–121. https://doi.org/10.1346/CCMN.2017.064052

[8] Dohrmann, R., Rüping, K.B., Kleber, M., Ufer, K., Jahn, R. 2009. Variation of preferred orientation in oriented clay mounts as a result of sample preparation and composition. Clays and Clay Minerals 57(6): 686–694. https://doi.org/10.1346/CCMN.2009.0570602

[9] MacEwan, C., Wilson, M.J. 1984. Interlayer and intercalation complexes of clay minerals. In G.W. Brindley & G. Brown (eds), Crystal structures of clay minerals and their X-ray Identification (pp. 197-248). Monograph 5, Mineralogical Society.

[10] Dueck, A., Johannesson, L.E., Kristensson, O., Olsson, S., Sjöland, A. 2011. Hydro-Mechanical and Chemical-Mineralogical Analyses of the Bentonite Buffer from A Full-Scale Field Experiment Simulating a High-Level Waste Repository. Clays and Clay Minerals 59: 595–607. https://doi.org/10.1346/CCMN.2011.0590605

[11] Estep P., Kovach J., Karr C. 1968 Quantitative infrared multicomponent analysis of minerals occurring in coal. Analytical Chemistry 40(2): 358-363.

[12] Fernández, A.M., Villar, M.V. 2010. Geochemical behaviour of a bentonite barrier in the laboratory after up to 8 years of heating and hydration. Applied Geochemistry 25: 809-824. https://doi.org/10.1016/j.apgeochem.2010.03.001

[13] Ferrage, E., Lanson, B., Michot, L.J., Robert, J.L. 2010. Hydration Properties and Interlayer Organization of Water and Ions in Synthetic Na-Smectite with Tetrahedral Layer Charge. Part 1. Results from X-ray Diffraction Profile Modeling. The Journal of Physical Chemistry C 114(10): 4515−4526.

[14] Fesharaki, O., García-Romero, E., Cuevas-González J., López-Martínez, N. 2007. Clay mineral genesis and chemical evolution in the Miocene sediments of Somosaguas, Madrid Basin, Spain. Clay Minerals 42: 187–201.

[15] García-Romero, E., Lorenzo, A., García-Vicente, A., Morales, J., García-Rivas, J., & Suarez, M. 2021. On the structural formula of smectites: a review and new data on the influence of exchangeable cations. Journal of Applied Crystallography 54: 251-262. https://doi.org/10.1107/S1600576720016040

[16] Gaus, I., Wieczorek, K., Mayor J.C., Trick T., García-Siñeriz, J.L., Schuster, K., Garitte, B., Kuhlman, U. 2011. EBS behaviour immediately after repository closure in a clay host rock: the HE-E experiment (Mont Terri URL). Proceedings of the 14th Int. Conference on Environmental Remediation and Radioactive Waste Management ICEM'11. September 25-29, 2011, Reims, France. P-59288. ASME, 7 pp.

[17] Gaus I., Garitte B., Senger R., Gens A., Vasconcelos R., Garcia-Sineriz J.-L., Trick T., Wieczorek K., Czaikowski O., Schuster K., Mayor J.C., Velasco M., Kuhlmann U., Villar M.V. 2014. The HE-E Experiment: Lay-out, Interpretation and THM Modelling. Nagra Arbeitsbericht NAB 14-53. Wettingen, 140 pp.

[18] Gómez-Espina, R., Villar, M.V. 2008. Presión de hinchamiento y permeabilidad en edómetro de alta presión. Procedimiento Técnico CIEMAT PT-MA-04-01. Madrid, 19 pp.

[19] Gómez-Espina, R., Villar, M.V. 2016. Time evolution of MX-80 bentonite geochemistry under thermo-hydraulic gradients. Clay Minerals 51(2): 145-160. DOI: 10.1180/claymin.2016.051.2.03

[20] Gunnarsson, I., Arnórsson, S. 2000. Amorphous silica solubility and the thermodynamic properties of H4SiO°4 in the range of 0° to 350 °C at Psat. Geochimica et Cosmochimica Acta 64(13): 2295-2307. https://doi.org/10.1016/S0016-7037(99)00426-3

[21] Heuser, M., Weber, C., Stanjek, H., Chen, H., Jordan, G., Schmahl, W.W., Natzeck, C. 2014. The Interaction Between Bentonite and Water Vapor. I: Examination of Physical and Chemical Properties. Clays and Clay Minerals 62: 188–202. https://doi.org/10.1346/CCMN.2014.0620303

[22] Idiart, A., Coene, E., Villar, M.V., Cuevas, J., Melón, A.M., Ortega, A., Ruiz, A.I., Maanoja S. 2022. Experimental study of thermo-hydro-geochemical evolution of compacted bentonite: geochemical characterization and numerical modelling. 8th International Conference on clays in natural and engineered barriers for radioactive waste confinement. Poster CLAY00102. Nancy, July 2022.

[23] Imbert, C., Villar, M.V. 2006. Hydro-mechanical response of a bentonite pellets/powder mixture upon infiltration. Applied Clay Science 32: 197-209.

[24] Itälä, A., Olin, M. 2011. Chemical evolution of bentonite buffer in a final repository of spent nuclear fuel during the thermal phase. Nuclear Technology 174: 342-352.

[25] Johnson, L.H., Niemeyer, M., Klubertanz, G., Siegel, P., Gribi, P. (2002): Calculations of the temperature evolution of a repository for spent fuel, vitrified high-level waste and intermediate level waste in Opalinus Clay. Nagra Technical Report NTB 01-04. Nagra, Wettingen, Switzerland.

[26] Kaufhold, S., Dohrmann, R., Götze, N., Svensson, D. 2017. Characterization of the second parcel of the alternative buffer material (ABM) experiment–I mineralogical reactions. Clays and Clay Minerals 65(1): 27-41.

[27] Kaufhold, S., Dohrmann, R., Sandén, T., Sellin, P., Svensson, D. (2013). Mineralogical investigations of the first package of the Alternative Buffer Material test – I. Alteration of bentonites. Clay Minerals 48: 199–213. https://doi.org/10.1180/claymin.2013.048.2.04

[28] Kober, F., García-Siñeriz, J.L., Villar, M.V., Lanyon, G.W., Cloet, V., Mäder, U., Wersin, P., Leupin, O., Sellin, P., Gens, A., Schneeberger R. 2021. FEBEX-DP Synthesis Summary of the Full-Scale Engineered Barriers Experiment – Dismantling Project. NAGRA Technical Report 17-01. Wettingen, 204 pp.

[29] Mantovani, M., Escudero, A., Becerro, A.I. 2009. Application of 29Si and 27Al MAS NMR spectroscopy to the study of the reaction mechanism of kaolinite to illite/muscovite. Clays and Clay Minerals 57: 302–310.

[30] Marshall, W.L. Slusher, R. 1966. Thermodynamics of calcium sulfate dihydrate in aqueous sodium chloride solutions, 0-110 °C. Journal of Physical Chemistry 70(12): 4015–4027.

[31] Morris, H.D., Bank, S., Ellis, P.D. 1990. Aluminum-27 NMR spectroscopy of iron-bearing montmorillonite clays. The Journal of Physical Chemistry 94(7): 3121-3129.

[32] Mukhopadhyay, I., Mohandas, V.P., Desale, G.R., Chaudhary, A., Ghosh, P.K. 2010. Crystallization of spherical common salt in the submillimeter size range without habit modifier. Industrial & Engineering Chemistry Research 49(23): 12197-12203.

[33] NAGRA 2019. Implementation of the Full-scale Emplacement Experiment at Mont Terri: Design, Construction and Preliminary Results. NAGRA Technical Report NTB 15-02. Wettingen, 147 pp.

[34] Nieto, F., Mellini, M., Abad, I. 2010. The role of H_3O^+ in the crystal structure of illite. Clays and Clay Minerals 58(2): 238–246.

[35] Olsson, S. Karnland, O. 2011. Mineralogical and chemical characteristics of the bentonite in the A2 test parcel of the LOT field experiments at Äspö HRL, Sweden. Physics and Chemistry of the Earth 36(17-18): 1545-1553.

[36] Pearson F. 2002. PC Experiment: Recipe for Artificial Pore Water. Switzerland. Mont Terri Project Technical Note 2002-17. St. Ursanne, Switzerland, 10 pp.

[37] Plötze M., Weber H.P. 2007. ESDRED: Emplacement tests with granular bentonite MX-80: Laboratory results from ETH Zürich. Nagra Arbeitsbericht NAB 07-24. Nagra, Wettingen.

[38] Poppe, L.J., Eliason, A.E. 2009. A basic program to calculate gravitational and centrifugal settling parameters. Geological Society of America 41(3): 21.

[39] Rodriguez-Navarro, C., Doehne, E. 1999. Salt weathering: influence of evaporation rate, supersaturation and crystallization pattern. Earth Surface Processes and Landforms: The Journal of the British Geomorphological Research Group 24(3): 191-209.

[40] Sánchez, L., Cuevas, J., Ramírez, S., Ruiz-De-León, D., Fernández, R., Vigil-De-La-Villa, R., Leguey, S. 2006. Reaction kinetics of FEBEX bentonite in hyper-alkaline conditions resembling the cement–bentonite interface. Applied Clay Science 33(2): 125–141.

[41] Santosh Kumar Verma, Manas Kanti Deb. 2007. Nondestructive and rapid determination of nitrate in soil, dry deposits and aerosol samples using KBr-matrix with diffuse reflectance Fourier transform infrared spectroscopy (DRIFTS). Analytica Chimica Acta 582(2): 382-389

[42] Serafeimidis, K., Anagnostou, G. 2015. The solubilities and thermodynamic equilibrium of anhydrite and gypsum. Rock Mechanics and Rock Engineering 48: 15-31.

[43] Smith, J.V., Blackwell, C.S. 1983. Nuclear magnetic resonance of silica polymorphs. Nature 303: 223-225.

[44] Sawhney, B.L. 1970. Potassium and cesium ion selectivity in relation to clay mineral structure. Clays and Clay Minerals 18(1): 47-52.

[45] Teodori, S.P., Gaus, I. (Eds.) 2011. Long Term Performance of Engineered Barrier Systems (PEBS). Mont Terri HE-E experiment: as built report. Nagra Arbeitsbericht NAB 11-25. Nagra, Wettingen, 125 pp.

[46] Tournassat, C., Bizi, M., Braibant, G., Crouzet, C. 2011. Influence of montmorillonite tactoid size on Na–Ca cation exchange reactions. Journal of Colloid and Interface Science 364(2): 443-454.

[47] Tournassat, C., Gailhanou, H., Crouzet, C., Braibant, G., Gautier, A., Gaucher, E.C. 2009. Cation Exchange Selectivity Coefficient Values on Smectite and Mixed-Layer Illite/Smectite Minerals. Soil Science Society America Journal 73: 928-942.

[48] Valter, M., Plötze, M. 2013. Characteristics of variably saturated granular bentonite after long-term storage at near-field relevant temperatures. Clay Minerals 48(2). https://doi.org/343-361. 10.1180/claymin.2013.048.2.14

[49] Verma, S.K., Deb, M.K. 2007. Nondestructive and rapid determination of nitrate in soil, dry deposits and aerosol samples using KBr-matrix with diffuse reflectance Fourier transform infrared spectroscopy (DRIFTS). Analytica Chimica Acta 582: 382-389. https://doi.org/10.1016/j.aca.2006.09.020

[50] Villar, M.V. 2005. MX-80 bentonite. Thermo-hydro-mechanical characterisation performed at CIEMAT in the context of the Prototype Project. Informes Técnicos CIEMAT 1053. CIEMAT, Madrid, 39 pp.

[51] Villar, M.V. 2013. Long-term THM tests reports: Isothermal infiltration tests with materials from the HE-E. PEBS Deliverable 2.2-7.2. CIEMAT Technical Report CIEMAT/DMA/2G210/07/2013. Madrid, 32 pp.

[52] Villar, M.V. 2017. FEBEX-DP Post-mortem THM/THG Analysis Report. Nagra work report Arbeitsbericht NAB 16-17, 147 pp., Wettingen, Switzerland, https://www.grimsel.com/gts-projects/febex-dp/febex-dp-literature-publications

[53] Villar, M.V., Lloret, A. 2001. Variation of the intrinsic permeability of expansive clay upon saturation. In: Adachi, K., Fukue, M. (Eds.) Clay Science for Engineering. Balkema, Rotterdam, pp. 259–266.

[54] Villar, M.V.; Martín, P.L., Barcala, J.M. 2005. Infiltration tests at isothermal conditions and under thermal gradient. Informe Técnico CIEMAT/DMA/M2140/1/05. Madrid, 24 pp. Abril 2005.

[55] Villar, M.V.; Sánchez, M., Gens, A. 2008. Behaviour of a bentonite barrier in the laboratory: experimental results up to 8 years and numerical simulation. Physics and Chemistry of the Earth 33: S476-S485.

[56] Villar, M.V.; Martín, P.L.; Gómez-Espina, R.; Romero, F.J., Barcala, J.M. 2012a. THM cells for the HE-E test: setup and first results. PEBS Deliverable 2.2-7.1. Technical Report CIEMAT/DMA/2G210/03/2012. Madrid, 34 pp.

[57] Villar, M.V., Gómez-Espina, R., Gutiérrez-Nebot, L. 2012b. Basal spacings of compacted bentonite. Applied Clay Science 65-66: 95-105.

[58] Villar, M.V.; Martín, P.L., Romero, F.J. 2014. Long-term THM tests reports: THM cells for the HE-E test: update of results until February 2014. PEBS Deliverable 2.2-7.3. Technical Report CIEMAT/DMA/2G210/03/2014. Madrid, 19 pp.

[59] Villar, M.V., Martín, P.L., Romero, F.J., Gómez-Espina, R., Iglesias, R.J., Gutiérrez-Rodrigo, V. 2015. HE-E Experiment: Laboratory test in a THM cell with the Sand/Bentonite mixture. Mont Terri Project TN 2015-43. Madrid, 28 pp.

[60] Villar, M.V., Martín, P.L., Romero, F.J., Iglesias, R.J., Gutiérrez-Rodrigo, V. 2016. Saturation of barrier materials under thermal gradient. Geomechanics for Energy and the Environment 8: 38-51. https://doi.org/10.1016/j.gete.2016.05.004

[61] Villar, M.V., Iglesias, R.J., Gutiérrez-Álvarez, C., Carbonell, B., Campos, R., Campos, G., Martín, P.L., Castro, B. 2018. FEBEX-DP: Thermo-hydro-mechanical postmortem analysis of bentonite performed at CIEMAT. Technical report CIEMAT/DMA/2G216/2/16. NAB16-024. Madrid, 144 pp.

[62] Villar, M.V., Iglesias, R.J., Gutiérrez-Álvarez, C., Carbonell, B. 2021a. Pellets/block bentonite barriers: laboratory study of their evolution upon hydration. Engineering Geology 292: 106272. https://doi.org/10.1016/j.enggeo.2021.106272

[63] Villar, M.V., Cuevas, J., Melón, A.M. Gutiérrez-Álvarez, C., Ruiz, A.I., Ortega, A., Iglesias, R.J., González, A.E., Brea, N., Fernández, R., Real, E. 2021b. Project MINALBEN. Report on postmortem analyses of samples from cells running for 2.5 years (C3, C4 and C5). Technical Report CIEMAT/DMA/2G219/1/21. Madrid, 86 pp.

[64] Villar, M.V., Iglesias, R.J., Gutiérrez-Álvarez, C. 2022. THM column cell with MX-80 pellets simulating the HE-E in situ experiment for 10 years: online results and final physical state. Informes Técnicos CIEMAT 1507. Madrid, 65 pp.

[65] Whitney, D.L., Evans, B.W. 2010. Abbreviations for names of rock-forming minerals. American Mineralogist 95: 185–187. DOI: 10.2138/am.2010.3371

APPENDIX

Table A- 1 Results of the mercury intrusion porosimetry and BET specific surface area for the HEE-B samples and the original pellets

REFERENCE	DISTANCE TO HEATER (cm)	INTRUDED e (% OF TOTAL)	e PORES >200 nm	MODE PORES >200 (nm)	e PORES <200 nm	MODE PORES <200 (nm)	e_M/e_M	BET a_s (m^2/g)
Pellets	-	47	0.578	251,165	0.255	15	0.44	31
S0	48	73	0.536	18,808	0.52	19	0.97	34
S1	46	73	0.461	13,712	0.494	19	1.07	37
S2	44	70	0.411	15,231	0.521	19	1.27	35
S3	43	66	0.425	15,231	0.576	17	1.36	34
S4	41	70	0.425	13,716	0.524	19	1.23	35
S5	39	70	0.389	10,031	0.515	21	1.32	37
S6	37	69	0.393	12,359	0.534	21	1.36	37
S7	35	70	0.399	13,716	0.519	17	1.30	37
S8	33	69	0.377	10,033	0.53	21	1.40	38
S9	31	69	0.379	8,134	0.526	21	1.39	38
S10	29	68	0.373	13,714	0.529	19	1.42	36
S11	27	65	0.320	9,027	0.554	21	1.73	37
S12	25	70	0.340	43,436	0.503	21	1.48	38
S13	23	64	0.297	99,683	0.556	19	1.87	37
S14	21	63	0.268	59,508	0.564	23	2.10	36
S15	19	70	0.282	122,348	0.513	26	1.82	38
S16	17	71	0.295	2,630	0.509	23	1.72	32
S17	15	75	0.331	462,137	0.427	19	1.29	24
S18	13	44	0.411	466,754	0.272	19	0.66	19
S19	11	64	0.409	465,580	0.287	19	0.70	17
S20	9	43	0.439	464,468	0.257	17	0.58	18
S21	7	37	0.434	465,745	0.262	12	0.60	24
S22	5	31	0.447	461,498	0.249	12	0.56	32
S23	3	33	0.461	536,409	0.236	12	0.51	30
S24	2	77	0.394	205,821	0.239	12	0.61	27
S25	1	41	0.548	461,978	0.246	15	0.45	25

Table A- 2 Analysis of the 1:8 aqueous extracts of samples from cell HEE-B and of the initial pellets (meq/L)

REFERENCE	DISTANCE TO HEATER (cm)	w (%)	pH	ALKALINITY	Ca^{2+}	Mg^{2+}	Na^{+}	K^{+}	Cl^{-}	SO_4^{2-}	HCO_3^{-}	CBE[a] (%)
S0	48	7.3	8.0	3	0.1	0.1	14.1	0.1	8.3	3.5	2.7	-0.2
S1	46	7.0	8.3	3	0.1	0.1	13.3	0.1	6.1	3.9	3.4	0.2
S2	44	5.7	8.2	3	0.3	0.1	17.4	0.1	5.7	10.5	2.8	-2.8
S3	43	5.8	8.2	3	0.3	0.1	17.6	0.1	5.4	11.4	2.5	-3.2
S4	41	7.4	8.0	3	0.3	0.1	17.6	0.1	4.9	11.6	2.8	-2.8
S5	39	9.7	8.1	3	0.3	0.1	17.4	0.1	4.5	12.0	2.9	-4.0
S6	37	9.4	8.0	3	0.3	0.1	16.1	0.1	4.1	11.9	2.6	-5.7
S7	35	8.6	8.1	3	0.3	0.1	15.2	0.1	3.9	11.2	2.8	-6.7
S8	33	9.3	8.0	3	0.2	0.1	15.7	0.1	3.7	9.9	2.8	-1.4
S9	31	9.2	8.1	3	0.1	0.1	13.5	0.1	3.3	7.8	3.0	-1.4
S10	29	8.6	8.2	3	0.2	0.1	14.4	0.1	3.3	9.2	3.3	-3.8
S11	27	9.3	8.1	3	0.3	0.1	17.0	0.2	2.8	13.2	2.7	-3.5
S12	25	10.3	8.2	3	0.2	0.1	15.4	0.1	2.5	11.7	2.7	-3.5
S13	23	10.4	8.4	3	0.1	0.0	14.1	0.1	2.4	9.5	3.3	-2.6
S14	21	11.7	8.3	4	0.1	0.0	12.6	0.1	2.2	7.7	3.6	-2.8
S15	19	15.5	8.2	2	0.4	0.1	19.8	0.2	2.4	17.5	2.1	-3.5
S16	17	10.4	7.7	1	2.3	0.5	31.3	0.4	4.7	33.3	1.2	-6.5
S17	15	15.5	7.9	2	1.1	0.5	26.7	0.4	10.5	18.9	1.9	-4.5
S18	13	12.2	8.0	3	1.1	0.7	25.7	0.5	17.1	11.3	2.5	-5.2
S19[b]	11	8.5	8.0	3	2.2	1.4	32.2	0.7	27.5	11.1	3.0	-6.8
S20[b]	9	5.9	8.1	4	2.7	1.2	38.3	0.6	39.5	10.7	3.5	-11.8
S21[b]	7	2.9	8.3	5	0.7	0.2	24.4	0.3	13.7	10.5	4.4	-7.1
S22[b]	5	1.0	8.3	6	0.5	0.1	17.4	0.2	2.1	11.6	6.0	-4.9
S23[b]	3	0.7	8.4	6	0.5	0.2	21.3	0.3	0.4	14.2	6.2	2.8
S24	2	0.1	8.4	7	0.8	0.2	23.9	0.3	0.4	17.6	6.6	0.9
S25	1	0.0	8.3	7	1.1	0.3	26.1	0.3	0.4	20.4	7.3	-0.5
Avg.	-	7.8	8.1	3	0.6	0.3	19.9	0.2	7.0	12.4	3.4	-3.5
Pellets	-	4.9	8.7	5	0.2	0.0	17.0	0.1	0.4	9.6	5.2	5.9

[a] Charge Balance Error; [b] Nitrate content higher than in reference sample (0.2 meq/L)

Table A- 3 Extractable cations and CEC of samples from cell HEE-B and of the initial pellets (in meq/100 g)

REFERENCE	DISTANCE TO HEATER (cm)	w (%)	Na^+	K^+	Mg^{2+}	Ca^{2+}	Sr^{2+}	SUM EXTRACT.	CEC
S0	48	7.3	49.0	1.4	8.7	16.6	0.3	75.9	77.3
S1	46	7.0	45.0	1.4	8.4	17.0	0.4	72.3	75.5
S2	44	5.7	48.1	1.4	8.5	20.6	0.4	79.1	74.2
S3	43	5.8	48.2	1.4	8.5	21.5	0.4	80.0	76.8
S4	41	7.4	47.1	1.4	8.2	20.0	0.4	77.1	75.4
S5	39	9.7	57.9	1.8	8.3	20.1	0.4	88.5	79.5
S6	37	9.4	57.7	1.9	8.2	20.2	0.4	88.3	78.9
S7	35	8.6	57.2	1.8	7.9	19.5	0.4	86.8	79.8
S8	33	9.3	57.7	1.8	7.8	19.0	0.4	86.6	79.9
S9	31	9.2	57.6	1.8	7.4	17.7	0.3	84.9	79.2
S10	29	8.6	57.2	1.8	7.2	17.5	0.3	84.1	78.2
S11	27	9.3	65.3	1.5	3.6	19.4	0.3	90.2	81.5
S12	25	10.3	69.8	1.5	3.3	18.0	0.3	93.0	79.0
S13	23	10.4	68.0	1.6	3.2	15.9	0.3	88.9	76.4
S14	21	11.7	55.1	2.1	2.8	15.4	0.1	75.4	76.2
S15	19	15.5	53.9	2.2	2.6	20.9	0.1	79.6	75.8
S16	17	10.4	57.9	2.1	3.2	31.2	0.2	94.6	75.9
S17	15	15.5	52.7	2.4	9.3	24.4	0.4	89.1	73.9
S18	13	12.2	47.9	2.8	12.7	23.6	0.3	87.3	74.3
S19	11	8.5	48.8	2.9	13.7	26.7	0.3	92.5	72.2
S20	9	5.9	48.2	2.2	6.5	28.1	0.3	85.3	69.8
S21	7	2.9	43.5	2.0	3.9	24.1	0.3	73.8	70.2
S22	5	1.0	36.6	2.0	3.4	21.2	0.3	63.4	71.5
S23	3	0.7	49.1	2.0	3.7	25.8	0.4	80.9	71.7
S24	2	0.1	48.8	2.0	4.0	28.0	0.0	82.6	72.3
S25	1	0.0	48.7	2.0	3.8	29.8	0.4	84.7	69.0
Average	-	-	53.0	1.9	6.5	21.6	0.3	83.3	75.6
Pellets	-	4.9	62.4	1.6	2.2	16.6	0.2	82.9	77.6


2695-8864